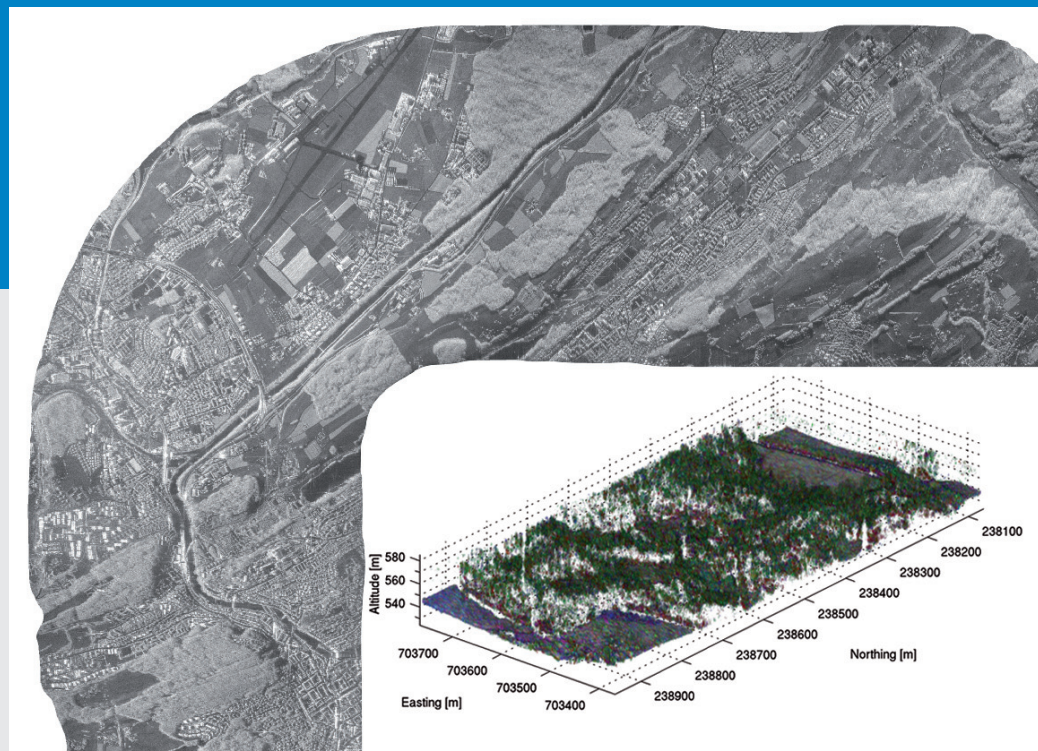


OTHMAR FREY

Synthetic Aperture Radar Imaging in the Time Domain for Nonlinear Sensor Trajectories and SAR Tomography



Editorial Board of the Remote Sensing Series:

Prof. Dr. Michael E. Schaepman, Dr. Erich Meier, Dr. Mathias Kneubühler, Dr. David Small,
Dr. Felix Morsdorf

Author:

Othmar Frey

Remote Sensing Laboratories, Department of Geography, University of Zurich
Winterthurerstrasse 190, CH-8057 Zurich, Switzerland

<http://www.geo.uzh.ch/rs1>

Frey, Othmar

Synthetic Aperture Radar Imaging in the Time Domain for Nonlinear Sensor Trajectories and
SAR Tomography

Remote Sensing Series, Vol. 59 – Zurich: Remote Sensing Laboratories, 2010.

ISBN: 978-3-03703-025-7

© Copyright 2010 – Othmar Frey, University of Zurich, Switzerland. All rights reserved.

Typesetting with L^AT_EX 2_ε.

Printed by *Reprozentrale ETH Zürich*.

Front page: L-shaped SAR image calculated by time-domain back-projection using airborne SAR data of a curvilinear acquisition, and, a three-dimensional image reconstruction of a forested area by means of tomographic processing of an airborne repeat-pass multibaseline SAR data set. Sensor: E-SAR L-band.

This work was approved as a PhD thesis (with distinction) by the Faculty of Science of the University of Zurich in the fall semester 2010 on the basis of expert reviews by Prof. Dr. Michael E. Schaepman (Remote Sensing Laboratories, University of Zurich), Dr. Erich Meier (Remote Sensing Laboratories, University of Zurich), Priv.-Doz. Dr. habil. Andreas Reigber (German Aerospace Center DLR/TU Berlin), Prof. Dr. Alberto Moreira (German Aerospace Center DLR/Karlsruhe Institute of Technology), Prof. Dr. Lars M. H. Ulander (FOI/Chalmers University of Technology).

Die vorliegende Arbeit wurde von der Mathematisch-naturwissenschaftlichen Fakultät der Universität Zürich im Herbstsemester 2010 aufgrund der Gutachten von Prof. Dr. Michael E. Schaepman (Remote Sensing Laboratories, Universität Zürich), Dr. Erich Meier (Remote Sensing Laboratories, Universität Zürich), Priv.-Doz. Dr. habil. Andreas Reigber (Deutsches Zentrum für Luft- und Raumfahrt DLR/TU Berlin), Prof. Dr. Alberto Moreira (Deutsches Zentrum für Luft- und Raumfahrt DLR/Karlsruher Institut für Technologie), Prof. Dr. Lars M. H. Ulander (FOI/Chalmers University of Technology) als Dissertation (mit Auszeichnung) angenommen.

Doctorate Committee/Promotionskomitee:

Prof. Dr. Michael E. Schaepman (Chair/Vorsitz), Dr. Erich Meier (Supervision/Leitung der Dissertation), Priv.-Doz. Dr. habil. Andreas Reigber.

Summary

Synthetic aperture radar (SAR) systems are used to obtain geospatial information for a broad range of applications, such as measuring geo- and biophysical parameters, topographic mapping, monitoring of land subsidence, landslides, and crustal deformation, as well as disaster mapping. In recent years, advanced SAR acquisition modes of growing complexity have been proposed in order to gain more flexibility in terms of usable sensor constellations and acquisition scenarios, as well as in an attempt to increase the number of observables to allow for a more reliable image and parameter inversion. These new imaging modes require more flexible SAR image reconstruction algorithms.

Within the scope of this dissertation, a novel time-domain back-projection (TDBP) based SAR image processing software was developed and investigated in terms of two nonstandard data acquisitions scenarios: 1) SAR imaging along highly nonlinear sensor trajectories, and 2) high-resolution tomographic imaging of a forest at L-band and P-band. To this end, two airborne SAR experiments were designed, which were flown by the German Aerospace Center's E-SAR system in September 2006.

By means of the experimental data involving highly nonlinear sensor trajectories it was shown that the TDBP focusing algorithm yields a superior image quality as compared to a combined chirp scaling and mosaicking approach. The results of the study indicate that, in general, the TDBP algorithm imposes virtually no restrictions on the shape of the sensor trajectory. It is therefore an attractive method for efficient mapping along curvilinear objects of interest, such as traffic routes, rivers, or pipelines.

A second emphasis of this dissertation is on SAR tomography of forest environments. In order to explore in detail the back-scattering behavior of radar signals within a forest a non-model-based TDBP tomographic imaging approach was pursued. In particular, three different direction-of-arrival estimation techniques, multilook beamforming, robust Capon beamforming, and MUSIC beamforming, were implemented in order to focus the two multibaseline airborne SAR data sets at L-band and P-band. In terms of focusing quality, an unprecedented level

of detail was obtained using the proposed TDBP-based tomographic imaging approach. Gaps in the canopy due to features like small forest roads are well visible in the tomographic image, for instance. Thus, the three-dimensional tomographic SAR imagery provides a good basis to investigate the back-scattering properties of the forested area at L-band and P-band.

With three prospective spaceborne SAR remote sensing missions, BIOMASS at P-band, Tandem-L, and DESDynI, both at L-band, which are all aimed at global mapping and monitoring of carbon stock by assessing the above ground biomass of forests, establishing a good understanding of the interaction of microwaves at L-band and P-band with forests is critical in order to develop reliable biomass products. By means of a detailed analysis of the high-quality three-dimensional SAR data products obtained by tomographic processing, including a cross-validation with airborne laser scanning data, a substantial contribution towards an improved understanding of the interaction of microwaves at L-band and P-band with forest environments was achieved within this work.

Zusammenfassung

Radarsysteme mit synthetischer Apertur (SAR) werden zur Gewinnung von raumbezogener Information für eine breite Palette von Anwendungen benutzt, wie beispielsweise zur Messung von geo- und biophysikalischen Parametern, zur Ableitung von Höheninformation, zur Überwachung von Absenkungen, Hangrutschungen und Bewegungen der Erdkruste, sowie zur Schadenserfassung nach Naturkatastrophen. Im Hinblick auf eine Verbesserung der Flexibilität bezüglich verwendbarer Sensorkonstellationen und möglicher Datenakquisitionsszenarien, sowie mit dem Ziel, die Anzahl der Beobachtungen zu erhöhen, um eine zuverlässigere Bildgebung und Parameterinversion zu erreichen, haben in den letzten Jahren neue, komplexe SAR Datenakquisitionsmodi grosse Beachtung gefunden. Diese neuen SAR Modi verlangen flexiblere SAR Bildrekonstruktionsalgorithmen.

Im Rahmen dieser Dissertation wurde eine neue SAR Prozessierungssoftware, welche auf dem “time-domain back-projection” (TDBP) Prinzip basiert, entwickelt und anhand von zwei nicht standardmässigen Aufnahmemodi getestet und evaluiert: 1) SAR Aufnahmen entlang von hochgradig nichtlinearen Sensortrajektorien, und 2) hochauflösende tomographische Aufnahmen eines Waldes im L- und P-Band. Die entsprechenden Daten wurden mittels zweier Experimente erhoben, welche im September 2006 mit dem flugzeuggestützten E-SAR Sensor des Deutschen Zentrums für Luft- und Raumfahrt durchgeführt wurden.

Mithilfe der experimentellen Daten, welche von hochgradig nichtlinearen Sensortrajektorien aufgenommen wurden, konnte gezeigt werden, dass der TDBP Algorithmus, im Gegensatz zu einem kombinierten “Chirp Scaling”- und Mosaikierungsansatz, trotz nichtlinearer Fluggeometrie keine Verschlechterung der Bildqualität aufweist. Die Ergebnisse der Studie zeigen, dass der vorgestellte TDBP Algorithmus grundsätzlich kaum Einschränkungen bezüglich der Aufnahmegeometrie unterliegt. Die Prozessierungsmethode ermöglicht somit eine effiziente Datenerfassung entlang kurvenförmiger Gebiete und Objekte, wie zum Beispiel Verkehrswege, Flüsse oder Pipelines.

Der zweite Schwerpunkt dieser Dissertation liegt auf der tomographischen Ab-

bildung von Waldgebieten mittels “Multibaseline” SAR Daten. Um das Rückstreuverhalten von Radarsignalen innerhalb eines Waldes zu untersuchen wurde ein nicht-modellbasierter, auf dem TDBP Verfahren beruhender Ansatz verfolgt. Insbesondere wurden drei verschiedene “Direction-of-Arrival” Schätzverfahren, Multilook Beamforming, Robust Capon Beamforming und MUSIC implementiert, um die beiden “Multibaseline” SAR Datensätze im L- und P-Band zu fokussieren. Hinsichtlich der Fokussierungsqualität konnte mit dem vorgestellten TDBP-basierten Ansatz ein bisher unerreichter Detaillierungsgrad in der tomographischen Fokussierung erzielt werden. So sind beispielsweise Lücken im Kronenschluss des Waldes über Forstwegen im fokussierten tomographischen Bild immer noch gut erkennbar. Damit bieten die dreidimensionalen tomographischen SAR Bilder eine geeignete Grundlage, um die Rückstreueigenschaften des aufgenommenen Waldes in den Frequenzen L-Band und P-Band zu untersuchen.

Im Hinblick auf drei in Aussicht stehende satellitengestützte SAR Fernerkundungsmissionen, BIOMASS im P-Band, Tandem-L und DESDynI, im L-Band, welche unter anderem auf eine globale Kartierung und Überwachung des in Form von Waldbiomasse gespeicherten Kohlenstoffbestandes ausgerichtet sind, ist ein vertieftes Verständnis der Wechselwirkung von Mikrowellen im L-Band und P-Band mit Wald unerlässlich, um zuverlässige Produkte zu entwickeln. Im Rahmen dieser Arbeit konnte aufgrund einer detaillierten Analyse der erzeugten, dreidimensionalen SAR Datenprodukte, einschliesslich einer Validierung mit hochauflösenden Laserscanning-Daten, ein wesentlicher Beitrag zu einem besseren Verständnis der Rückstreueigenschaften von Wald mit Mikrowellen im L- und P-Band geleistet werden.

Contents

1	Introduction	1
1.1	General Background	1
1.2	Aperture Synthesis in a Nutshell	3
1.2.1	Diffraction	3
1.2.2	The Fundamental Resolution Limit of Imaging Systems	8
1.2.3	Synthesizing a Larger Aperture	9
1.3	Imaging Paradigms in Synthetic Aperture Radar Data Processing	12
1.3.1	Basic Focusing Steps	13
1.3.2	Range-Doppler Paradigm	15
1.3.3	Wavenumber Domain Paradigm	16
1.3.4	Tomographic Imaging Paradigm	17
1.3.5	Time-Domain Back-Projection	18
1.4	Rationale of Dissertation	21
1.4.1	Motivation	21
1.4.2	Objectives	24
1.4.3	Structure of the Thesis	27
	References	27
2	Focusing of Airborne Synthetic Aperture Radar Data From Highly Nonlinear Flight Tracks	35
	Abstract	35
2.1	Introduction	36
2.1.1	Nonlinear Flight Tracks: Previous Work	36
2.1.2	TDBP Processing	37
2.1.3	Aim of This Paper	39
2.2	Processing of Nonlinear Flight Tracks	39
2.2.1	Patchwise Frequency-Domain Processing and Mosaicking	39
2.2.2	TDBP	42
2.3	Description of the Experiment	47
2.3.1	Experimental Setup	47
2.3.2	Quality Measures for Focused Data	50

2.4	Results	50
2.4.1	Image Comparison	51
2.4.2	Analysis of the Impulse Response	54
2.4.3	Coherence Maps	58
2.4.4	Complete 90° Curve Flight	59
2.5	Discussion	61
2.6	Conclusion	62
	Acknowledgment	63
	References	63
3	Tomographic Imaging of a Forested Area By Airborne Multi-Baseline P-Band SAR	67
	Abstract	67
3.1	Introduction	67
3.2	The SPECAN Algorithm, Resolution and Sampling in the Normal Direction	69
3.3	3D Focusing in the Time-Domain	72
3.4	Experimental Set-Up	74
3.5	Simulated Data	77
3.6	Experimental Results	78
3.7	Discussion and Conclusion	79
	Acknowledgment	81
	References	82
4	3D SAR Imaging of a Forest Using Airborne Multibaseline Data at L- and P-Band	85
	Abstract	85
4.1	Introduction	85
4.1.1	Previous Work/State of the Art	86
4.1.2	Aim of This Paper	88
4.2	Data Model and Focusing Methods	89
4.2.1	Multilook Standard Beamforming (MLBF) and the One-Look Special Case	91
4.2.2	Multiple Signal Classification (MUSIC)	93
4.2.3	Robust Capon Beamforming (RCB)	96
4.2.4	A Few Comments on the Processing Approach	100
4.2.5	A Note On Baseline Calibration	100
4.3	Description of the Experiment	102

4.3.1	Experimental Set-Up for SAR Tomography	102
4.3.2	Cross-Validation Data	103
4.4	Results	103
4.4.1	Analysis of the Impulse Response	103
4.4.2	Tomographic Images	106
4.5	Discussion	106
4.5.1	Analysis of the Impulse Response	106
4.5.2	Tomographic Images	109
4.6	Conclusion	110
	References	111
5	Analyzing Tomographic SAR Data of a Forest With Respect to Frequency, Polarization, and Focusing Technique	113
	Abstract	113
5.1	Introduction	114
5.1.1	Aim of This Paper	115
5.2	Data and Methods	117
5.2.1	Focused Tomographic Data	117
5.2.2	Validation Data	119
5.2.3	Methods Used for Data Analysis	119
5.3	Experimental Results	123
5.3.1	Vertical Profiles	123
5.3.2	Entropy/ α Scatter Plots	123
5.3.3	Ground Level Detection	127
5.4	Discussion	127
5.4.1	Vertical Profiles	127
5.4.2	Entropy/ α Scatter Plots	130
5.4.3	Ground Level Detection	131
5.5	Conclusion	132
	References	133
6	Synopsis	139
6.1	Main Findings	139
6.1.1	Nonlinear Flight Tracks	139
6.1.2	SAR Tomography	140
6.2	Conclusion	143
6.3	Outlook	145

Acknowledgment	147
Scientific Communications	149

List of Figures

1.1	Fraunhofer diffraction patterns for a single slit, a rectangular aperture, and a circular aperture.	7
1.2	SAR data representations during focusing: raw data, range-compressed data, and azimuth-focused data.	14
1.3	Flow diagram of the time-domain back-projection based synthetic aperture radar processor.	20
2.1	Schematic illustration of mosaicking through geocoding of the individually focused subpatches of the data set.	41
2.2	Schematic view of the acquisition/reconstruction geometry for TDBP processing of SAR data from nonlinear flight tracks. . . .	45
2.3	Nonlinear flight tracks flown during the experiment: 1) Quasi-linear reference track, 2) double bend, 3) dive, and 4) 90° curve. . . .	48
2.4	Variation of the midelevation Doppler centroid values along the flight track for the four different flight paths, calculated from navigation data.	49
2.5	Close-up views of amplitude images. (a) ECS&M: (Quasi-)linear reference track. (b) TDBP: (Quasi-)linear reference track. (c) ECS&M: Double bend. (d) TDBP: Double bend.	52
2.6	Close-up views of amplitude images. (a) ECS&M: Dive. (b) TDBP: Dive. (c) ECS&M: 90° curve. (d) TDBP: 90° curve. . . .	53
2.7	Impulse response and quality figures of a simulated point target for all four flight tracks.	55
2.8	Impulse response and quality figures of a trihedral corner reflector for all four flight tracks.	56
2.9	Two-dimensional power spectra for all four test data sets corresponding to the surrounding area of the in-scene corner reflector.	58
2.10	Coherence maps for the pairs (a) dive/reference track and (b) double bend/90° curve processed by TDBP.	59
2.11	Amplitude image of the 90° curve track: E-SAR L-band HH. Processing: TDBP.	60

3.1	Simplified tomographic imaging geometry.	70
3.2	P-band tomographic acquisition pattern consisting of 11 flight tracks.	75
3.3	Impulse responses resulting from TDBP tomographic imaging of the multi-baseline P-band raw data set.	78
3.4	(a) RGB ortho-image of a partially forested area. (b) SAR intensity values within a horizontal tomographic slice. (c) Coherence map of the zero baseline configuration.	80
3.5	Vertical slices of the SAR tomographic image in south-northern direction.	81
3.6	Vertical slices of the SAR tomographic image in west-eastern direction.	82
4.1	Tomographic acquisition scenario and the three-dimensional reconstruction grid.	90
4.2	Tomographic acquisition patterns: (a) P-band, 11 tracks and (b) L-band, 16 tracks.	101
4.3	Impulse responses obtained from a trihedral reflector using three different approaches to focus the MB data in the normal direction: MLBF, RCB, and MUSIC beamforming.	104
4.4	Tomographic image (3D voxel plot) of a partially forested area obtained from combined TDBP and MUSIC beamforming of polarimetric airborne MB SAR data at L-band.	105
4.5	Vertical slices through a 3D volume of a forested area obtained from a polarimetric multibaseline L-Band data set.	107
4.6	Vertical slices through a 3D volume of a forested area obtained from a polarimetric multibaseline P-Band data set.	108
5.1	Tomographic acquisition patterns at P- and L-band.	118
5.2	Entropy/alpha classification scheme after Cloude and Pottier.	122
5.3	Vertical profiles of relative intensities from L-band tomographic data of a partially forested area.	124
5.4	Vertical profiles of relative intensities from P-band tomographic data of a partially forested area.	125
5.5	Histograms of height difference between ALS DSM and DEM.	126
5.6	Entropy/ α scatter plot for different horizontal layers.	126
5.7	Ground level detection below canopy at L-band.	128
5.8	Ground level detection below canopy at P-band.	129

List of Tables

2.1	E-SAR L-band system specifications.	48
3.1	E-SAR P-band system parameters.	76
3.2	Nominal parameters used in the set-up of the P-band tomographic SAR experiment.	76
4.1	E-SAR system specifications and nominal parameters of the tomographic acquisition patterns for both multibaseline data sets at P-band and L-band.	102
5.1	E-SAR system specifications and nominal parameters of the tomographic acquisition patterns for both multibaseline data sets at P-band and L-band.	116

Preface

The topic of this paper-based dissertation is synthetic aperture radar (SAR) imaging in the time-domain with a special emphasis on two nonstandard data acquisition modes, nonlinear sensor trajectories and multibaseline SAR tomography, respectively. At the core of the thesis at hand stand four scientific publications each of which is self-contained in terms of both, structure and content. The purpose of the introduction that precedes the publications is threefold: 1) The first two Sections 1.1 & 1.2 give a more general introduction to the subject of synthetic aperture radar remote sensing aimed at a potential reader with a technical or scientific background, yet unfamiliar with the topic. 2) Section 1.3 introduces the main classes of SAR image reconstruction paradigms and forms the basis where the motivation for SAR imaging in the time domain is deduced from. 3) Section 1.4 contains the rationale of the dissertation. The main findings drawn from the publications are compiled in a synopsis in Section 6.

1 Introduction

1.1 General Background

The increasing complexity of human activity and its impact on the planet Earth demand a comprehensive understanding of how the various dynamic processes, natural and man-made, interact and, in particular, how they affect the natural and socio-economic environment we are living in. A fundamental prerequisite in order to gain information about the spatial and temporal variation of phenomena of interest is an adequate means to measure the current state of our environment at different scales ranging from local to regional to global. As a consequence, over the last decades, remote sensing technology and the resulting products have become a major source of spatial information for monitoring and planning tasks assumed by local authorities, governmental agencies, supranational and intergovernmental organizations, as well as private industry.

Envisioning the experience of standing on a high building, a tower, a mountain top, or sitting next to the window on an airplane and looking down at the earth, it is obvious to everyone that observing the earth *from a distance* reveals a wealth of information at a single glance; information, that is not readily available when standing on the ground in flat terrain. Thus, capturing this information in a systematic way by means of adequate sensors on board of air- and spacecraft is a consequential next step to just “looking at the earth” with our own remote sensing device, the human eye.

Remote sensing, according to a common definition [1], encompasses the entirety of all methods which goal consists of retrieving information about the earth’s surface by means of measuring and interpreting (energetic) fields that emanate from the earth. Thereby, electromagnetic radiation that is back-scattered or emitted by the earth serves as a carrier of information. These definitions are analogously valid for remote sensing of other celestial bodies. Remote sensing provides a means to not only overcome by far the very limited resolving capability of a human eye in terms of both, the spatial and the spectral resolution. It also allows for capturing information that is carried by the non-visible parts

of the electromagnetic spectrum.

Regarding the source of electromagnetic radiation two classes of remote sensing systems are identified: passive remote sensing, where electromagnetic radiation of a natural source (e.g. the sun, thermal radiation etc.), back-scattered or emitted by an object of interest, is detected; and active remote sensing, where an artificial source of radiation is part of the remote sensing system. Active remote sensing systems are further distinguished into light detection and ranging (lidar) systems, and radio detection and ranging (radar) systems. Lidar systems use a laser device as their source of radiation, thus, work in the optical domain. With radar systems microwave antennas are employed for transmitting electromagnetic waves and receiving their back-scattered echoes.¹ As the term “ranging” suggests these two types of active systems measure the time-delay between transmitting a signal and receiving the portion of the signal that is back-scattered towards the sensor. The propagation time is related to the distance (range). By combining this information with the sensor’s position and attitude the geolocation of the object where the scattering process occurred can be determined. In this basic mode, the cross-range resolution of the system is governed by the beam footprint, which is a function of the wavelength, the aperture of the sensor, and the range distance. In the context of radar remote sensing, the resolution obtained in this way is typically low as a consequence of the large wavelengths of microwaves (m to mm), as compared to the wavelengths in the optical domain (μm to nm), for instance. In the next section, a concept, termed aperture synthesis, that alleviates this adverse property is discussed in some detail. The high resolution imaging radar technique based on this concept is called *synthetic aperture radar* (SAR).

When thinking of remote sensing as an operational monitoring tool imaging radar technology brings in a number of attractive assets: The source of radiation, the radar antenna, is man-made and, therefore, well-controlled. It can be deployed in the required manner, limited only by the degree of freedom and mission constraints of the carrying air- or spacecraft. As a further con-

¹Electromagnetic waves within the frequency interval from 300MHz to 300GHz are commonly termed *microwaves*. In fact, multiple differing definitions of the exact boundaries of this interval and its subdivision into a number of frequency bands are found in literature. Skolnik [2] is a comprehensive resource on this topic. Within this dissertation, two bands are of importance, UHF (or P-band) (300MHz-1GHz) and L-band (1GHz-2GHz). Note, that throughout this thesis the terminology P-band is used instead of UHF-band. P-band is a sub-band nomenclature considered obsolete according to IEEE standard 521-1984 but it is widely used within the SAR community as well as by a number of data providers. The operating frequencies of the E-SAR system are at 350MHz for the P-band sensor, and at 1.3GHz for the L-band sensor. Each sensor features a nominal bandwidth of 94MHz.

sequence of the artificial source of radiation the data-acquisition schedule is not restricted by external factors such as day-light or weather conditions. Microwaves experience very little attenuation when they propagate through the earth's atmosphere², they penetrate clouds, and within a substantial range of the microwave frequency band (at wavelengths of the order of decimeters and larger), radar imaging is possible even in case of heaviest precipitation. Further, synthetic aperture radar, unlike optical remote sensing, is the only imaging remote sensing technique where the spatial resolution of the resulting imagery is not a function of the distance between the sensor and the object of interest.

Achieving a high resolution by means of adequate synthetic aperture radar signal processing is the main topic of this dissertation. More specifically, the research presented within this thesis treats aperture synthesis of airborne radar data in case of nonstandard acquisition modes, such as highly nonlinear sensor trajectories, on the one hand, and three-dimensional SAR imaging, referred to as SAR tomography, on the other hand.

1.2 Aperture Synthesis in a Nutshell

In this section, a short overview of the general concept of aperture synthesis is given. In particular, aperture synthesis within the context of radar remote sensing is highlighted. These explanations are accompanied by a brief sketch of further relevant basic concepts of radar imaging. For an in-depth treatment of the subject the interested reader is referred to the following excellent and comprehensive textbooks on synthetic aperture radar signal processing [8–11] and Fourier array imaging [12]. Unless indicated otherwise, the subsequent paragraphs are based on material compiled from references [12–14].

1.2.1 Diffraction

For many applications it is critical that remote sensing data is available at a high level of detail. Striving for a high spatial resolution has therefore always been one of the key challenges in remote sensing. As for any imaging system, there is a fundamental physical limit that determines the maximum resolving

²While only being attenuated mildly microwaves are subject to polarization rotation (Faraday rotation) and propagation delays, which depend on the total electron content of the ionosphere, as well as to propagation delays in the troposphere, which change as a function of the hydrodynamic condition (see [3–7]).

performance that can theoretically be achieved by a remote sensing system. This limit is imposed by the physical phenomenon of *diffraction*. Waves of any kind (electromagnetic waves, sound waves, ocean waves etc.) are subject to diffraction when they interact with an object. In the context of the fundamental resolution limit of imaging systems, the diffraction pattern that occurs when a wave front impinges on a slit, a rectangular, or a circular aperture, is of interest. The real-world equivalents would be the antenna array (real aperture) in the case of radar, or the slit dimension in optics, respectively.

For remote sensing systems, where the physical aperture D is typically very small compared to the distance R from the object under examination, a type of diffraction, called *Fraunhofer, far-field, or plane-wave diffraction*, defines the fundamental theoretical resolution.

According to the Huygens-Fresnel principle [13], every point on a wavefront is a source of a secondary wavelet. Assuming a one- or two-dimensional aperture, which lies in the tangent plane of the spherical wave, and assuming the far-field case, a planar wavefront “impinges” on the aperture at one instance of time. Thus, an infinite number of secondary radiating point sources, which oscillate in phase occupy the planar wavefront within the planar aperture \mathbf{S} at locations $\vec{r}_e(l), l \in \mathbf{S}$. The radiation stemming from a secondary radiating point source within the aperture \mathbf{S} experienced at a point in space with position vector \vec{r} is then

$$E_{sec} = \frac{1}{R} a(l) e^{i\omega t - ik|\vec{r} - \vec{r}_e(l)|} dl, \quad (1.1)$$

where $R = |\vec{r} - \vec{r}_c|$. \vec{r}_c is the center of the aperture, $a(l)$ is an amplitude function, i is the imaginary unit, ω is the angular frequency, t is the time, $k = 2\pi/\lambda$ is the wavenumber and λ , again, is the wavelength, and dl represents an infinitesimally sized patch of the planar aperture \mathbf{S} . Hence the total radiation experienced at the spatial point defined by \vec{r} is obtained by integrating over all secondary radiating point sources within the aperture \mathbf{S} :

$$E(x, y) = \frac{1}{R} \int_{l \in \mathbf{S}} a(l) e^{i\omega t - ik|\vec{r} - \vec{r}_e(l)|} dl \quad (1.2)$$

which is called the Fresnel-Kirchhoff diffraction integral. The conception of both, plane waves that are subject to diffraction when passing an aperture (optical case), and planar wavefronts that impinge on, or are transmitted by a planar antenna, are equivalent and therefore yield similar diffraction patterns.

In terms of the fundamental resolution of remote sensing systems, we are interested in the diffraction patterns that occur in the far-field case.³ Essentially, the far-field case is obtained by approximating the nonlinear dependence of (1.2) on $R = |\vec{r} - \vec{r}_e(l)| = \sqrt{(x - x_e(l))^2 + (y - y_e(l))^2 + (z - z_e(l))^2}$ using a Taylor series expansion. Let us choose the coordinate system in such a way that $z_e(l) = 0$, i.e., the z-axis runs orthogonal to the aperture plane. Then, the Taylor series expansion of R yields

$$\begin{aligned} R &= \sqrt{z^2 + (x - x_e(l))^2 + (y - y_e(l))^2} \\ &= z \left(1 + \frac{(x - x_e(l))^2}{2z^2} + \frac{(y - y_e(l))^2}{2z^2} + \dots \right). \end{aligned} \quad (1.3)$$

Stopping the expansion after the quadratic terms we obtain the Fresnel, or near-field, diffraction (E is the electric field strength)

$$E(x, y, z) = \frac{e^{-ikz}}{i\lambda z} \int_{l \in \mathbf{S}} E(x_e(l), y_e(l)) \cdot e^{\frac{-ik}{2z}((x-x_e(l))^2 + (y-y_e(l))^2)} dl. \quad (1.4)$$

The Fraunhofer, or far-field, diffraction is obtained by expanding the quadratic terms of the second order Taylor series expansion of R :

$$\begin{aligned} R &\approx z \left(1 + \frac{x^2 - 2xx_e(l) + x_e^2(l) + y^2 - 2yy_e(l) + y_e^2(l)}{2z^2} \right) \\ &= z \left(1 + \frac{x^2 + y^2}{2z^2} - \frac{xx_e(l)}{z^2} - \frac{yy_e(l)}{z^2} + \frac{x_e^2(l) + y_e^2(l)}{2z^2} \right). \end{aligned} \quad (1.5)$$

If the size of the aperture \mathbf{S} is small compared to z , then

$$z \gg \frac{1}{\lambda}(x_e^2(l) + y_e^2(l)) \quad (1.6)$$

holds, and thus,

$$e^{(x_e^2(l) + y_e^2(l))/(\lambda z)} \approx 1. \quad (1.7)$$

As a consequence, in (1.5), the quadratic terms in x_e and y_e are negligibly small and the quadratic terms in x and y can be placed outside the integral in (1.4).

³A more general (neither using the Fresnel nor the Fraunhofer approximation) treatment of the radiation pattern for dish-type radar antennas can be found in [10].

Thus, a further simplification of the Fresnel approximation (1.4), the Fraunhofer approximation, is obtained:

$$E(x, y, z) = A(x, y, z) \int_{l \in \mathbf{S}} E(x_e(l), y_e(l)) e^{\frac{-ik}{z}(xx_e(l) + yy_e(l))} dl . \quad (1.8)$$

where $A(x, y, z) = \frac{e^{-ikz}}{i\lambda z} \cdot e^{(-i\pi) \cdot (x^2 + y^2) / (\lambda z)}$.

Evaluating (1.8) for a single vertical slit of horizontal width D_x and an infinite vertical extension $D_y = \infty$, and further using $k = 2\pi/\lambda$, yields

$$E(x, y, z = z_0) = E_0 \frac{\sin\left(\frac{\pi D_x x}{\lambda z_0}\right)}{\frac{\pi D_x x}{\lambda z_0}} . \quad (1.9)$$

For a rectangular aperture of dimensions D_x , D_y , the Fraunhofer diffraction pattern is

$$E(x, y, z = z_0) = E_0 \frac{\sin\left(\frac{\pi D_x x}{\lambda z_0}\right)}{\frac{\pi D_x x}{\lambda z_0}} \frac{\sin\left(\frac{\pi D_y y}{\lambda z_0}\right)}{\frac{\pi D_y y}{\lambda z_0}} . \quad (1.10)$$

Similarly, for a circular aperture of diameter D the Fraunhofer diffraction pattern

$$E(r, z = z_0) = E_0 \frac{2J_1\left(\frac{\pi D r}{\lambda z_0}\right)}{\frac{\pi D r}{\lambda z_0}} \quad (1.11)$$

is obtained, where $r = \sqrt{x^2 + y^2}$, and J_1 is the Bessel function of the first kind of order one.

An interesting and, in practice, a very useful property of Fraunhofer diffraction is the fact that the amplitude distribution of the Fraunhofer diffraction pattern is directly proportional to the Fourier transform of the aperture shape.

This becomes obvious when (1.8) is rewritten for the rectangular aperture case, for instance,

$$E(x, y, z = z_0) = E_0 \int_{-D_y/2}^{D_y/2} \int_{-D_x/2}^{D_x/2} e^{\frac{-ik}{z_0}(xx_e + yy_e)} dx_e dy_e , \quad (1.12)$$

which is easily identified as the two-dimensional Fourier transform of the rectangular function $rect(x_e, y_e)$

$$rect(x_e, y_e) = \begin{cases} 1, & |x_e| \leq D_x/2 \quad |y_e| \leq D_y/2 \\ 0, & |x_e| > D_x/2 \quad |y_e| > D_y/2 \end{cases}$$

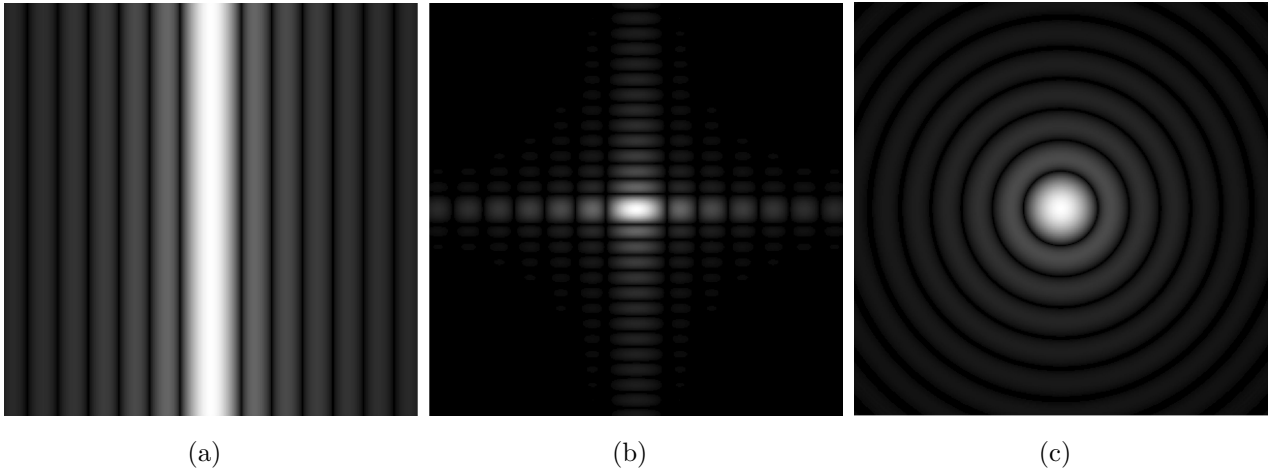


Figure 1.1: Fraunhofer (far-field) diffraction patterns obtained from the following planar apertures: a) a single vertical slit of horizontal width $D_x = D$ and infinite vertical extension $D_y = \infty$ b) a rectangular aperture of dimensions $D_x = D, D_y = 2D$, c) a circular aperture of diameter D . The grayscale map has been adjusted to increase the visibility of the diffraction pattern.

In Fig. 1.1, the intensity distributions of the Fraunhofer diffraction patterns are shown for three different shapes of apertures: a single slit, a rectangular, and a circular aperture, respectively. The following is notable: A constant field amplitude within a rectangular aperture of the dimensions D_x, D_y yields the same diffraction pattern as two orthogonally running slits of infinite length and widths D_x, D_y , respectively. The horizontal apertures of both, the single slit and the rectangular aperture, which lead to the far-field diffraction patterns shown in Figs. 1.1(a) & 1.1(b), are of the same size $D_x = D$. Thus the central, or, main lobe of the diffraction pattern has the same width in the horizontal dimension in both cases. The vertical extension $D_y = 2D$ of the rectangular aperture, however, is *twice* the size of the horizontal aperture, which leads to a main lobe that is only *half* as wide as compared to the horizontal dimension. The far-field diffraction pattern depicted in Fig. 1.1(c) results from a circular aperture of diameter $D_r = D$.

In conclusion, for rectangularly shaped apertures the intensity distribution of the far-field diffraction pattern is sinc-squared-shaped ($\text{sinc}^2(\xi) = \sin^2(\xi)/\xi^2$) in either dimension, and a circular aperture leads to a pattern in the form of the so-called airy function ($(2J_1(\rho))^2/\rho^2$). In the following, the Fraunhofer diffraction pattern is also called the point spread function (PSF) or the impulse response function (IRF) of an imaging system.

1.2.2 The Fundamental Resolution Limit of Imaging Systems

In the context of imaging systems, the resolution is a measure for the separability of two point targets (dirac pulses). The width of the main lobe of the Fraunhofer diffraction pattern defines the fundamental resolving performance of an imaging system. Looking at the diffraction patterns given in Fig. 1.1 it can be observed that the first dark line or circle defines the width of the main lobe. In terms of mathematical expressions the dark lines correspond to the roots of the sinc and airy function, respectively. The roots of the sinc function are found at

$$\xi_0 = \pm n\pi, \text{ for } n = 1, \dots, \infty . \quad (1.13)$$

The outer boundary of the main lobe can be expressed in terms of the aperture D_x and the wavelength λ by combining (1.9) and (1.13)

$$\frac{\pi D_x x}{\lambda z_0} = \pi , \quad (1.14)$$

further, using $x/z_0 = \sin(\delta_\vartheta)$, where δ_ϑ is called the divergence angle, (1.14) can be rewritten as

$$\sin(\delta_\vartheta) = \frac{\lambda}{D_x} . \quad (1.15)$$

In optics, a common empirical definition of resolution is the so-called Rayleigh criterion. According to the Rayleigh criterion, two point sources are considered to be just resolved if the center of the main lobe of the IRF of the first point source coincides with the first root of the IRF of the second point source—a circular aperture is assumed. The first root of the airy function is found at $\rho_0^1 = 1.220\pi$ (see [13]). In analogy to (1.15) this yields

$$\sin(\delta_\vartheta) = 1.22 \frac{\lambda}{D_r} , \quad (1.16)$$

where δ_ϑ is the angular resolution that could theoretically be obtained, if no other resolution-degrading effects were present.

In radar remote sensing (and also for other modern imaging systems) a slightly different definition of resolution is used since the sensitivity of these devices is usually better than imposed by the Rayleigh criterion. Commonly, and also throughout this work, the -3dB width of the main lobe of the intensity distribution of the Fraunhofer diffraction pattern is used as a definition of the angular

resolution, which is obtained by solving

$$10 \log_{10} \left(\frac{I(\pi D / \lambda \sin(\delta_{\vartheta_{3dB}}))}{I_0} \right) = -3 \quad (1.17)$$

for $\sin(\delta_{\vartheta_{3dB}})$. $I(\cdot)$ is the intensity distribution of the Fraunhofer diffraction pattern. For the rectangular aperture case the relationship is then

$$\sin(\delta_{\vartheta_{3dB}}) = 0.64 \frac{\lambda}{D}, \quad (1.18)$$

where $\delta_{\vartheta_{3dB}}$ is the $-3dB$ angular resolution and D is the size of the aperture in the particular dimension of the rectangular aperture. The threshold of $-3dB$ corresponds approximately to half the maximal intensity I_0 .

In remote sensing, one is eventually interested in the spatial resolution, i.e. the resolution that is achieved when observing an object from a particular distance. The *spatial resolution* δ_{3dB} that is obtained by illuminating an object using one single radar antenna of aperture D at a distance R is

$$\delta_{3dB}(R) = a \sin \left(0.64 \frac{\lambda}{D} \right) R. \quad (1.19)$$

With respect to radar remote sensing two basic essentials can be drawn from these reflections:

1. A smaller aperture (antenna) has a lower directivity, a lower angular resolution, and a larger beamwidth.
2. The final spatial resolution is directly proportional to the distance of observation R , which means that the spatial resolution deteriorates with increasing distance of observation.

1.2.3 Synthesizing a Larger Aperture

The basic concept of aperture synthesis consists of appropriately combining the electromagnetic waves, which are back-scattered from an object of interest, as they are measured at *different sensor locations*. Thereby, an aperture of a size a hundred to several thousand times larger than the actual aperture of a real antenna can be simulated. As a consequence, the main lobe of the synthetic antenna is extremely narrow leading to a high resolution in the dimension where

the aperture synthesis is performed. In SAR remote sensing, this is usually the direction of the motion vector of the sensor, called the *azimuth* direction. In multibaseline SAR configurations, such as SAR tomography (treated in Publication 2, 3, and 4 of this thesis), a synthetic aperture is also built in the *normal direction*, which is the direction orthogonal to both, the azimuth direction and the line of sight.

Bearing in mind the Huygens-Fresnel principle once more, where the real aperture is thought of to be composed of an infinite number of secondary wavelets, which radiate in phase, one can extend this thought to subsequently placing antennas to form an array, and where for all individual antennas an infinite number of secondary wavelets radiate in phase. However, as the synthetic aperture increases, the Fraunhofer approximation is no longer valid. As a consequence, the phase of the electromagnetic waves that are recorded at the different sensor locations have to be altered such that the wavefronts that are echoed by the object of interest interfere constructively for the location of where the object is situated.

Given that premise, the beam divergence angle ϑ_{SA} obtained for the synthetic aperture of length L can be written, analogously to the real aperture case [see (1.15)], as

$$\sin(\vartheta_{SA}) = \frac{\lambda}{L} . \quad (1.20)$$

Using the fact that $x/z_0 = \sin(\delta_\vartheta)$ and setting $x = L/2$, the length of the synthetic aperture L , which varies as a function of the range distance, can be expressed in terms of the wavelength λ and the aperture D of the real antenna:

$$\frac{L/2}{z_0} = \sin(\delta_\vartheta) = \frac{\lambda}{D} . \quad (1.21)$$

Combining (1.20) and (1.21), we obtain the following expression for the divergence angle ϑ_{SA} of the synthetic aperture

$$\sin(\vartheta_{SA}) = \frac{D}{2z_0} . \quad (1.22)$$

The maximal spatial resolution δ_{SA} obtained with the full synthetic aperture is then

$$\delta_{SA} = \sin(\vartheta_{SA})z_0 = \frac{D}{2} . \quad (1.23)$$

Hence, the beneficial characteristics of aperture synthesis can be summarized as follows:

1. A very high spatial resolution of half the aperture size of the real antenna is obtained in the dimension in which the synthetic aperture is built. A smaller real aperture (antenna), which has a lower directivity, that is, a larger beamwidth, is favorable in order to obtain a higher resolution because individual radar echoes measured at different azimuth positions can be combined only as long as the object lies within the beamwidth of the real antenna.
2. Most importantly, the resolution is *independent* of the distance of observation.

The above analysis is valid for an imaging mode called stripmap mode and the additional constraint that the pointing direction of the antenna is orthogonal to the synthetic antenna array during the whole data acquisition period. In contrast, in spotlight mode imaging the antenna beam is steered, mechanically or electronically, such that the scene of interest is illuminated over a longer period of time and, thereby, the resolution in azimuth direction can be further enhanced [9, 10].

Similar to aperture synthesis in azimuth direction, a synthetic aperture can also be formed in the normal direction, thus yielding a two-dimensional synthetic aperture. This concept is called multibaseline SAR interferometry or SAR tomography. In practice, the main difference lies in the fact that multiple, ideally parallel-running sensor trajectories are required in order to build the synthetic aperture in the normal direction. Since SAR tomography is discussed at length in Publication 2, 3, and 4 of this dissertation this topic is not repeated here.

So far, we have been talking about the imaging resolution in the two dimensions of the planar antenna, assuming that an infinitesimally short pulse consisting of a monochromatic wave accurately indicates the propagation delay to the object of interest. For pulsed radar systems, a high resolution in range direction (line of sight) is obtained by typically using a frequency-modulated pulse (chirp) of a length of several microseconds; each radar echo is then compressed later by matched filtering with a replica of the original frequency-modulated pulse. Without going into further detail here, the resolution δ_r in range direction is given for the case of a linear frequency modulation leading to a resolution that is inversely proportional to the bandwidth B :

$$\delta_r = \frac{c}{2B} . \quad (1.24)$$

c is the propagation speed of the electromagnetic wave.

Herewith, we conclude this brief introduction to aperture synthesis and imaging resolution. For a detailed introduction to the signal model of synthetic aperture radar systems the interested reader is again referred to references [8–11].

Radar remote sensing is only one of many fields, where imaging by aperture synthesis is performed. Examples of such imaging systems include very large baseline interferometry (VLBI) in radio astronomy, synthetic aperture sonar (SAS) (see e.g. [15]) in the maritime environment, ultrasonic synthetic aperture systems in non-invasive diagnostic medicine, as well as seismic sounding in geophysical exploration [16]. In astronomy, even optical aperture synthesis (OAS) using an array of telescopes is possible, today, a notable difference being that the large aperture cannot be synthesized by digital post-processing but has to be correlated by a dedicated optical system (see e.g. the Very Large Telescope, VLT). Case studies have also been made for future OAS earth observation systems from a geostationary orbit. Similar concepts are found in speech and acoustic signal processing and wireless communication systems, mostly under the name of direction-of-arrival estimation (DOA). The fundamental framework of all these techniques is called *array signal processing*.

As diverse as the fields where aperture synthesis is applied, as diverse is the terminology. Thus, a number of terms which essentially all describe the resolution enhancement by means of aperture synthesis are listed here non-exhaustively: (azimuth) focusing, (digital) beamforming, matched filtering, correlation with a reference function, wave equation migration, back-projection, and direction-of-arrival estimation.

1.3 Imaging Paradigms in Synthetic Aperture Radar Data Processing

Imaging essentially means inverting the measurement process in an adequate way in order to obtain a representation of the objects of interest.

Over the years, a number of different algorithms have been developed or adapted for SAR image processing. The goal of this section is to give a very brief overview of three imaging paradigms that are commonly used in SAR signal processing. An in-depth review of available SAR focusing algorithms is out of the scope of this thesis. A number of excellent textbooks are available that cover this topic at

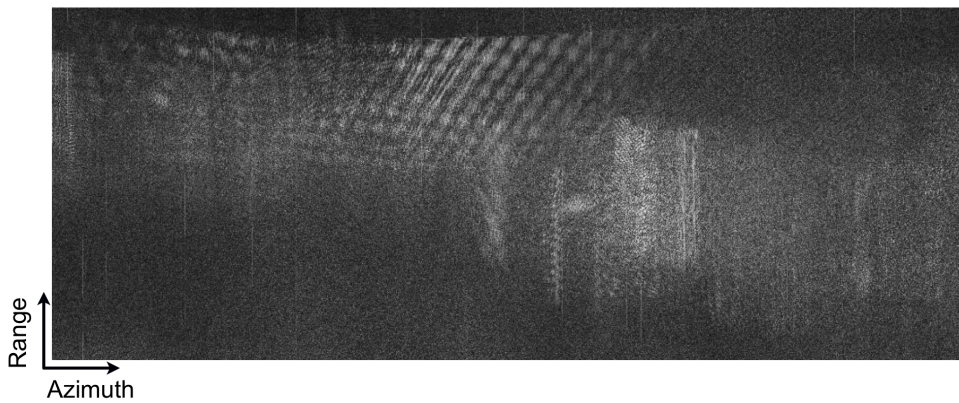
length and in great detail: see, for instance, Curlander and McDonough [8], or Cumming and Wong [11], who highlight and compare a number of focusing algorithms from a spaceborne SAR perspective and, therefore, predominantly for narrow bandwidth and narrow beamwidth systems. Carrara et al. [9], Jakowatz et al. [17], and Soumekh [10] all treat SAR signal processing from an airborne SAR perspective. Thus, compensation of irregular motion receives considerable attention in these works.

1.3.1 Basic Focusing Steps

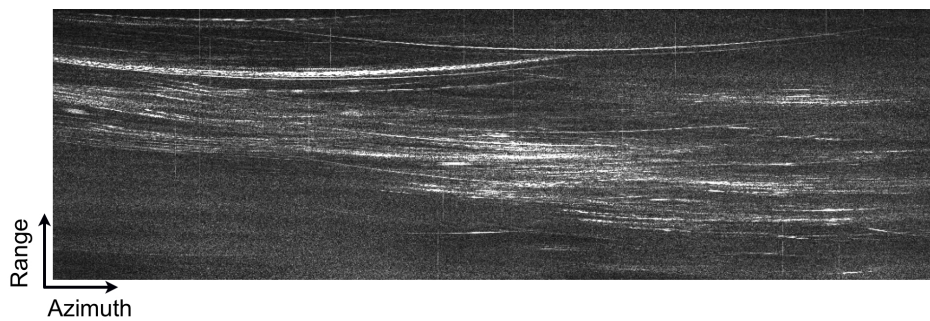
With the exception of the chirp-scaling based algorithms, all SAR imaging techniques can be split into a sequence of focusing the data in the range (fast-time) direction (range compression, range matched filtering) and synthesizing a large aperture in azimuth (slow-time) direction. In Fig. 1.2, an example of an airborne SAR data set is given that visualizes the SAR data as amplitude representations at different stages of the image formation process: 1) before any manipulation, i.e. the data is displayed as taken by the sensor before focusing (raw data), 2) at an intermediate stage, after range matched filtering (range-compressed data), and 3) after aperture synthesis has been performed (azimuth-focused data).

In the range-compressed data representation shown in Fig. 1.2(b), the two-dimensional, hyperbolic nature of the target signal history becomes obvious: the target appears to be smeared along a hyperbolic trajectory. This non-trivial range/azimuth coupling is exactly what makes synthetic aperture imaging a challenging task. The signal contributions of a point target appear at range distances that vary from pulse to pulse along the azimuth direction, an effect called “range cell migration” (RCM), or “motion through resolution cells”. In addition, perturbation of the signal history in the airborne case, caused by irregular motion of the sensor and varying propagation delays due to the atmospheric conditions, further complicate the image inversion.

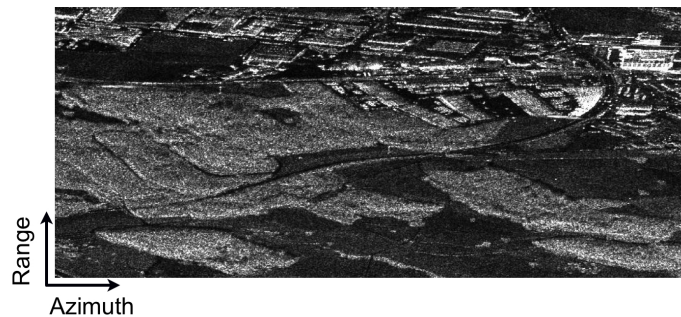
In the following, the most common SAR imaging algorithms are discussed briefly in the context of three imaging paradigms, the range-Doppler paradigm, the wavenumber domain reconstruction paradigm, and the tomographic paradigm.



(a)



(b)



(c)

Figure 1.2: Exemplary SAR data representations: a) raw data, as measured by the sensor, b) range-compressed data (i.e. after range matched filtering) c) azimuth-focused data (i.e. after aperture synthesis). Note the hyperbolic shape of bright objects as they appear at different range distances in subsequent pulses within the range/azimuth geometry of the range-compressed image. Evidently, the signal processing steps that are needed to build the synthetic aperture are of a two-dimensional nature (in contrast to the one-dimensional range compression).

1.3.2 Range-Doppler Paradigm

Following this paradigm, an efficient processing is achieved by making use of the fact that in SAR remote sensing, the sensor is in motion. Thus, the signal of a point target experiences a Doppler frequency shift depending on the projection of the relative velocity vector onto the connecting line between the sensor and the target. Algorithms that can be assigned to the range-Doppler paradigm are the range-Doppler algorithm [18–20], the chirp scaling algorithm [21], as well as further extensions of the chirp scaling algorithm such as for squinted geometry in [22], the airborne case including motion compensation [23], and a more generalized formulation for processing of air- and spaceborne stripmap SAR data and even ScanSAR data [24]. Another chirp-scaling-based framework for higher order approximation of the hyperbolic range equation, called generalized frequency domain algorithm, is described by Zaugg and Long [25].

The basic range Doppler algorithm involves the assumption of a narrow bandwidth and a narrow beamwidth as well as a parabolic approximation (corresponding to the Fresnel approximation of the diffraction pattern) of the hyperbolic shape of the signal history. A further, distinct feature of the range Doppler algorithm is that the range cell migration correction (RCMC) is performed in the range (time) - Doppler (frequency) domain where targets lying at a certain range distance are superposed as they have the same Doppler characteristics. The RCMC is performed using an interpolation scheme, the choice of which considerably affects the quality of the final image.

The chirp scaling algorithm avoids that critical and time consuming interpolation step. It consists basically of multiplying the SAR data in the range-Doppler domain with a quadratic phase function (chirp scaling) in order to equalize the range cell migration to a reference range, followed by a range compression and a secondary range compression (SRC) in the wavenumber domain. The SRC is strictly correct only for one reference range and it is updated as a function of the Doppler frequency. The SAR data are imaged without any data interpolation within this focusing procedure. The chirp scaling algorithm in its standard formulation employs a parabolic approximation of the hyperbolic range history. Varying the Doppler rate with range is possible. The RCMC is carried out differentially by means of the chirp scaling operation in the range Doppler domain.

The accuracy of both, the range Doppler algorithm and the (extended) chirp scaling algorithm is limited for higher bandwidths and wide beamwidths. While the generalized frequency domain algorithm is theoretically suitable to process

SAR data from systems with wide beamwidths, large bandwidths, or low carrier frequencies, no concept that can handle severe deviations from a linear sensor trajectory has been presented so far.

In [26] the so-called polar format algorithm was introduced, that has later been reformulated from a tomographic point of view. The polar format algorithm is particularly useful for spotlight mode SAR data processing.

1.3.3 Wavenumber Domain Paradigm

The wavenumber domain algorithm, also called range migration algorithm, or $\omega - k$ algorithm [27–30] allows for an approximation-free image reconstruction based on the exact inversion (as far as the phase history is concerned) of the wave equation. The only approximation involved in this reconstruction scheme is the principle of stationary phase which is used for an explicit evaluation of the Fourier transform of the signal model. The principle of stationary phase is valid in the standard monostatic scenario except in the extreme case of frequencies close to zero [25]. Another exception where the principle of stationary phase is not valid is an extreme bistatic case, such as a combined spaceborne-airborne bistatic data acquisition [31].

The characteristic feature of this algorithm is a nonlinear coordinate transform also termed Stolt mapping [16], which stems from a seismic migration technique.

Theoretically, the $\omega - k$ algorithm is a very elegant and approximation-free solution of the SAR image reconstruction problem. In practice, however, several drawbacks become evident: for instance, the exact $\omega - k$ algorithm lacks the possibility to account for a range varying adjustment of the Doppler rate, which renders it to be an option only for airborne SAR remote sensing. Therefore, approximations of the exact $\omega - k$ algorithm have been developed for small bandwidth and narrow beamwidth spaceborne systems. One of these approximative solutions is called monochromatic $\omega - k$ developed by Rocca et al. [32]. It is an approximation of the strict $\omega - k$ algorithm in two ways: The non-linear Stolt interpolation is replaced by a multiplication by a linear phase term in the range-Doppler domain. Consequently, only the carrier frequency is mapped correctly, hence, the attribute monochromatic. In addition, a quadratic approximation is used instead of the exact transfer function. The main advantage of the monochromatic $\omega - k$ algorithm is that it needs no interpolation and therefore it is very efficient.

Another interpolation-free imaging algorithm deduced from the wavenumber domain algorithm is the range stacking algorithm [33] where a (range-varying) matched filter is explicitly calculated for each range bin, followed by a slow-time inverse Fourier transform. In the original wavenumber domain algorithm, by contrast, the matched filter is applied in the two-dimensional wavenumber domain for one reference range. Thus, the Stolt mapping of variables $k_r = \sqrt{4k^2 - k_u^2}$ requires a delicate interpolation of non-linearly spaced data points to regular grid points in the (k_r, k_y) domain. The range stacking algorithm is computationally more expensive than the wavenumber domain algorithm, but due to the fact that the azimuth focusing can be performed independently for each range bin, the image formation can be parallelized with ease. In addition, it features the advantage that no interpolation artifacts are present in the final image.

In the airborne case, however, another problem may occur in the sense that strong deviations from a linear trajectory, especially in combination with rugged terrain, cannot be corrected for adequately.

1.3.4 Tomographic Imaging Paradigm

In a pioneering paper, Munson et al. [34] have highlighted the similarity of spotlight mode SAR data and tomographic data as obtained from e.g. X-ray computerized tomography devices. They gave a two-dimensional formulation of spotlight SAR imaging in terms of the projection slice theorem known from computer-aided tomography [35]. The signal received at each antenna position is interpreted as a portion of the Fourier transform of a central projection of the imaged area. This interpretation allows for a geometry-based or Radon-transform-based instead of a Doppler-shift-based understanding of the synthetic aperture imaging process. In that paper [34], the polar format algorithm [26], originally formulated in a range-Doppler sense, is reinterpreted and opposed to a back-projection algorithm. Jakowatz and Thompson [36] have extended the two-dimensional view towards a three-dimensional tomographic formulation of spotlight mode SAR. However, the polar format algorithm is again an approximation of the exact image formation process in the sense that a plane wave approximation is used. This limits the scope of application to narrow-beamwidth systems and spotlight processing of limited-sized patches in terms of the target area [10].

Another instance of the class of tomographic imaging algorithms is called time-

domain back-projection (TDBP). In contrast to all frequency-domain based reconstruction methods, TDBP theoretically allows for a non-linear aperture shape and incorporation of terrain models into signal processing in a stringent way. The idea of back-projecting the measured data pulse by pulse onto a two- or three-dimensional image space is a very natural solution of the inversion problem: For each sensor position, the range-compressed signal is spread (back-projected) along the spherical shape of constant range in the monostatic case, or along the ellipsoidal shape of constant bistatic range in the bistatic SAR case. Basically, the coherent superposition of the back-projected signals at different range distances and for all antenna positions within the synthetic aperture (as obtained at the pixel locations of the reconstruction grid) yields the final focused SAR image.

It has been stated by Ulander et al. [37] that in particular for airborne wide-beamwidth systems, an extreme case is the CARABAS II sensor [38], the TDBP supersedes the frequency domain algorithms. The TDBP can be regarded as a generalization of the standard beamforming or delay-and-sum approach, on the one hand, or matched filtering of a known signal embedded in Gaussian noise by means of a spatially varying reference kernel for each pixel location on the reconstruction grid, on the other hand.

In summary, every efficient frequency-domain based SAR imaging algorithm has its shortcomings in one or another configuration, whereas the only shortcoming of the TDBP approach is its high computational cost. This adverse property can be alleviated considerably by parallelization and due to its aptitude for implementation on graphics processing unit (GPU)-based high-performance computing hardware. Therefore, the high computational cost is not a major drawback for most applications except real-time imaging. In addition, there are also fast back-projection processing methods [37, 39] available, which, however, trade the phase accuracy for higher processing speed.

As the imaging algorithm developed during this thesis is based on time-domain back-projection, the latter shall be discussed in some detail in the next paragraph.

1.3.5 Time-Domain Back-Projection

The development of the system model of TDBP reproduced in this section has originally been published in a slightly modified version by Frey et al. [40].

In the following, the system model of TDBP processing as proposed in [37] is briefly revised and then rewritten as a function of the three-dimensional position of a point in the reconstruction grid, which is the convenient form for our purpose. Reference [37] gives a comprehensive overview of TDBP and of fast back-projection techniques, which make use of approximations in order to reduce the computational burden. Another source which extensively discusses the subject is [10].

Assuming a linear sensor path the two-way response g for a single point target can be written as a function of the cylinder coordinates (ρ, θ, x) where ρ is the range distance at the point of closest approach between sensor and target, θ is the elevation angle, and x is the azimuth position along the linear flight path:

$$g(R, x) = A(.) \cdot \sigma_0 \cdot \frac{p_{rc}(R - \sqrt{(x - x_0)^2 + \rho_0^2})}{(x - x_0)^2 + \rho_0^2} . \quad (1.25)$$

R is the range distance, $A(.)$ the amplitude function representing the antenna gain pattern (AGP), σ_0 the reflectivity of the point target at position (ρ_0, θ_0, x_0) , and p_{rc} is the demodulated, range-compressed pulse.

The focused SAR signal s after TDBP at the range/azimuth position (ρ, x) is:

$$s(\rho, x) = \sum_{x'} g(R, x) \cdot R \cdot \exp(j2k_c R) , \quad (1.26)$$

where $R = \sqrt{(x' - x)^2 + \rho^2}$ is the range distance, x' the along-track integration parameter, $k_c = 2\pi f_c/c$ the central wavenumber corresponding to the carrier frequency f_c , and c is the speed of light. The exponential term brings the demodulated signal back to its original bandpass form.

Generalising to an arbitrary sensor path the two-way response g for a single point target at position \vec{r}_0 can be written as:

$$g(R, \vec{r}_S) = A(\vec{r}_S, \vec{r}_0) \cdot \sigma_0 \cdot \frac{p_{rc}(R - |\vec{r}_S - \vec{r}_0|)}{|\vec{r}_S - \vec{r}_0|^2} , \quad (1.27)$$

where $A(\vec{r}_S, \vec{r}_0)$ is the amplitude function representing the antenna gain pattern, σ_0 the reflectivity of the point target at position \vec{r}_0 , p_{rc} the demodulated and range-compressed pulse, \vec{r}_S the three-dimensional position vector of the sensor, and R the range distance.

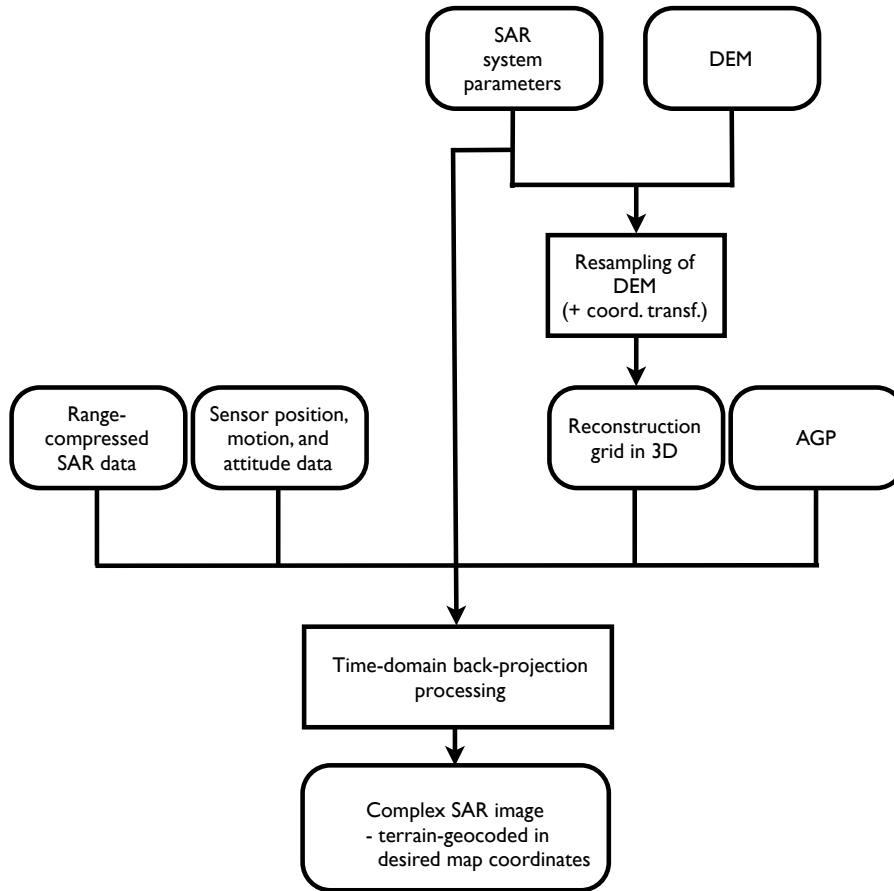


Figure 1.3: Flow diagram of the time-domain back-projection based synthetic aperture radar processor.

In order to be able to back-project the data directly to a three-dimensional reconstruction grid consisting of the grid points \vec{r}_i we want to express the back-projected signal s not as a function of the range position ρ and the sensor position \vec{r}_S , but as a function of the grid point \vec{r}_i :

$$s(\vec{r}_i) = \sum_{j=a(\vec{r}_i)}^{b(\vec{r}_i)} g(|\vec{r}_i - \vec{r}_{S_j}|, \vec{r}_{S_j}) \cdot |\vec{r}_i - \vec{r}_{S_j}| \cdot \exp(j2k_c|\vec{r}_i - \vec{r}_{S_j}|) , \quad (1.28)$$

where a and b are the indices of the first and last sensor position, respectively, the echo of which still contributes to the grid position \vec{r}_i . This means that we sum up the contributions from those sensor positions \vec{r}_{S_j} which build the synthetic aperture for the grid position \vec{r}_i . Note that a and b vary as a function of the grid position \vec{r}_i .

In Fig. 1.3, the flow diagram of the TDBP-based synthetic aperture radar processor is shown. A graphical representation illustrating the SAR data acquisition geometry is given in Fig. 2.2, p. 45.

1.4 Rationale of Dissertation

1.4.1 Motivation

Advanced imaging modes in SAR remote sensing, such as efficient corridor mapping along nonlinear features of interest, dual- and multibaseline (polarimetric) interferometry, SAR tomography, as well as bistatic and multistatic imaging, potentially offer augmented capabilities in observing and monitoring the environment [31, 41–47]. Fields of application that would benefit from such new imaging modes include forestry management, supporting the understanding of the global carbon cycle, agriculture monitoring, infrastructure planning, development and maintenance, coastal management, risk management, floodplain mapping, disaster response and recovery, real estate asset management, telecommunications, network planning, oil, gas, and mineral exploration, as well as defense and intelligence.

Today, a large number of airborne SAR systems at a wide range of frequencies are already available. These airborne sensors serve as data and application providers, and as a testbed for spaceborne missions, as well as a data source for new, experimental imaging modes. In addition, due to technical advances in sensor and satellite technology, sophisticated satellite acquisition modes, such as formation flying for single-pass interferometry and potentially even for tomographic applications [46, 47], will be available in the near future (TanDEM-X is scheduled for launch in 2010, and Tandem-L is in a pre-phase A stadium). They will foster the development of a broad range of new applications and data products based on nonstandard imaging modes. The implementation of new applications based on advanced acquisition geometries and multiple sensor trajectories requires that SAR image processing algorithms which are more flexible than the standard frequency domain approaches (range-Doppler, ω -k, (extended) chirp scaling) be developed and tested under these nonstandard imaging modes.

For most purposes, except for real-time or for quasi real-time applications, the data quality (high focusing quality, phase preservation, radiometric and geometric fidelity) of SAR remote sensing products stands way above all other

requirements. Clearly, time-domain back-projection based imaging is the only imaging philosophy that provides an adequate framework to tackle the challenges of *all* these different SAR imaging acquisition modes, while still providing high-quality, phase preserving SAR images [37]. Nevertheless, within the SAR remote sensing community a lot of effort has been put into designing fast algorithms [18–31, 34, 36] that are more or less restricted to certain acquisition scenarios and system parameters such as frequency band, bandwidth and beamwidth, thereby trading flexibility and quality for speed. Although the potential of TDBP with respect to solving imaging problems of intricate nature is a well-known and acknowledged fact [8, 10, 20, 37] hardly any work has been done so far to demonstrate the feasibility by means of experimental data. With technical advances in GPU-based high performance computing which, by design, support highly parallelizable tasks, TDBP processing even more gains in attractiveness by further diminishing the often cited time factor [48].

In order to expand the range of applications towards nonstandard acquisition scenarios such as SAR imaging along highly nonlinear flight tracks and multi-baseline SAR tomography time-domain based approaches provide an adequate framework to investigate and potentially realize a high quality reconstruction of more complex SAR data acquisition modes.

Nonlinear Flight Tracks

The most general SAR data acquisition scenario involves highly nonlinear sensor paths in a monostatic or multistatic configuration over rugged terrain, possibly also involving multiple sequential overflights (repeat-pass). On the other hand, standard frequency domain algorithms typically assume a strictly linear sensor path [8–11]. In the airborne case, the deviations from the ideally linear sensor path are compensated to a certain extent—requiring an external digital elevation model if a more accurate correction shall be obtained [49–51]. Such high precision motion compensation increases the computational complexity considerably, and, still, the overall shape of the trajectory has to be approximately linear in order to obtain images of high quality.

However, SAR systems mounted on small aircraft or drones may exhibit highly nonlinear sensor trajectories to the extent that a model of a linear sensor trajectory can not be justified. Influencing factors include rugged topography, atmospheric turbulence, and, particularly, the need for more flexibility in mission design. Potential application scenarios include corridor mapping of curvilinear

ear areas of interest, such as rivers and nearby potential flooding areas, traffic routes, or pipelines using airborne or drone-based SAR systems. In such cases, the possibility to acquire SAR data along a nonlinear trajectory would provide a more cost-effective and time-saving data acquisition compared to repeatedly flying linear tracks to cover the area of interest. Ideally, the trajectory of the sensor follows the shape of the feature of interest, which renders the model assumption of a single linear trajectory, upon which the standard frequency-domain processing methods are based, insufficient. Thus, more flexible processing approaches have to be investigated to provide SAR-based corridor mapping. Time-domain back-projection potentially offers a number of advantages with respect to high-quality image processing of SAR data of such intricate nature.

Tomographic SAR Imaging of Forests

Finding new ways to gain or improve the knowledge of the structure and the back-scattering behavior of forests in order to estimate biophysical parameters using synthetic aperture radar data has become a major research topic within the SAR remote sensing community (see e.g. [43, 45, 52–64]).

Several prospective spaceborne SAR missions, such as BIOMASS (ESA) [65, 66] at P-band, Tandem-L [67, 68], and DESDynI (NASA) [69], both at L-band, aim at the measurement of the carbon stock by means of (interferometric) synthetic aperture radar data—or a combination of synthetic aperture data and spaceborne LiDAR data in the case of the DESDynI mission concept—by assessing the above ground biomass of forests as well as forest dynamics such as the amount of deforestation and re-growth on a global scale.

A good understanding of the interaction of microwaves at L-band and P-band with vegetation cover, and in particular, with forests, is an indispensable basis for developing reliable biomass products. It has been reiterated in literature, that simple back-scattering based measurement of the biomass is not feasible for dense forested areas due to signal saturation around 100 t/ha at L-band and 200 t/ha at P-band [52, 70–72]. Therefore, additional measures such as the forest height, involving the extraction of the underlying terrain height, and structural information about the forest are needed. As stated in the recommendations of the PolInSAR 2009 workshop [73] there is still a need for research about the interactions of microwaves at different frequencies within the vertical structure of forested areas and its underlying terrain. The vertical forest structure and terrain reflectivity under vegetated canopies, including the polarimetric signature,

need to be investigated. SAR tomography has the potential to gain such three-dimensional structural information about a forest following a non-model-based approach [43–45].

1.4.2 Objectives

As a common denominator of this work stands the realization of a high-precision SAR imaging tool that is, compared to standard frequency domain SAR processing algorithms, more flexible in terms of both, the type of acquisition mode and the characteristics of a SAR system (airborne and spaceborne, narrow and wide bandwidth or beamwidth, and low to high frequency). On the basis of this newly developed time-domain back-projection based SAR processor⁴ a number of open questions were investigated related to SAR imaging and resulting new data products obtained from airborne data acquisitions that involve 1) a highly nonlinear sensor trajectory, such as corridor mapping, and 2) three-dimensional imaging of multibaseline SAR data of forested areas by means of SAR tomography. To this end, two airborne SAR experiments were designed, which were flown by the German Aerospace Center’s E-SAR system in September 2006. In the first experiment, three highly nonlinear sensor trajectories and a quasi-linear reference track were flown over an airfield. The second experiment consisted of two multibaseline data sets (16 tracks at L-band, 11 tracks at P-band) with a layout optimized for tomographic imaging of a forested area.

The focus of Publication 1 “*Focusing of Airborne Synthetic Aperture Radar Data From Highly Nonlinear Flight Tracks*” is on a performance analysis of two-dimensional SAR imaging from *highly nonlinear* flight paths. This research picks up a thread started by the work of Soumekh [11], who treated the problem of processing SAR data obtained from nonlinear flight paths from an entirely theoretical standpoint, and who only employed a two-dimensional formulation of the geometry instead of a more realistic three-dimensional formulation. Further, practical considerations such as an adequate description of how a changing antenna pointing direction is handled over azimuth were omitted. Publication 1 attempts to fill this gap by analyzing the imaging performance of two algorithms, a new TDBP-based approach and a patch-wise frequency-domain pro-

⁴The TDBP processor developed during this work has been successfully tested for airborne and spaceborne SAR data sets, at P-band (E-SAR, OrbiSAR), L-band (E-SAR, ALOS-PALSAR), C-band (Envisat ASAR), X-band (E-SAR, OrbiSAR), and Ka-Band (FGAN Memphis), thus, for low and high carrier frequencies, narrow and relatively wide beamwidth, as well as high-resolution SAR systems.

cessing approach employing extended chirp scaling and mosaicking (ECS&M). The analysis is performed by means of simulated data as well as experimental airborne SAR data exhibiting highly nonlinear sensor trajectories.

The main research question related to this first topic is:

- What is the imaging performance of TDBP as opposed to the ECS&M approach and are these methods suitable with respect to potential applications such as corridor mapping along nonlinear features of interest?

The second major topic treated in this thesis concerns three-dimensional imaging, also termed SAR tomography, of forested areas by means of airborne multibaseline SAR data at P-band and L-band. In terms of data, a research gap has been identified in that no P-band tomographic SAR data existed so far. With the experimental data acquired during the SWISAR 2006 airborne SAR campaign this gap could be closed and, in addition, tomographic data at L-band *and* P-band was available at the same forest test site, for the first time. In terms of the processing technique the TDBP algorithm provides an adequate framework for tomographic SAR data, since such data is typically subject to nonuniform and sparse sampling in the normal direction. TDBP maintains the entire three-dimensional geometric relationship between the measured sensor positions and the illuminated area while focusing the data. Thus, the complex geometry of multibaseline airborne SAR data is handled appropriately. The objectives of this work are 1) to present a TDBP-based SAR tomography processing framework including a three-dimensional, pure TDBP approach (in Publication 2), as well as improved multilook-based methods such as multilook standard beamforming (MLBF), robust Capon beamforming (RCB), and multiple signal classification (MUSIC) beamforming (in Publication 3), and 2) to contribute towards an improved understanding of the back-scattering behavior of forested areas at frequencies of observation at L-band and P-band (Publication 4).

The focus of Publication 2 “*Tomographic Imaging of a Forested Area by Airborne Multibaseline P-Band SAR*” lies on reporting the investigations related to the development of a highly accurate TDBP-based tomographic imaging approach, which is less sensitive to sparse and irregular sampling than Fourier-based methods. As a result, for the first time, tomographic images of a forested area at P-band were presented in Publication 2.

The main research question related to Publication 2 is:

- What is the imaging performance obtained with a three-dimensional pure TDBP approach when tomographically imaging a forested area at P-band and where are the main backscattering sources located?

In Publication 3 “*3D SAR Imaging of a Forest Using Airborne Multibaseline Data at L- and P-Band*”, three tomographic focusing techniques, MLBF and the two super-resolution methods, RCB and MUSIC, are analyzed and their imaging performance is assessed for different baseline configurations and at both frequencies. The goal is to optimize the detection and exact localization of backscattering sources within the forest volume in order to separate contributions from the canopy level and the ground level, respectively.

The main research questions related to Publication 3 are:

- What is the imaging performance obtained with the three different tomographic imaging approaches: multilook standard beamforming, robust Capon beamforming, and multiple signal classification at L-band and P-band?
- What is the imaging performance using the full set of baselines as compared to a reduced set?

In Publication 4 “*Analyzing Tomographic SAR Data of a Forest With Respect to Frequency, Polarization, and Focusing Technique*” the resulting polarimetric three-dimensional data products are subject to a comparison and cross-validation with a digital elevation model and a digital surface model obtained from airborne laser scanning. The aim is to point out which features of the forest and its underlying terrain are actually measured consistently as a function of the parameters frequency, polarization, and focusing technique. The results are discussed with respect to the question whether the desired information, forest structure and forest height, can be derived from the SAR tomography data sets.

More specifically, the main research questions addressed in Publication 4 are:

- What features of the forest (canopy top, forest structure, terrain level) can be imaged at the different frequencies and polarization channels and using different focusing techniques?
- What types of scattering mechanisms are found by applying polarimetric decompositions to the three-dimensional tomography data sets at both frequencies?
- Is the information obtained consistent with the cross-reference in the form of a digital surface model and a digital elevation model obtained from

airborne laser scanning?

1.4.3 Structure of the Thesis

Chapters 2 to 5 of this thesis are each self-contained individual studies representing material that has already been published in peer-reviewed scientific journals or has been submitted, recently. Thus, each chapter can be read autonomously. In particular, each chapter is composed of an abstract, an introduction to the subject, a description of the methods and data used, followed by a discussion reporting the main findings. An overall synopsis of the thesis is given in Chapter 6.

References

- [1] “German Industry Standard DIN 18716-3:1997-07,” Jul. 1997.
- [2] M. I. Skolnik, *Radar Handbook (2nd Edition)*. McGraw-Hill, 1990.
- [3] O. Frey, E. Meier, D. Nüesch, and A. Roth, “Geometric error budget analysis for TerraSAR-X,” in *Proc. of EUSAR 2004 - 5th European Conference on Synthetic Aperture Radar*, Ulm, Germany, May 2004, pp. 513–516.
- [4] M. Jehle, O. Frey, D. Small, E. Meier, and D. Nüesch, “Improved knowledge of SAR geometry through atmospheric modelling,” in *Proc. of EUSAR 2004 - 5th European Conference on Synthetic Aperture Radar*, Ulm, Germany, May 2004, pp. 909–911.
- [5] M. Jehle, D. Perler, D. Small, A. Schubert, and E. Meier, “Estimation of atmospheric path delays in TerraSAR-X data using models vs. measurements,” *Sensors*, vol. 8, no. 12, pp. 8479–8491, 2008.
- [6] M. Jehle, M. Rüegg, L. Zuberbühler, D. Small, and E. Meier, “Measurement of ionospheric Faraday rotation in simulated and real spaceborne SAR data,” *IEEE Trans. Geosci. Remote Sens.*, vol. 47, no. 5, pp. 1512–1523, May 2009.
- [7] M. Jehle, O. Frey, D. Small, and E. Meier, “Measurement of ionospheric TEC in spaceborne SAR data,” *IEEE Trans. Geosci. Remote Sens.*, vol. 48, no. 6, pp. 2460–2468, Jun. 2010.

-
- [8] J. C. Curlander and R. N. McDonough, *Synthetic Aperture Radar - Systems and Signal Processing*. New York: John Wiley & Sons, 1991.
- [9] W. G. Carrara, R. S. Goodman, and R. M. Majewski, *Spotlight Synthetic Aperture Radar: Signal Processing Algorithms*. Boston, London: Artech House Inc., 1995.
- [10] M. Soumekh, *Synthetic Aperture Radar Signal Processing: with MATLAB Algorithms*. New York: John Wiley & Sons, 1999.
- [11] I. G. Cumming and F. H. Wong, *Digital Processing of Synthetic Aperture Radar Data: Algorithms and Implementation*. Boston, London: Artech House Inc., 2005.
- [12] M. Soumekh, *Fourier Array Imaging*. Englewood Cliffs, NJ: Prentice Hall, 1994.
- [13] M. Born and E. Wolf, *Principles of Optics, 7th ed.* Cambridge University Press, 2009.
- [14] W. Demtröder, *Experimentalphysik 2: Elektrizität und Optik (2. Auflage)*. Berlin Heidelberg: Springer, 1999.
- [15] M. Hayes and P. Gough, “Broad-band synthetic aperture sonar,” *IEEE J. Ocean. Eng.*, vol. 17, no. 1, pp. 80–94, Jan. 1992.
- [16] R. H. Stolt, “Migration by Fourier transform,” *Geophysics*, vol. 43, no. 1, pp. 23–48, Feb. 1978.
- [17] J. Charles V. Jakowatz, D. E. Wahl, P. H. Eichel, D. C. Ghiglia, and P. A. Thompson, *Spotlight-Mode Synthetic Aperture Radar: A Signal Processing Approach*. Norwell, MA: Kluwer Academic Publishers, 1996.
- [18] I. G. Cumming and J. R. Bennett, “Digital processing of SEASAT SAR data,” in *Proc. Rec. IEEE Int. Conf. Acoust., Speech Signal*, vol. 4, Washington, DC, Apr. 1979, pp. 710–718.
- [19] C. Wu, K. Liu, and M. Jin, “Modeling and a correlation algorithm for spaceborne SAR signals,” *IEEE Trans. Aerosp. Electron. Syst.*, vol. 18, no. 5, pp. 563–575, Sep. 1982.
- [20] B. C. Barber, “Theory of digital imaging from orbital synthetic-aperture radar,” *International Journal of Remote Sensing*, vol. 6, no. 7, pp. 1009–1057, 1985.

-
- [21] R. K. Raney, H. Runge, R. Bamler, I. G. Cumming, and F. Wong, "Precision SAR processing using chirp scaling," *IEEE Trans. Geosci. Remote Sens.*, vol. 32, no. 4, pp. 786–799, Jul. 1994.
- [22] G. Davidson, I. G. Cumming, and M. Ito, "A chirp scaling approach for processing squint mode SAR data," *IEEE Trans. Aerosp. Electron. Syst.*, vol. 32, no. 1, pp. 121–133, Jan. 1996.
- [23] A. Moreira and Y. Huang, "Airborne SAR processing of highly squinted data using a chirp scaling approach with integrated motion compensation," *IEEE Trans. Geosci. Remote Sens.*, vol. 32, no. 5, pp. 1029–1040, Sep. 1994.
- [24] A. Moreira, J. Mittermayer, and R. Scheiber, "Extended chirp scaling algorithm for air- and spaceborne SAR data processing in Stripmap and ScanSAR imaging modes," *IEEE Trans. Geosci. Remote Sens.*, vol. 34, no. 5, pp. 1123–1136, Sep. 1996.
- [25] E. C. Zaugg and D. G. Long, "Generalized frequency-domain SAR processing," *IEEE Trans. Geosci. Remote Sens.*, vol. 47, no. 11, pp. 3761–3773, Nov. 2009.
- [26] J. L. Walker, "Range-Doppler imaging of rotating objects," *IEEE Trans. Aerosp. Electron. Syst.*, vol. 16, no. 1, pp. 23–52, Jan. 1980.
- [27] F. Rocca, "Synthetic aperture radar: a new application for wave equation techniques," *Stanford Exploration Project SEP-56*, pp. 167–189, 1987.
- [28] C. Cafforio, C. Prati, and F. Rocca, "SAR data focusing using seismic migration techniques," *IEEE Trans. Aerosp. Electron. Syst.*, vol. 27, no. 2, pp. 194–207, Mar. 1991.
- [29] M. Soumekh, "A system model and inversion for synthetic aperture radar imaging," *IEEE Trans. Image Process.*, vol. 1, no. 1, pp. 64–76, Jan. 1992.
- [30] A. S. Milman, "SAR imaging by omega-k migration," *International Journal of Remote Sensing*, vol. 14, no. 10, pp. 1965–1979, 1993.
- [31] R. Wang, O. Loffeld, Q. Ul-Ann, H. Nies, A. M. Ortiz, and A. Samarah, "A bistatic point target reference spectrum for general bistatic SAR processing," *IEEE Geosci. Remote Sens. Lett.*, vol. 5, no. 3, pp. 517–521, Jul. 2008.
- [32] F. Rocca, C. Prati, and A. Monti-Guarnieri, "New algorithms for processing of SAR data," ESA Contract Report, ESRIN Contract no. 7998/88/F/FL(SC), 1989.

-
- [33] M. Soumekh, “Range stacking: An interpolation-free SAR reconstruction algorithm,” in *Proc. SPIE*, vol. 3370, 1998, pp. 13–24.
- [34] D. C. Munson, Jr., J. D. O’Brien, and W. K. Jenkins, “A tomographic formulation of spotlight-mode synthetic aperture radar,” *Proceedings of the IEEE*, vol. 71, no. 8, pp. 917–925, Aug. 1983.
- [35] A. C. Kak and M. Slaney, *Principles of Computerized Tomographic Imaging*. IEEE Press, 1988.
- [36] C. Jakowatz and P. Thompson, “A new look at spotlight mode synthetic aperture radar as tomography: imaging 3-D targets,” *IEEE Trans. Image Process.*, vol. 4, no. 5, pp. 699–703, 1995.
- [37] L. M. H. Ulander, H. Hellsten, and G. Stenström, “Synthetic-aperture radar processing using fast factorized back-projection,” *IEEE Trans. Aerosp. Electron. Syst.*, vol. 39, no. 3, pp. 760–776, Jul. 2003.
- [38] H. Hellsten, L. M. H. Ulander, A. Gustavsson, and B. Larsson, “Development of VHF CARABAS II SAR,” in *Proc. SPIE*, vol. 2747, Jun. 1996, pp. 48–60.
- [39] A. F. Yegulalp, “Fast backprojection algorithm for synthetic aperture radar,” in *Proc. Rec. IEEE Radar Conf.*, 1999, pp. 60–65.
- [40] O. Frey, E. Meier, and D. Nüesch, “Processing SAR data of rugged terrain by time-domain back-projection,” in *SPIE Vol. 5980: SAR Image Analysis, Modeling, and Techniques X*, 2005.
- [41] G. Vigurs, M. Wood, and M. Jarrett, “Non-linear synthetic aperture radar techniques,” in *Proc. EURAD*, Oct. 2005, pp. 13–16.
- [42] M. Soumekh, “Time domain non-linear SAR processing,” Dept. Elect. Eng., State Univ. New York, Buffalo, Tech. Rep., 2006.
- [43] A. Reigber and A. Moreira, “First demonstration of airborne SAR tomography using multibaseline L-band data,” *IEEE Trans. Geosci. Remote Sens.*, vol. 38, no. 5, pp. 2142–2152, 2000.
- [44] S. Guillaso and A. Reigber, “Polarimetric SAR tomography (POLTOM-SAR),” in *Proc. POLINSAR*, Frascati, Italy, 2005.
- [45] S. Tebaldini, “Algebraic synthesis of forest scenarios from multibaseline PolInSAR data,” *IEEE Trans. Geosci. Remote Sens.*, vol. 47, no. 12, pp. 4132–4142, Dec. 2009.

-
- [46] G. Krieger, A. Moreira, H. Fiedler, I. Hajnsek, M. Werner, M. Younis, and M. Zink, “TanDEM-X: A satellite formation for high-resolution SAR interferometry,” *IEEE Trans. Geosci. Remote Sens.*, vol. 45, no. 11, pp. 3317–3341, Nov. 2007.
- [47] G. Krieger, I. Hajnsek, K. P. Papathanassiou, M. Younis, and A. Moreira, “Interferometric synthetic aperture radar (SAR) missions employing formation flying,” *Proceedings of the IEEE*, vol. 98, no. 5, pp. 816–843, May 2010.
- [48] M. Blom and P. Follo, “VHF SAR image formation implemented on a GPU,” in *IEEE International Geoscience and Remote Sensing Symposium, IGARSS '05.*, vol. 5, July 2005, pp. 3352–3356.
- [49] K. A. Câmara de Macedo and R. Scheiber, “Precise topography- and aperture-dependent motion compensation for airborne SAR,” *IEEE Geosci. Remote Sens. Lett.*, vol. 2, no. 2, pp. 172–176, 2005.
- [50] P. Prats, A. Reigber, and J. J. Mallorqui, “Topography-dependent motion compensation for repeat-pass interferometric SAR systems,” *IEEE Geosci. Remote Sens. Lett.*, vol. 2, no. 2, pp. 206–210, 2005.
- [51] P. Prats, K. A. Câmara de Macedo, A. Reigber, R. Scheiber, and J. J. Mallorqui, “Comparison of topography- and aperture-dependent motion compensation algorithms for airborne SAR,” *IEEE Geosci. Remote Sens. Lett.*, vol. 4, no. 3, pp. 349–353, 2007.
- [52] M. L. Imhoff, “Radar backscatter and biomass saturation: ramifications for global biomass inventory,” *IEEE Trans. Geosci. Remote Sens.*, vol. 33, no. 2, pp. 511–518, Mar. 1995.
- [53] J. Hagberg, L. M. H. Ulander, and J. Askne, “Repeat-pass SAR interferometry over forested terrain,” *IEEE Trans. Geosci. Remote Sens.*, vol. 33, no. 2, pp. 331–340, Mar. 1995.
- [54] R. N. Treuhaft, S. N. Madsen, M. Moghaddam, and J. J. van Zyl, “Vegetation characteristics and underlying topography from interferometric radar,” *Radio Science*, vol. 31, no. 6, pp. 1449–1485, 1996.
- [55] S. R. Cloude and K. P. Papathanassiou, “Polarimetric SAR interferometry,” *IEEE Trans. Geosci. Remote Sens.*, vol. 36, no. 5, pp. 1551–1565, Sep. 1998.
- [56] R. N. Treuhaft and S. R. Cloude, “The structure of oriented vegetation from

- polarimetric interferometry,” *IEEE Trans. Geosci. Remote Sens.*, vol. 37, no. 5, pp. 2620–2624, Sep. 1999.
- [57] J.-S. Lee, S. R. Cloude, K. P. Papathanassiou, M. R. Grunes, and I. H. Woodhouse, “Speckle filtering and coherence estimation of polarimetric SAR interferometry data for forest applications,” *IEEE Trans. Geosci. Remote Sens.*, vol. 41, no. 10, pp. 2254–2263, Oct. 2003.
- [58] R. N. Treuhaft, B. E. Law, and G. P. Asner, “Forest attributes from radar interferometric structure and its fusion with optical remote sensing,” *BioScience*, vol. 54, no. 6, pp. 561–571, 2004.
- [59] B. Hallberg, G. Smith, A. Olofsson, and L. M. H. Ulander, “Performance simulation of spaceborne P-band SAR for global biomass retrieval,” in *Proc. IEEE Int. Geosci. and Remote Sens. Symp.*, vol. 1, Sep. 2004, pp. 503–506.
- [60] O. Frey, F. Morsdorf, and E. Meier, “Tomographic processing of multi-baseline P-band SAR data for imaging of a forested area,” in *Proc. IEEE Int. Geosci. and Remote Sens. Symp.*, Jul. 2007, pp. 156–159.
- [61] O. Frey, F. Morsdorf, and E. Meier, “Tomographic imaging of a forested area by airborne multi-baseline P-band SAR,” *Sensors, Special Issue on Synthetic Aperture Radar*, vol. 8, no. 9, pp. 5884–5896, Sep. 2008.
- [62] M. Nannini, R. Scheiber, and A. Moreira, “Estimation of the minimum number of tracks for SAR tomography,” *IEEE Trans. Geosci. Remote Sens.*, vol. 47, no. 2, pp. 531–543, Feb. 2009.
- [63] R. N. Treuhaft, B. D. Chapman, J. R. dos Santos, F. G. Gonçalves, L. V. Dutra, P. M. L. A. Graça, and J. B. Drake, “Vegetation profiles in tropical forests from multibaseline interferometric synthetic aperture radar, field, and lidar measurements,” *J. Geophys. Res.*, vol. 114, pp. 1–16, Dec. 2009.
- [64] F. Garestier, P. C. Dubois-Fernandez, D. Guyon, and T. Le Toan, “Forest biophysical parameter estimation using L- and P-band polarimetric SAR data,” *IEEE Trans. Geosci. Remote Sens.*, vol. 47, no. 10, pp. 3379–3388, Oct. 2009.
- [65] “Candidate Earth explorer core mission BIOMASS - report for assessment,” ESA SP-1313/2, Tech. Rep., Nov. 2008. [Online]. Available: http://esamultimedia.esa.int/docs/SP1313-2_BIOMASS.pdf
- [66] F. Hélière, C. Lin, F. Fois, M. Davidson, A. Thompson, and P. Bensi, “BIOMASS: A P-band SAR Earth explorer core mission candidate,” in *Proc. IEEE Radar Conf.*, May 2009, pp. 1–6.

- [67] A. Moreira, G. Krieger, I. Hajnsek, K. Papathanassiou, M. Eineder, F. D. Zan, M. Younis, and M. Werner, “Tandem-L: Monitoring the Earth’s dynamics with InSAR and Pol-InSAR,” in *Proc. PolInSAR*, Frascati, Italy (ESA SP-668), Jan. 2009.
- [68] G. Krieger, I. Hajnsek, K. P. Papathanassiou, M. Eineder, M. Younis, F. De Zan, P. Prats, S. Huber, M. Werner, H. Fiedler, A. Freeman, P. Rosen, S. Hensley, W. Johnson, L. Veilleux, B. Grafmueller, R. Werninghaus, R. Bamler, and A. Moreira, “The Tandem-L mission proposal: Monitoring Earth’s dynamics with high resolution SAR interferometry,” in *Proc. IEEE Radar Conf.*, May 2009, pp. 1–6.
- [69] A. Donnellan, P. Rosen, J. Graf, A. Loverro, A. Freeman, R. Treuhaft, R. Oberto, M. Simard, E. Rignot, R. Kwok, X. Pi, J. Blair, W. Abdalati, J. Ranson, H. Zebker, B. Hager, H. Shugart, M. Fahnestock, and R. Dubayah, “Deformation, ecosystem structure, and dynamics of ice (DESDynI),” in *Proc. IEEE Aerospace Conf.*, Mar. 2008, pp. 1–13.
- [70] M. C. Dobson, F. T. Ulaby, T. LeToan, A. Beaudoin, E. S. Kasischke, and N. Christensen, “Dependence of radar backscatter on coniferous forest biomass,” *IEEE Trans. Geosci. Remote Sens.*, vol. 30, no. 2, pp. 412–415, Mar. 1992.
- [71] H. Israelsson, L. M. H. Ulander, J. L. H. Askne, J. E. S. Fransson, P.-O. Frörlind, A. Gustavsson, and H. Hellsten, “Retrieval of forest stem volume using VHF SAR,” *IEEE Trans. Geosci. Remote Sens.*, vol. 35, no. 1, pp. 36–40, Jan. 1997.
- [72] R. F. Nelson, P. Hyde, P. Johnson, B. Emessiene, M. L. Imhoff, R. Campbell, and W. Edwards, “Investigating RaDAR-LiDAR synergy in a North Carolina pine forest,” *Remote Sensing of Environment*, vol. 110, no. 1, pp. 98–108, Sep. 2007.
- [73] “PolInSAR 2009 sorted recommendations,” ESA, Frascati, Italy, Jan. 2009. [Online]. Available: http://earth.esa.int/workshops/polinsar2009/POLInSAR2009_sorted_rec.pdf

2 Focusing of Airborne Synthetic Aperture Radar Data From Highly Nonlinear Flight Tracks

This chapter has been published as: O. Frey, C. Magnard, M. Rüegg, and E. Meier, 2009. Focusing of Airborne Synthetic Aperture Radar Data from Highly Nonlinear Flight Tracks. IEEE Transactions on Geoscience and Remote Sensing, 47(6):1844–1858.

Abstract

Standard focusing of data from synthetic aperture radar (SAR) assumes a straight recording track of the sensor platform. Small nonlinearities of airborne platform tracks are corrected for during a motion-compensation step while maintaining the assumption of a linear flight path. This paper describes the processing of SAR data acquired from nonlinear tracks, typical of sensors mounted on small aircraft or drones flying at low altitude. Such aircraft do not fly along straight tracks, but the trajectory depends on topography, influences of weather and wind, or the shape of areas of interest such as rivers or traffic routes. Two potential approaches for processing SAR data from such highly nonlinear flight tracks are proposed: a patch-wise frequency-domain processing and mosaicking technique, and a time-domain back-projection-based technique. Both are evaluated with the help of experimental data featuring tracks with altitude changes, a double bend, a 90° curve, and a linear flight track. In order to assess the quality of the focused data, close-ups of amplitude images are compared, impulse response functions of a point target are analyzed, and the coherence is evaluated. The experimental data were acquired by the German Aerospace Center's E-SAR L-band system.

2.1 Introduction

Processing of raw synthetic aperture radar (SAR) data to obtain focused data products is central to virtually all SAR applications and techniques known at present. While being the first and crucial step towards accurate and reliable results of any SAR application, it is also a delicate one, with strong dependence on the system specifications, flight geometry, and scene properties. For SAR data collected by airborne sensors, the flight path and its incorporation into the processing of the recorded data are of paramount importance. The traditional approach of strip-map SAR begins by assuming an ideal linear flight path. The SAR data are then reassigned to the linear flight path by one or two so-called motion-compensation steps, whereby small deviations of the sensor from the ideal linear trajectory are compensated.

The extended chirp scaling (ECS) algorithm [1], for instance, implements a two-step motion-compensation approach: 1) A first-order range-invariant motion compensation is performed, and 2) a second-order range-dependent motion compensation is executed before the azimuth compression.

However, SAR systems mounted on small aircraft or even drones may exhibit highly nonlinear—if not arbitrary—flight paths, to the extent that a model of a linear sensor trajectory is no longer feasible. This scenario may occur due to various factors such as rugged topography, atmospheric turbulence, and also the need for more flexibility in mission design. Examples include airborne- or drone-based monitoring of curvilinear areas of interest (corridor mapping), such as rivers and nearby (potential) flooding areas or traffic routes.

In such cases, the model assumption of a single linear trajectory, upon which the standard frequency-domain processing methods are based, is not sufficient, and therefore, more flexible processing approaches must be sought after.

2.1.1 Nonlinear Flight Tracks: Previous Work

SAR imaging from nonlinear flight tracks has been an issue of interest for several years. A number of publications that discuss aspects of SAR imaging from nonlinear flight paths have appeared. Soumekh [2] treats the special case of a circular sensor trajectory around the area of interest. In [3] and [4], the idea of using a nonlinear sensor trajectory in the azimuth-elevation plane for tomographic SAR imaging has been proposed. In [5], SAR and other synthetic

aperture imaging systems are considered, in which a backscattered wave is measured from positions along an arbitrary flight path. In [6], 3-D tomographic SAR imaging is investigated for several nonlinear trajectory patterns, with the help of simulated data. The focusing performance is compared for various curved flight tracks, including circles, ellipses, spirals, and random sampling. Most of the simulations are carried out for Ka-band SAR systems; for the image formation, a time-domain correlation algorithm is used. Most recently, Xiang and Rulian [7] and Su *et al.* [8,9] studied the performance of 3-D SAR imaging from nonlinear tracks, mainly in the azimuth-elevation plane, with respect to 3-D target reconstruction using parametric and nonparametric estimation techniques. Vigurs and Wood [10] presented a technique exploiting a nonlinear sensor trajectory to distinguish the Doppler effects of a target's radial velocity from the effect of a cross-range displacement.

The focus of this paper lies on the performance of 2-D SAR imaging from highly nonlinear flight paths. Previous work in this field has been done by Soumekh [11], where the problem of processing SAR data from nonlinear flight tracks is treated in detail and two solutions are proposed. The first solution is processing the data by time-domain back-projection (TDBP). However, the problem is described with the help of a 2-D formulation of the geometry similar to the formulation made in [12], and there is no description of how the changing antenna pointing direction (i.e., the highly varying Doppler centroid) is handled over azimuth. The second solution proposed is an $\omega - k$ -based subaperture processing algorithm, which is claimed to yield superior results as compared with the TDBP approach. Unfortunately, neither of these publications provides results obtained using real SAR data acquired from highly nonlinear flight tracks. This paper attempts to fill this gap by presenting experimental results accompanied by the description and comparison of two potential approaches for processing SAR data acquired from highly nonlinear flight tracks.

2.1.2 TDBP Processing

Although the possibility of correlating SAR data in the time domain has already been discussed by Barber [13] and later by Curlander and McDonough [14] and Soumekh [12], most of the attention in the SAR processing community has been directed toward more efficient frequency-domain focusing techniques. These algorithms are often designed for processing SAR data of a particular sensor or sensor type. Their general applicability is limited by restrictions imposed upon

parameters, such as the maximum chirp bandwidth or the maximum azimuth beam width, and, particularly, the requirement of a regularly-shaped (typically linear) sensor trajectory.

More recently, in [15] and [16], fast back-projection techniques have been described. The algorithm presented in [15] makes use of an approximation in the form of a factorization of both the synthetic aperture and the size of the reconstruction grid. The approach in [16] describes a rather similar scheme, where the synthetic aperture is divided into a number of subapertures, which are then back-projected to a polar coordinate system with a coarse cross-range resolution. After upsampling of the low-resolution (in azimuth) polar grids, these are coherently added to form the final high-resolution image. With the help of such approximations, the computational complexity can be reduced, albeit at the cost of less accurate phase information. Standard TDBP processing has also been discussed in [12]. However, only the cases of a linear flight track with the usual motion errors and the special case of a circular flight track are discussed.

The authors believe that for many scientific purposes, the amount of time spent on SAR raw data focusing, be it in the frequency domain or *even in the time domain*, is rather small, if not negligible, as compared to the overall time spent on data evaluation and the analysis of derived products. In the particular case of TDBP processing, the data can be split into an arbitrary number of patches that can be processed in parallel with very little interprocess communication. An exception is obviously any true real-time SAR application, given the performance of a realistic current hardware environment. However, for most other cases, looking at the total time spent on data processing and exploitation, the often-cited time factor supporting frequency-domain processing techniques diminishes, particularly if traded for processing quality or if applied to nonstandard SAR data-acquisition scenarios, as will be shown in this paper.

As a side benefit, quicklooks can be generated with increasing resolution without additional processing. Furthermore, the processing can be applied to a subregion of the acquired scene, thus saving time by not requiring the rest of the data to be processed at the same resolution. Potentially, data processing could even begin at acquisition time, with contributions from each echo cumulatively and coherently added as the sensor moves along the azimuth direction; one would not need to wait until the correlation length in azimuth has been reached.

The authors therefore believe that it is well worth exploring the possibilities of TDBP processing, with its inherent ability to generate high-quality results even

for SAR data acquired under atypical circumstances.

2.1.3 Aim of This Paper

In this paper, two different approaches that have been identified to be potentially suitable for handling highly nonlinear sensor trajectories are discussed:

1. a piecewise track-linearization, processing and mosaicking approach based on the ECS algorithm (ECS&M);
2. a TDBP processing approach which easily adapts to the changing flight geometry and antenna pointing direction.

The merits and limitations of these two approaches are highlighted by applying them to three airborne SAR data sets acquired from different nonlinear flight tracks. A data set acquired from a quasi-linear track over the same area is used for comparison.

In addition, the focusing performance of the TDBP approach is evaluated quantitatively by examining the impulse response of an in-scene corner reflector. For comparison, a simulated point target having the same position as the corner reflector is evaluated in the same way. During the simulations, the 3-D coordinates and attitude data of the real sensor have been used to ensure comparability between the simulated and the real data.

This paper is organized as follows: Section 2.2 discusses the two focusing approaches that were applied to the SAR data from highly nonlinear flight tracks. In Section 2.3, the SAR experiment, as well as the methods used to evaluate the focusing quality of the algorithms, is described. Section 2.4 provides the results in the form of close-ups of amplitude images, impulse response figures for a simulated point target and a trihedral corner reflector, and coherence maps for two image pairs of a small subregion. A discussion of the results follows in Section 2.5, and finally, conclusions are drawn in Section 2.6.

2.2 Processing of Nonlinear Flight Tracks

2.2.1 Patchwise Frequency-Domain Processing and Mosaicking

Frequency-domain processing algorithms such as the range-Doppler [17, 18], $\omega - k$ [19], or (extended) chirp scaling [1, 20] approaches feature high focus-

ing accuracy while remaining highly efficient. However, they all rely on regular data alignment. Relatively small deviations from a given linear sensor path can be corrected by realigning the data to the linear path by applying motion-compensation algorithms [21]. However, large deviations from a linear track, such as in the case of intentionally nonlinear flight paths, are more difficult to handle.

These limitations may be overcome by approaches where individually focused subpatches of the data set are stepped together (e.g. [22]). To ensure a correct stepping of these single-look complex (SLC) data patches from a strongly nonlinear recording path, additional location corrections for the individual patches need to be made, either by image matching or, as presented here, by geocoding.

The algorithm described here is based on airborne SAR raw data. A first patch of the raw data is extracted, i.e. an azimuth segment of a predetermined length is selected and focused using ECS with motion compensation and linearization of the small patch, as described in [21]. The central part in azimuth of the focused patch—containing information from the full synthetic aperture—is subsequently geocoded onto the underlying terrain [23, 24]. The next patch of the raw data is then defined such as to partially overlap in azimuth with the previous patch. The new patch is processed, focused, and geocoded into the output map geometry. This process is repeated until the entire raw data set has been processed. The mosaicking procedure is shown in Fig. 2.1.

The geocoding step begins with a forward projection into a map geometry, where the corners of the selected patch are geocoded to determine the area of interest. If it is the first patch, an empty geocoded image is created with the dimensions of the area of interest. Otherwise, the previous geocoded image is read and resized to include the new area of interest. An overlap always exists between the newly geocoded patch and the previously mosaicked patch of the mosaic. Overlapping may be as much as 50% of the patch; this is the case for the results presented in Section 2.3. Output samples within overlap zones are produced by weighted averaging of the input samples.

The backward geocoding step, whose aim is to append a patch to the geocoded mosaic, starts from a set of coordinates on the ground and finds the corresponding position within the current SLC patch. This involves selecting a ground position, deriving its terrain height from a digital elevation model (DEM), and calculating a vector between the back-scattering element and the antenna position, using the navigation data and the Doppler centroid frequency from the

ECS focusing step. The sensor position and the length of the range vector provide the azimuth and range coordinates within the SLC; the data are extracted at these coordinates and mapped to the mosaic.

Considering that geocoding a focused SAR image, which is described by slant-range and azimuth coordinates, is not a one-to-one operation, resampling of the SAR data is needed (e.g. cubic B-spline [25, 26]). To obtain a smooth geocoded image, an averaging filter can be applied.

Consequently, certain conditions need to be met in order to obtain a precisely mosaicked and geocoded image from a nonlinear flight track with the method described above. The flight direction must be nearly constant over the length of the synthetic aperture for each patch. If this condition is not met, image blurring will occur. Furthermore, the Doppler centroid frequency may vary by more than half a pulse-repetition frequency (PRF) between two successive patches; this leads to ghost targets or data gaps in the scene, as well as bad focusing of certain parts of the image. In this case, a solution may be to process the image once more with smaller patches and/or smaller steps between the patches. However, the desired azimuth resolution, i.e. the correlation length in azimuth, sets a lower limit on the patch length.

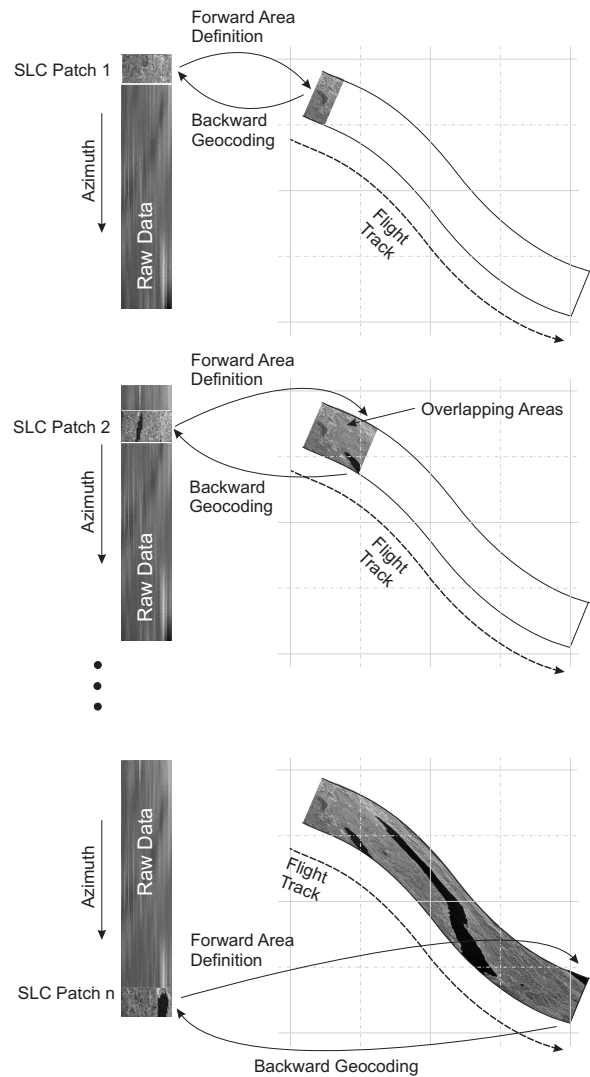


Figure 2.1: Schematic illustration of mosaicking through geocoding of the individually focused subpatches of the data set.

2.2.2 TDBP

Methodology

Our TDBP implementation has been described in [27] and [28]. Implementation details on aspects such as processing steps, parallelization, hardware used and computational cost are given in Section 2.2.2.

In the following, the focus lies mainly on the extension that makes the algorithm suitable for processing SAR data acquired from an arbitrary flight track. The key items of the TDBP approach which enable successful focusing of such SAR data are as follows:

1. By processing the data in the time domain, the exact 3-D configuration of the acquisition pattern and the surface of the illuminated area can be exploited—to the extent that the motion of the aircraft is accurately measured and an accurate digital elevation/surface model is available. In other words, the exact reference function is determined for each point of the reconstruction grid based on the 3-D coordinates of the target points and of the sensor along the synthetic aperture.
2. The Doppler centroid frequency is determined from the sensor’s velocity, position and attitude data and is updated for each radar echo.
3. The varying boundaries of the Doppler bandwidth over azimuth are compared with the Doppler frequency under which the individual target points are “seen.” The signal contributions to a certain point on the reconstruction grid are weighted according to the Doppler frequency or omitted if the Doppler frequency exceeds the Doppler boundaries.
4. The scene is divided into a user-defined number of patches that can be processed in parallel in order to overcome the high computational burden of the TDBP approach.

In the following, it is described how the variation of the antenna look direction caused by the nonlinear flight geometry is accounted for during azimuth focusing. For each radar echo j , the Doppler centroid frequency f_{dc_j} is calculated from the navigational data assuming an Earth-centered rotating (ECR) coordinate system, e.g., the WGS84 coordinate system and zero target velocity

$$f_{dc_j} = \frac{2}{\lambda_c} \cdot \frac{\vec{v}_{S_j} \cdot \vec{p}_j}{|\vec{p}_j|} \quad (2.1)$$

where λ_c is the wavelength of the carrier signal, \vec{v}_{S_j} is the velocity vector of the sensor corresponding to the j th radar echo, and \vec{p}_j is a vector indicating the antenna pointing direction. \vec{p}_j is calculated from the sensor's positioning and attitude data (roll, pitch, and heading) and is updated for each radar echo. Usually, the velocity vector \vec{v}_{S_j} is directly available from navigational data that accompany the SAR raw data. The pointing vector \vec{p}_j varies as the attitude of the sensor platform changes along the nonlinear flight track. \vec{p}_j is obtained from the aircraft-fixed constant antenna pointing vector \vec{p}_B by the following procedure.

First, \vec{p}_B is left-multiplied by the following azimuth-varying rotation matrices in order to obtain the antenna pointing vector \vec{p}_{ned_j} in the topocentric northing-easting-down (NED) coordinate space

$$M_{\theta_{h_j}} = \begin{bmatrix} \cos\theta_{h_j} & -\sin\theta_{h_j} & 0 \\ \sin\theta_{h_j} & \cos\theta_{h_j} & 0 \\ 0 & 0 & 1 \end{bmatrix} \quad (2.2)$$

$$M_{\theta_{p_j}} = \begin{bmatrix} \cos\theta_{p_j} & 0 & \sin\theta_{p_j} \\ 0 & 1 & 0 \\ -\sin\theta_{p_j} & 0 & \cos\theta_{p_j} \end{bmatrix} \quad (2.3)$$

$$M_{\theta_{r_j}} = \begin{bmatrix} 1 & 0 & 0 \\ 0 & \cos\theta_{r_j} & -\sin\theta_{r_j} \\ 0 & \sin\theta_{r_j} & \cos\theta_{r_j} \end{bmatrix} \quad (2.4)$$

$$\vec{p}_{ned_j} = M_{\theta_{h_j}} M_{\theta_{p_j}} M_{\theta_{r_j}} \vec{p}_B. \quad (2.5)$$

θ_{h_j} is the *heading*, θ_{p_j} is the *pitch angle*, and θ_{r_j} is the *roll angle*, which, together, define the coordinate transformation between the aircraft's frame of reference and the topocentric NED frame. Note that the rotation angles vary with azimuth. The coordinates are then transformed from the topocentric NED frame to the ECR coordinate system by left-multiplying the rotation matrix M_{T2G_j} to the antenna pointing vector \vec{p}_{ned_j} in NED coordinates

$$M_{T2G_j} = \begin{bmatrix} -\sin\Phi_j \cdot \cos\Lambda_j & -\sin\Lambda_j & -\cos\Phi_j \cdot \cos\Lambda_j \\ -\sin\Phi_j \cdot \sin\Lambda_j & \cos\Lambda_j & -\cos\Phi_j \cdot \sin\Lambda_j \\ \cos\Phi_j & 0 & -\sin\Phi_j \end{bmatrix} \quad (2.6)$$

Φ_j is the latitude and Λ_j the longitude. The azimuth-varying antenna pointing vector \vec{p}_j , in ECR coordinates, is calculated as

$$\vec{p}_j = M_{T2G_j} \vec{p}_{ned_j}. \quad (2.7)$$

Inserting \vec{p}_j into (2.1) yields the azimuth-varying reference Doppler centroid frequency f_{dc_j} calculated from geometry, which is later used in order to determine the contributions of the individual radar echoes to a particular target position. Aside from the variation along the flight direction, the Doppler centroid also changes as a function of the elevation angle. This effect is accounted for by calculating the Doppler centroid frequency for three different elevation angles at each sensor position. A polynomial is then determined, which best describes the variation.

Using f_{dc_j} , the azimuth-varying upper and lower limits of the Doppler bandwidth to process are given by $f_{d_{max_j}} = f_{dc_j} + B/2$ and $f_{d_{min_j}} = f_{dc_j} - B/2$, where B is the constant absolute Doppler bandwidth.

For each pixel i on the reconstruction grid, the Doppler frequency $f_{d_{ij}}$ is calculated based on the varying geometric constellation given by the target position vector on the ground \vec{r}_i , the sensor position \vec{r}_{S_j} , and the sensor velocity vector \vec{v}_{S_j}

$$f_{d_{ij}} = \frac{2}{\lambda_c} \cdot \frac{\vec{v}_{S_j}(\vec{r}_i - \vec{r}_{S_j})}{|\vec{r}_i - \vec{r}_{S_j}|}. \quad (2.8)$$

During the coherent summation in the time domain, a weighting function $w(df_{d_{ij}})$ is applied, where $df_{d_{ij}} = f_{d_{ij}} - f_{dc_j}$. The weighting term w ensures that only signal contributions corresponding to the actual sensor orientation at each azimuth time step are coherently added

$$w(df_{d_{ij}}) = \begin{cases} \alpha - (1 - \alpha) \cos\left(\frac{2\pi df_{d_{ij}}}{B} - \pi\right), & |df_{d_{ij}}| \leq \frac{B}{2} \\ 0, & |df_{d_{ij}}| > \frac{B}{2}. \end{cases} \quad (2.9)$$

A value $\alpha = 0.54$ was chosen which corresponds to a Hamming weighting function. Of course, any other appropriate weighting function can be applied. If the weighting function $w(df_{d_{ij}})$ is incorporated into the TDBP algorithm, the focused signal $s(\vec{r}_i)$ is given as

$$s(\vec{r}_i) = \sum_{j=a(\vec{r}_i)}^{b(\vec{r}_i)} w(df_{d_{ij}}) \cdot g(|\vec{r}_i - \vec{r}_{S_j}|, \vec{r}_{S_j}) \cdot |\vec{r}_i - \vec{r}_{S_j}| \cdot \exp(j2k_c|\vec{r}_i - \vec{r}_{S_j}|). \quad (2.10)$$

a and b are the indices of the first and last sensor positions, respectively, still contributing to the grid position \vec{r}_i . The range-compressed demodulated two-way response is given by $g(\cdot)$ and k_c is the central wavenumber.

The acquisition geometry consists of the nonlinear flight track and a reconstruction grid based on a DEM. Fig. 2.2 shows the general case of a nonlinear flight track and variable terrain. The synthetic aperture and the related geometric elements are shown for the position \vec{r}_i on the reconstruction grid. Note that a and b vary as a function of the grid position \vec{r}_i .

Finally, a note is due regarding the calculation of the sampling spacing of the reconstruction grid. Within the TDBP algorithm, the range-compressed data are not focused in the native slant-range/azimuth geometry, but are “back-projected” to another grid, usually termed the *reconstruction grid* or image space. In order to avoid aliasing, an appropriate sampling spacing has to be chosen for the reconstruction grid, taking into account the original range and azimuth sampling rates, as well as the shape of the flight track. In particular, attention must be paid to strongly curved tracks, where the direction of illumination varies dramatically during the data acquisition. In such cases the orientation of ground range and azimuth, with respect to the orientation of the reconstruction grid, is continuously changing as the sensor moves along the nonlinear trajectory. Therefore, the output sampling spacing must satisfy the requirements imposed by the varying orientation of ground range and azimuth, such that the focused complex SAR image is never undersampled in either dimension.

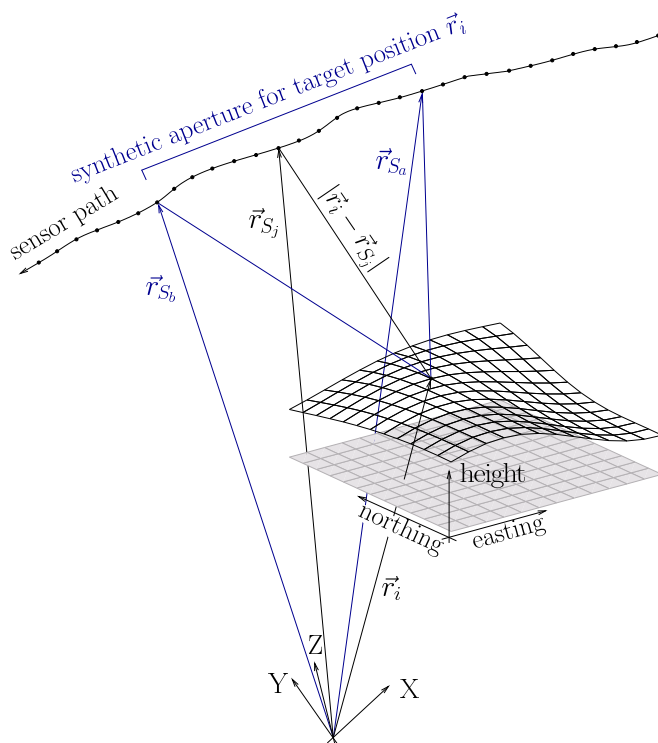


Figure 2.2: Schematic view of the acquisition/reconstruction geometry for TDBP processing of SAR data from nonlinear flight tracks.

Implementational Aspects

Our experimental TDBP processor has been realized within a combined Matlab and C++ environment. Tasks such as the preparation of auxiliary data, including navigation data, DEMs, and the subdivision of the data into a number of subpatches to be processed in parallel, are all handled within Matlab.

The processor is connected to a coordinate transform engine. Thus, reconstruction grids can be defined for any desired map projection. For the experimental data, each scene has been subdivided into patches of 0.5 km x 1 km in size in the local map projection. The computationally expensive back-projection processing is then performed by an efficient ANSI C++ implementation of the TDBP algorithm. The subsequent collection and mosaicking of the individual patches, as well as data visualization and analysis operations, are again handled by dedicated Matlab scripts. The main processing steps can be summarized as follows.

Processing steps The processing steps are as follows.

1. Range compression.
2. Preparation of the navigation data.
3. Preparation of the reconstruction grid (may include a DEM) subdivided into a user-defined number of patches in a coordinate system of choice.
4. For each patch, the first and the last contributing echo is determined.
5. The TDBP jobs are sent to the different computing platforms.
 - a) Each range-compressed echo is upsampled using a fast Fourier transform (FFT)-based upsampling method [29].
 - b) For a sensor position \vec{r}_{S_j} the sensor-to-pixel ranges are calculated for all samples of a patch. Additionally, the Doppler frequency $f_{d_{ij}}$ is evaluated based on (2.8).
 - c) The data values are extracted from the upsampled range echo at the appropriate range distances (rounded to the upsampled sampling spacing), modulated and weighted as described in (2.10).
 - d) The contributions from each echo to a pixel are coherently added until the complete synthetic aperture is reached.
 - e) Demodulation.
6. The data patches are assembled and mosaicked.

Parallelization The subdivision of the scene into several patches, which are then processed individually, permits parallelization of the implementation of the TDBP algorithm. Thus, numerous patches can be processed simultaneously. In fact, a rather heterogeneous computer cluster (see also the next section)

was used for TDBP processing of the experimental data. All machines are accessible via a network and are connected to a centralized array of hard disks for efficient data I/O. This way, interprocess communication is reduced to a minimum. Parallelization of the problem in this way seems to be a flexible and natural solution, particularly because of its *hardware independence*. This type of parallelization is also termed “embarrassing” or “trivial” parallelization, since the parallelization is done at a high level of the algorithm rather than at lower level functions, e.g., the FFT.

Hardware The experimental data presented in the following section had been focused using a loose network of different computing platforms available at our institute. Among these are a Sun Fire V40z Server, which is equipped with four dual-core AMD Opteron processors Model 880 (2.4 GHz) and 16-GB RAM running a Linux operating system; several single- and dual-core processor Linux PCs (3.2-GHz clocked Intel Pentium 4) with 1–2-GB RAM; and Mac Pro platforms equipped with two 2.8-GHz Quad-Core Intel Xeon processors and 4-GB RAM. Note that the TDBP processing framework developed here is not hardware specific.

Computational cost Processing a patch consisting of 10^6 pixels with its center at midrange takes about 10 min on a CPU of a Mac Pro and about 20 min on the Sun Fire or the Linux PCs. Thus, choosing a conservative grid spacing of 0.25 m x 1 m, a scene of 3 km x 4 km can be processed within approximately 1 h using the 8 CPUs of a single Mac Pro.

2.3 Description of the Experiment

2.3.1 Experimental Setup

In order to assess the two proposed processing approaches, four tracks were flown by the German Aerospace Center (DLR)’s E-SAR system, namely, a quasi-linear reference track, a track involving a drop in altitude of approx. 250 m (*dive*), a double-bend track, and a track with a 90° curve, all shown in Fig. 2.3.

The system parameters of the L-band sensor used are listed in Table 2.1. The E-SAR system is equipped with a modern computer-controlled CCNS4 nav-

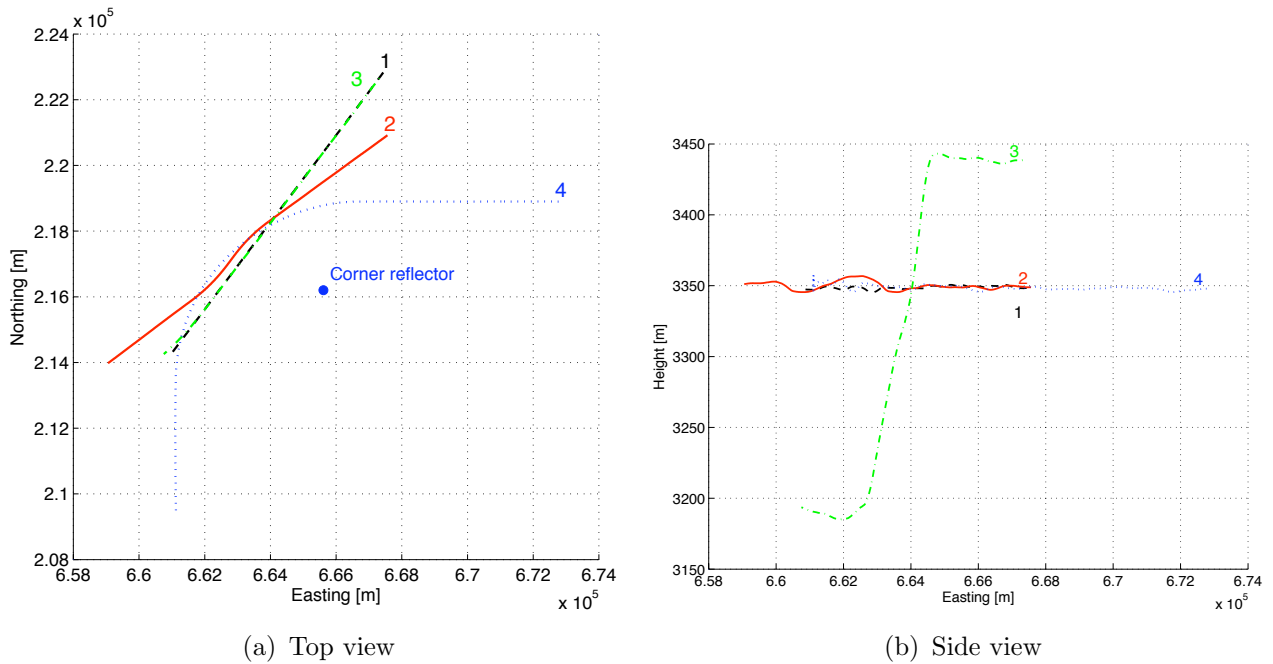


Figure 2.3: Nonlinear flight tracks flown during the experiment, as obtained from the DGPS/IMU system of the E-SAR system: (1, $- -$) Quasi-linear reference track. (2, $-$) Double bend. (3, $- -$) Dive. (4, $\cdot \cdot$) 90° curve. The position of a corner reflector is shown in (a).

Table 2.1: E-SAR L-Band System Specifications.

Carrier frequency	1.3 GHz
Chirp bandwidth	94 MHz
Sampling rate	100 MHz
PRF	400 Hz
Ground speed	90 m/s
Azimuth beam width	18°
Elevation beam width	35°
Look direction	left

igation system combined with a highly precise differential global positioning system/inertial measurement unit (DGPS/IMU) system of the type AEROcontrol IId, both by IGI mbH. The absolute 3-D positioning accuracy lies between 0.05 m and 0.1 m rms for the available experimental data sets. The short-term relative positioning accuracy is about 0.01 m rms. The accuracy of the attitude angles are given [30] as $\sigma_{\theta_r} = \sigma_{\theta_p} = 0.004^\circ$ rms for the roll and pitch angles and $\sigma_{\theta_h} = 0.01^\circ$ rms for the heading. The velocity is measured with an accuracy of $\sigma_V = 0.005$ m/s, and the bias of the accelerometer $\sigma_b \approx 5 \times 10^{-3}$ m/s². Ac-

According to Fornaro *et al.* [31], the first derivative of the residual range error, the drift $\sigma_{\dot{\delta}_e}$, and the second derivative thereof $\sigma_{\ddot{\delta}_e}$ can be expressed as follows:

$$\sigma_{\dot{\delta}_e}^2 = \frac{1}{V^2} \sigma_V^2 + (\sin^2 \vartheta) \sigma_{\theta_h}^2 \quad (2.11)$$

$$\sigma_{\ddot{\delta}_e}^2 = \frac{1}{V^4} \sigma_b^2 + \left(\frac{g \sin \vartheta}{V^2} \right)^2 \sigma_{\theta_r}^2 \quad (2.12)$$

where V is the platform velocity, $g = 9.81 \text{ m/s}^2$ is the acceleration due to gravity, and ϑ is the elevation angle, which will be fixed to 45° . The following values are subsequently obtained for $\sigma_{\dot{\delta}_e}$ and $\sigma_{\ddot{\delta}_e}$:

$$\sigma_{\dot{\delta}_e} = 1.35 \times 10^{-4} \quad (2.13)$$

$$\sigma_{\ddot{\delta}_e} = 6.2 \times 10^{-7} \text{ m}^{-1}. \quad (2.14)$$

In addition to the focusing quality, the geometric fidelity of the final image is an important aspect for the user. In order to assess the preservation of dedicated features in the focused image, an airfield has been chosen as a test site. The airfield contains numerous linear elements, such as a runway, fences, and large buildings.

In Fig. 2.4, the variation of the Doppler centroid values along the flight track is shown for the four different flight paths. The Doppler centroid values are calculated from sensor motion and attitude data, and represent the Doppler centroid values corresponding to the pointing direction of the antenna.

For a quantitative analysis of the impulse response, a trihedral corner reflector, which is visible in all four data sets, was installed on the airfield.

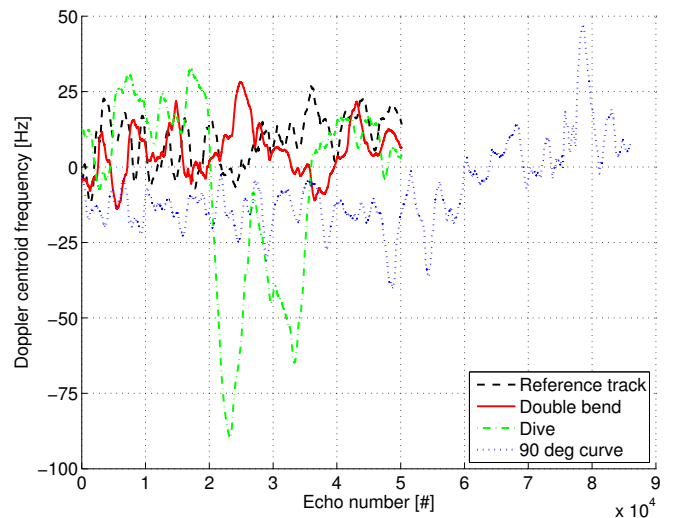


Figure 2.4: Variation of the midelevation Doppler centroid values along the flight track for the four different flight paths, calculated from navigation data.

2.3.2 Quality Measures for Focused Data

In order to quantify the focusing performance obtained with TDBP processing, the characteristics of the impulse response using the corner reflector, as well as a simulated point target, were measured.

The reader is referred to [32] and [33] for a definition of the numerous quality measures such as the following:

1. three-decibel spatial resolution;
2. peak-to-sidelobe ratio (PSLR);
3. spurious sidelobe ratio (SSLR);
4. integrated sidelobe ratio (ISLR);
5. ratio of total power to peak height (TPPR).

2.4 Results

First of all, some general remarks are needed concerning the evaluation of the results. Qualitative visual comparisons are made of close-up extracts from the airfield area. The processing quality is quantitatively assessed using the measures listed in the previous section. Only the results processed by the TDBP approach are evaluated in detail and compared with the reference track. Detailed analysis of the ECS&M-processed data is not useful here because the SAR images resulting from the frequency-domain/mosaicking approach are not well focused, as shown in Figs. 2.5 and 2.6. Two-dimensional frequency plots are presented for all flight tracks processed by TDBP. In addition, coherence maps are given in order to provide area-based measures of processing quality, as opposed to point-target-based measures. Naturally, a useful degree of coherence can only be achieved in cases where the critical baseline criterion is not violated. Further, the look direction in azimuth—or, in other words, the portion of the processed Doppler spectrum—must be identical. At minimum, a considerable overlap is needed. Bearing in mind the flight tracks, which are shown in Fig. 2.3, it is furthermore clear that the coherence can only be assessed for selected portions and combinations of the four data takes. In the present case, only two combinations of valid data pairs permit the evaluation of the coherence magnitude between the four different flight tracks. Note that the intention of the experiment—and, therefore, the choice of the flight tracks—was

not governed by interferometric requirements. Rather, the goal was to make the focusing task as difficult as possible by introducing complicated sensor motions and directional changes during the data acquisition. Nevertheless, the authors believe that the coherence maps provide a useful complementary measure of the focusing performance of the TDBP processor and demonstrate the phase preservation that can be achieved.

The coherence was estimated as follows, as described, for instance, in [34]:

$$\hat{\gamma} = \frac{\left| \sum_{n=1}^N \sum_{m=1}^M s_1(n, m) \cdot s_2^*(n, m) \cdot e^{-j\hat{\phi}(n, m)} \right|}{\sqrt{\sum_{n=1}^N \sum_{m=1}^M |s_1(n, m)|^2 \cdot \sum_{n=1}^N \sum_{m=1}^M |s_2(n, m)|^2}} \quad (2.15)$$

where the interferometric phase $\hat{\phi}(n, m)$ is estimated beforehand using identical spatial averages. s_1 and s_2 represent the two SAR images. To calculate the spatial averages, $N=M=5$ is chosen.

2.4.1 Image Comparison

In this section, the quality of the images is discussed by comparing close-ups of the same scene extract for all four sensor trajectories and both ECS&M and TDBP algorithms.

Quasi-Linear Track The reference data set acquired from a standard near-linear sensor trajectory is well focused using both processing techniques [see Fig. 2.5(a) and (b)].

Double Bend In Fig. 2.5(c), the double-bend data set processed by ECS&M is shown. Considerable defocusing is identified in the southwestern portion of the image. This area is heavily affected by one of the curves of the double-bend track. For this portion of the flight track, the deviation from the linear subpatches is too large. This, in turn, results from the fact that the number of subpatches is limited by the size of the azimuth beam width. Therefore, a defocused image is obtained. On the other hand, TDBP delivers a well-focused image [see Fig. 2.5(d)]. Note the slightly positive gradient in brightness from the northeastern corner to the southwestern corner of the image, best visible along the runway. This effect is due to the azimuth-varying position of the beam

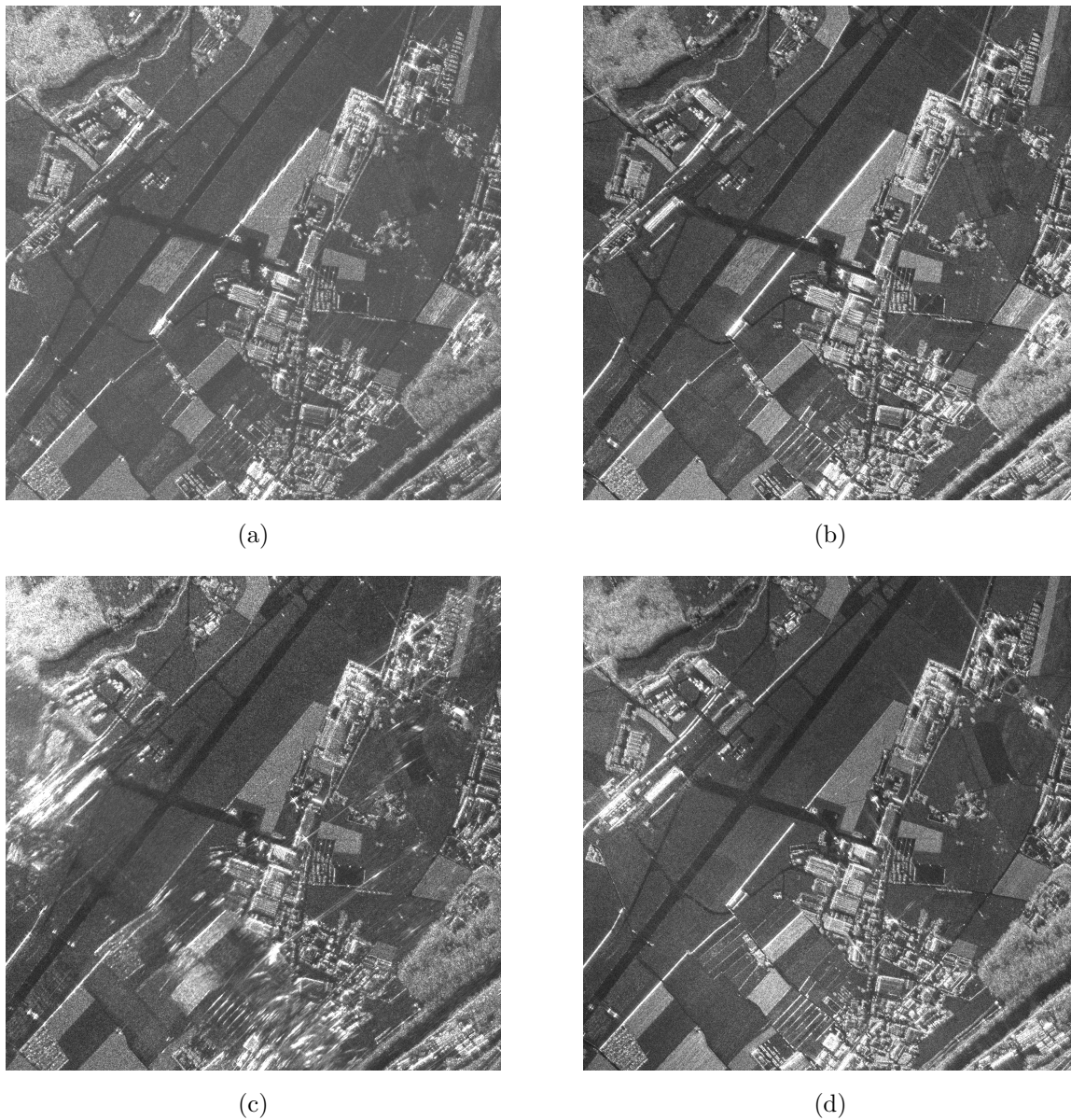


Figure 2.5: Close-up views of amplitude images. Sensor: E-SAR L-band HH. (a) ECS and mosaicking: (Quasi-)linear reference track. (b) TDBP: (Quasi-)linear reference track. (c) ECS and mosaicking: Double bend. (d) TDBP: Double bend.

center location in the geocoded image, caused by the steeper antenna look angle during the left turn and due to the fact that the elevation antenna gain pattern has intentionally been left uncorrected.

Dive The image resulting from ECS&M [see Fig. 2.6(a)] appears to be well focused in terms of the geometric resolution; however, a low signal-to-noise ratio

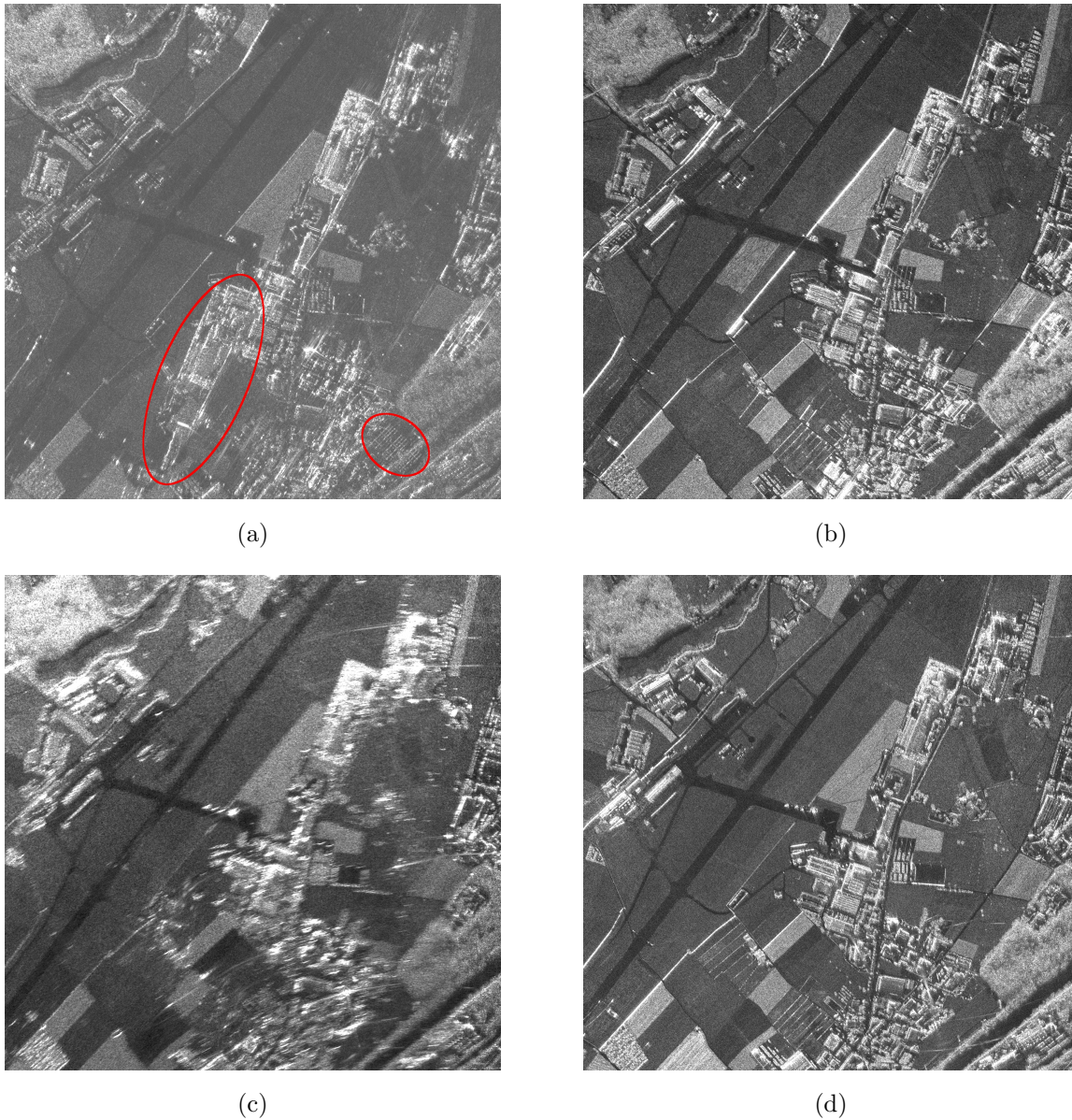


Figure 2.6: Close-up views of amplitude images. Sensor: E-SAR L-band HH. (a) ECS and mosaicking: Dive. (b) TDBP: Dive. (c) ECS and mosaicking: 90° curve. (d) TDBP: 90° curve.

is observed. In particular, the image exhibits severe ghost targets [shown by the ellipses in Fig. 2.6(a)] as a result of the abrupt change in the antenna pointing direction [see also Fig. 2.4, where a noticeable change in pointing direction is indicated by the change in Doppler centroid frequency]. Again, this rapid change cannot be accounted for within the ECS algorithm and, therefore, the spectral components are mapped incorrectly in the final image. In contrast, the image resulting from TDBP [see Fig. 2.6(b)] is free of Doppler aliasing and is

well focused.

90° Curve The whole image patch shown in Fig. 2.6(c), which is approximately situated in the center of the curve, appears blurred. The defocusing is due to the strong curvature of the 90° flight track in combination with the long synthetic aperture of the E-SAR L-Band system; for each subpatch, the deviation of the linearized path from the real sensor trajectory becomes too large towards the ends to still permit an adequate motion compensation within the ECS&M algorithm. In contrast, the TDBP algorithm handles the curved flight geometry very well, and a high focusing quality is obtained [see Fig. 2.6(d)]. The geometric fidelity appears to be high in all cases, as can be seen by the preservation of linear features, such as the runway and fences.

2.4.2 Analysis of the Impulse Response

An analysis of the impulse response function (IRF) was performed for a simulated point target, as well as for a corner reflector visible in the real SAR data set. The simulated point target was assigned the 3-D coordinates of the in-scene corner reflector, which had been deployed on the airfield before the SAR acquisitions. The raw data for the simulated point target was generated using the navigational data of the real flight tracks, providing the identical acquisition geometries required for their comparison.

All impulse response analyses presented here are based on data focused by the proposed TDBP approach. The authors refrain from including the impulse response analyses for the ECS&M approach, since the defocusing and image degradations are immediately clear by visual inspection of Figs. 2.5 and 2.6, making further quantitative analysis unnecessary.

Simulated Data

The reason simulated data sets are used to analyze the focusing performance is to demonstrate the focusing quality for a *point target* under ideal conditions.

In Fig. 2.7, the IRFs for all four simulated data sets are shown, after they have been focused by the TDBP algorithm. The figure annotations list the relevant quality parameters. During range compression, a Kaiser window with coefficient $\beta = 2.12$ was applied, giving a nominal PSLR of ca. -19 dB. This value is

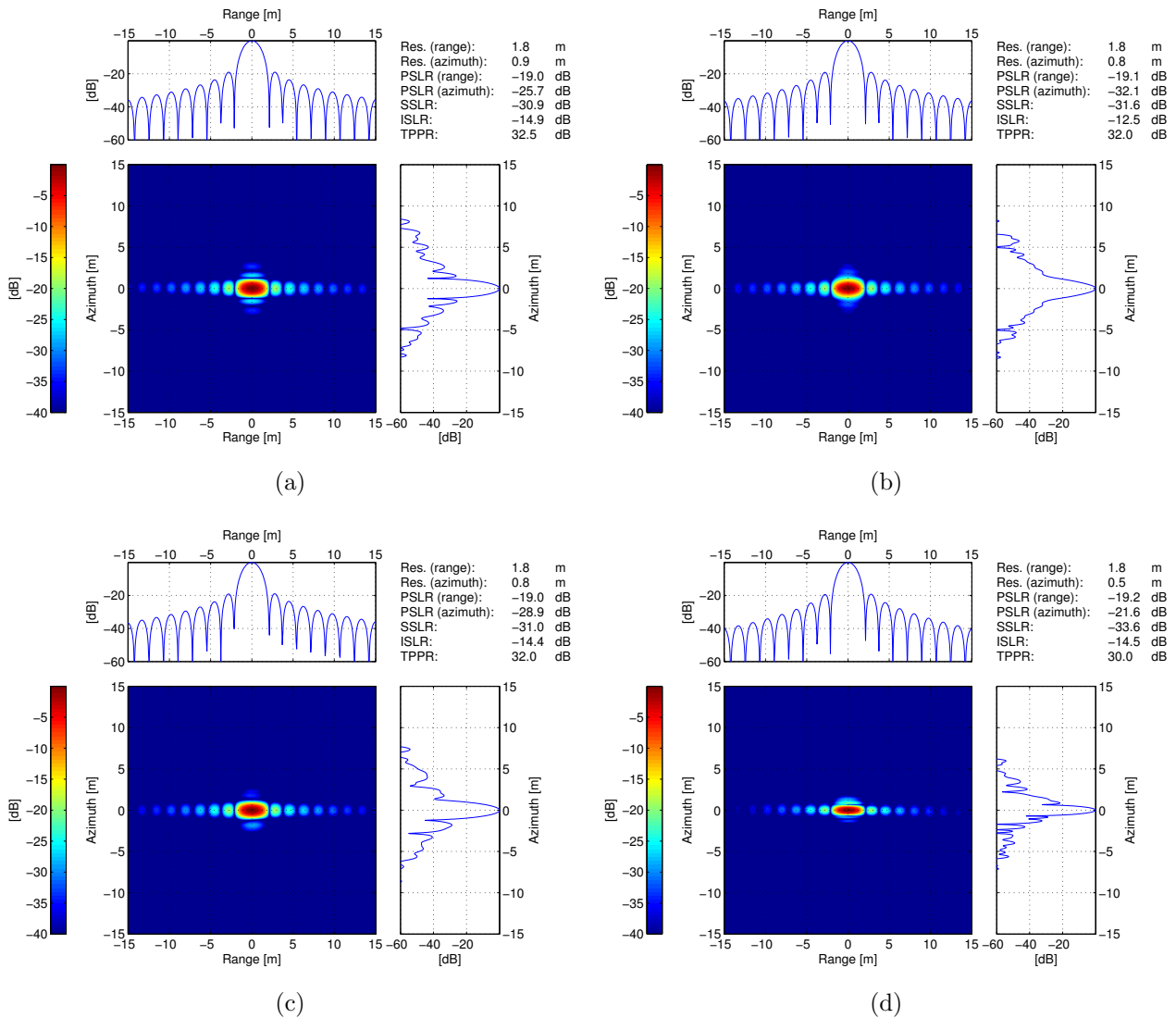


Figure 2.7: Impulse response and quality figures of a simulated point target for all four flight tracks. The location of the simulated point target matches the true location of the trihedral corner reflector that was deployed during the experiment. (a) (Quasi-)linear reference track. (b) Double bend. (c) Dive. (d) 90° curve.

approximately equal to the value obtained for the simulated data sets. In the case of the 90° curve, the area surrounding the corner reflector is illuminated in a sliding spotlight manner, and therefore, the azimuth resolution is increased considerably from 0.9 to 0.5 m. Note that the length of the synthetic aperture is altered along the curved flight track: At the beginning and end of the trajectory, where it is approximately linear, the data take resembles strip-map acquisition. Within the curved portion, it approximates a sliding spotlight acquisition [see also Fig. 2.3 for the shape of the trajectory].

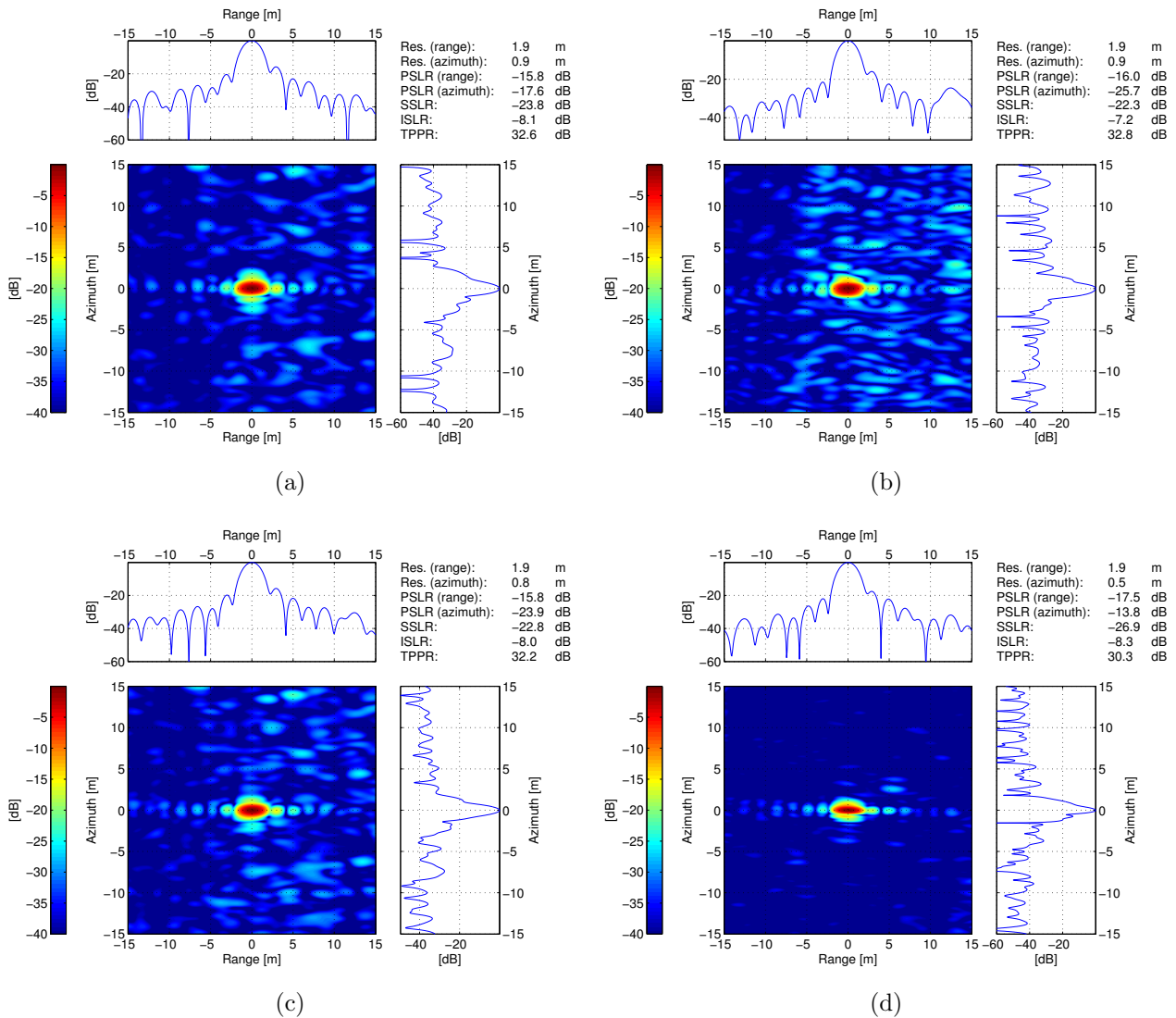


Figure 2.8: Impulse response and quality figures of a trihedral corner reflector for all four flight tracks. For the position of the corner reflector see Fig. 2.3. (a) (Quasi-)linear reference track. (b) Double bend. (c) Dive. (d) 90° curve.

Real Data

Having demonstrated the performance under ideal conditions, the real-world case is now evaluated. The nominal system and processing parameters are identical in both the simulated and real cases. Shown in Fig. 2.8 is the IRF of the TDBP imaging system, evaluated using the in-scene trihedral corner reflector visible in all four SAR images. Compared with the simulated impulse responses, it can be seen that the quality indicators obtained for the corner reflector are inferior for the real data. This is particularly true for the PSLR

in range and azimuth, as well as the ISLR. A trihedral corner reflector with triangular reflecting surfaces was used as the reference target. The length of the cathetus of each triangular surface is $a = 1.2$ m, which results in a radar cross section of $\text{RCS} = 4/3 \cdot \pi \cdot a^4 / \lambda^2 = 163.42 \text{ m}^2$ or $\text{RCS}_{\text{dB}} = 22.13 \text{ dB} \cdot \text{m}^2$ for the given central wavelength $\lambda = 0.2305$ m of the L-band E-SAR system. The range resolution of the impulse responses for the real data is approximately 5 % lower compared with the simulated case since the effective chirp bandwidth is smaller than the bandwidth used during the simulations. The theoretical value of -19 dB for the range PSLR of the point target is not reached with the real data. The first sidelobe in the far range of the point target is by 1.5–3 dB higher than the theoretical value. Also, the azimuth PSLR is affected by anomalous sidelobes, which may have been caused by residual motion errors and interpolation artifacts when preparing the IRF analysis.

In contrast with the simulated case, there are many bright targets visible near the corner reflector. These targets have similar or even higher intensity values than the corner reflector. The tarmac on which the reflector was located also exhibits surprisingly high backscatter, affecting the target-to-clutter ratio for the corner reflector. This causes a reduced ISLR compared with the simulated point target. In terms of azimuth resolution, the impulse responses are equally well focused for both the simulated and real SAR data sets (the resolution has been measured with an accuracy of 10 cm, which corresponds to the sampling spacing of the upsampled impulse response).

However, the most important discovery is that the quality indicators remain *consistent irrespective of the acquisition geometry* for each particular data set, simulated or real. An exception is the azimuth PSLR of the 90° -curved flight, which is considerably lower than in the case of the double-bend or the dive data set. The reason for this difference is the fact that the first azimuth sidelobe is hidden in the main lobe in these cases [see Fig. 2.8]. Apart from that exception, it can be stated that even for the 90° curve flight, the focusing quality is as high as for the quasi-linear reference data set. This demonstrates the ability of the TDBP approach to perform high-quality focusing of all four test cases.

In Fig. 2.9, the 2-D power spectra for the four test cases are shown. There are significant differences, most noticeable in the case of the 90° curve flight and the double-bend track, where an extended Doppler spectrum caused by the curved acquisition geometry can be observed. The spectra were extracted from a part of the scene which includes the corner reflector.

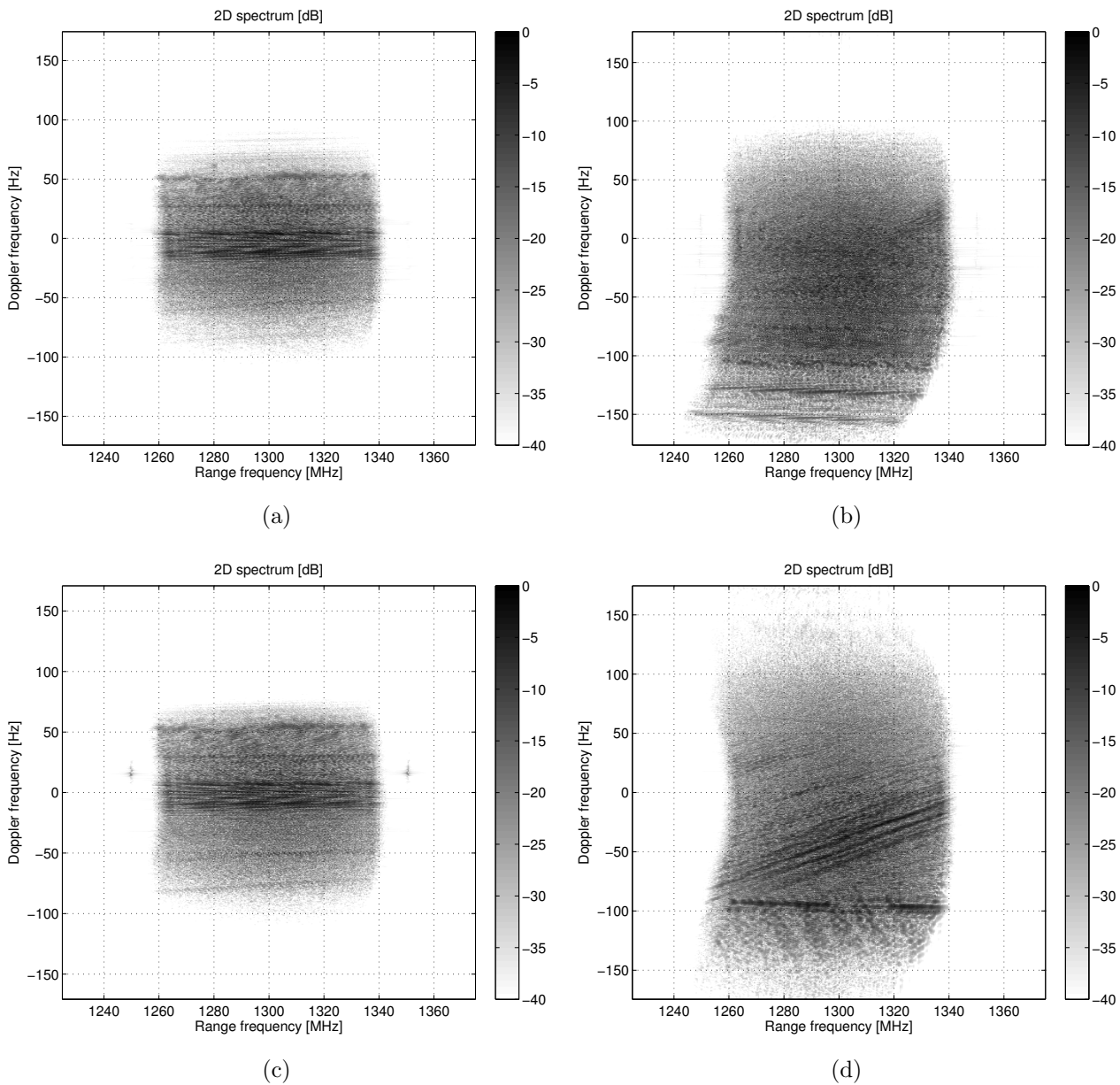


Figure 2.9: Two-dimensional power spectra for all four test data sets corresponding to the surrounding area of the in-scene corner reflector. (a) (Quasi-)linear reference track. (b) Double bend. (c) Dive. (d) 90° curve.

2.4.3 Coherence Maps

The corresponding coherence maps for the data pairs *reference track/dive* and *double bend/90° curve* are shown in Fig. 2.10(a) and (b), respectively. In the case of the *reference track/dive* pair, high coherence values are obtained over a larger area due to the fact that the two flight tracks are more nearly parallel

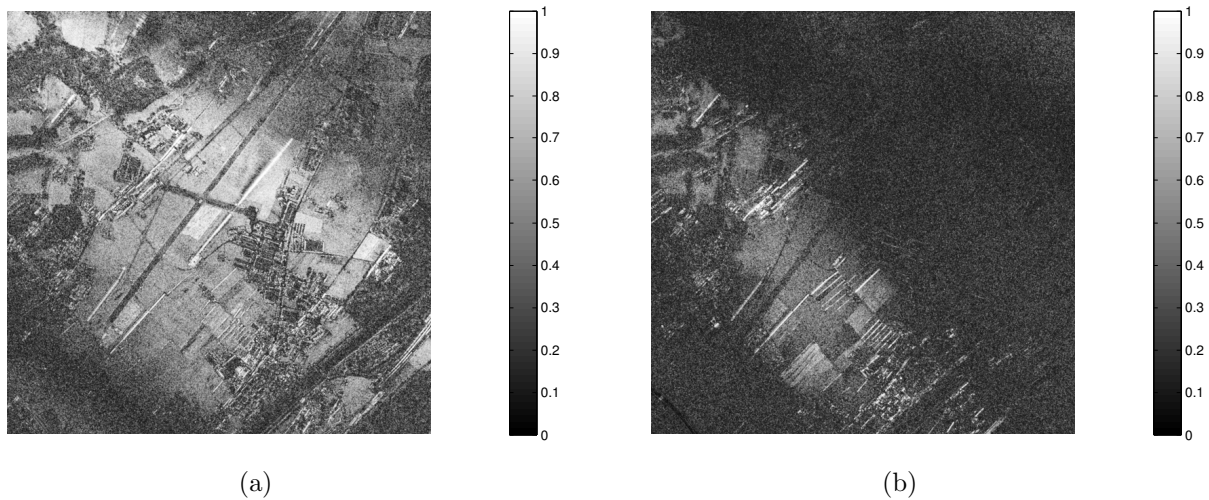


Figure 2.10: Coherence maps for the pairs (a) dive/reference track and (b) double bend/ 90° curve processed by TDBP. See Fig. 2.3 for the corresponding sensor trajectories. High coherence values are obtained for the small regions where the flight tracks are well within the critical baseline and where the look direction is similar (note that the coherence is not optimized in the sense that the Doppler and range spectra are reduced to their common spectral band and that the flight tracks of the two data pairs do not run in parallel).

than in the case of the *double bend/ 90° curve* pair.

Note that the coherence has not been optimized. The Doppler and range spectra have not been reduced to their common spectral band. This is because the coherence is only used as an indicator of phase preservation and focusing quality. Spectral filtering would alter the resolution properties, causing certain regions not to be imaged at all due to the high variability of the relevant Doppler spectrum over azimuth. Neither of these effects is desired; thus, the coherence map is used solely as an indicator of the processing quality.

Indeed, in those areas where the critical baseline criterion is not violated and the look angles coincide, high coherence is obtained. This indicates that the phase is well preserved here, even for the highly nonlinear flight tracks.

2.4.4 Complete 90° Curve Flight

In Fig. 2.11 the amplitude image obtained from TDBP processing of the 90° curve flight is shown, placed on top of a 1:25000-scale map of the area. The data acquisition began in the northeast part of the image, with a heading of 270° and the antenna aimed southward (left-looking antenna). After the aircraft had

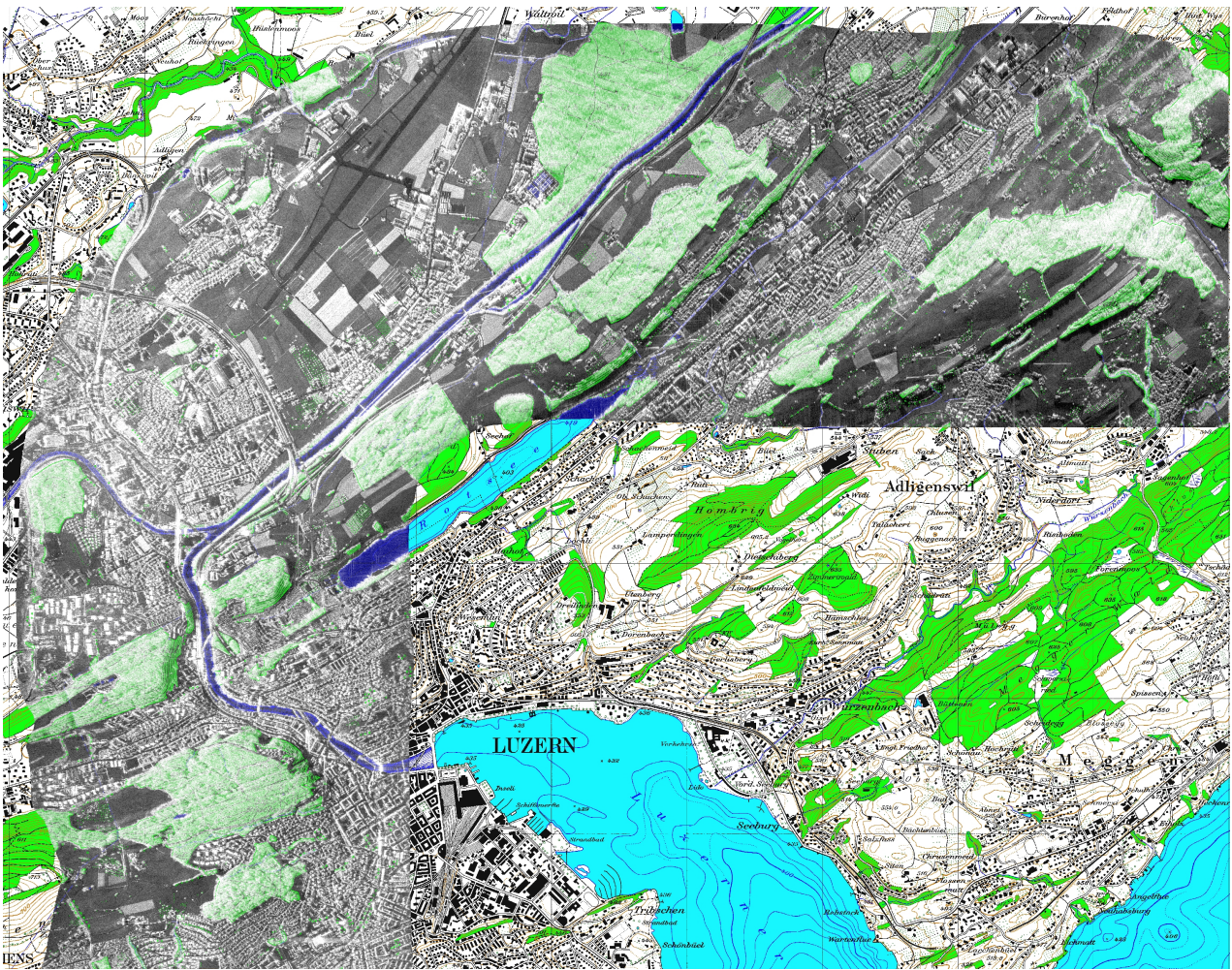


Figure 2.11: Amplitude image of the 90° curve track: E-SAR L-band HH. Processing: TDBP. The data set has been processed directly to map coordinates using a DEM. The SAR amplitude image is shown on top of a 1:25000-scale digital map of the area. Map reproduced by permission of swisstopo (BA081196).

flown about 5 km to the west, it performed a 90° left turn, resulting in a heading of 180° and an eastward look direction. The data set has been processed onto a DEM given in Swiss map coordinates. The ability of the TDBP approach to process highly nonlinear flight geometries is strikingly demonstrated by the example of this 90° -curved SAR data strip.

2.5 Discussion

Airborne SAR data acquired from highly nonlinear flight tracks was focused using two processing approaches: 1) a patchwise focusing and mosaicking approach based on the ECS algorithm, and 2) a flexible TDBP approach, which utilizes the true 3-D acquisition geometry.

In our experiment, the E-SAR L-band sensor had a moderate azimuth beam width of only 18° . Nonetheless, the focusing quality of the ECS&M was unsatisfactory, whereas the TDBP approach proposed in this paper provided well-focused results, irrespective of the flight geometry. Its ability to handle difficult 3-D geometry through its inherent consideration of the varying antenna pointing direction during azimuth focusing makes it the superior method. The high focusing performance of the algorithm was demonstrated by point-target analyses and a coherence evaluation of the processed data.

The focusing quality achieved using the ECS&M approach is degraded severely for segments where highly nonlinear sensor motion was present. The major causes are high horizontal (double-bend and 90° curve cases) or vertical (dive case) deviations of the linearized subpaths from the original nonlinear flight tracks and, particularly, the considerable variation of the flight direction over the length of the synthetic aperture.

The double bend and the 90° curve exhibited maximal deviations of $dn_{\max} = 10.6$ m and $dn_{\max} = 10.7$ m, respectively. For the dive track, the maximal deviation was $dn_{\max} = 9.3$ m, within the length of the synthetic aperture. The quasi-linear reference track, which was well focused by the ECS&M algorithm, had a maximum deviation of $dn_{\max} = 1.8$ m. The maximum angle δ_{\max} between the velocity vector of the linearized sensor path and the true velocity vectors is $\delta_{\max} = 4.9^\circ$ for the double bend, $\delta_{\max} = 4.2^\circ$ for the dive, and $\delta_{\max} = 5.0^\circ$ for the 90° curve. The reference track had a maximum deviation angle of $\delta_{\max} = 0.9^\circ$. Thus, in the case of the double bend and the 90° curve, the total variation of orientation of the airplane within the length of the synthetic aperture was as high as 8° – 10° . The azimuth antenna beam width limits the number of linearized subpaths along the flight track. However, longer linearized subpath lengths cause larger deviations from the real sensor trajectory, and, thus, larger changes in the sensor orientation.

Hence, patchwise frequency-domain processing and mosaicking is limited because of two opposing requirements on the azimuth length of a patch: 1) A

higher flight-track nonlinearity would require patches with shorter azimuth length, and 2) the minimal length of a patch is determined by the azimuth beam width of the antenna. A large azimuth beam width is often preferable in order to ensure a continuous coverage of the region of interest even for large attitude variations along the sensor trajectory.

In an experiment designed to push SAR processing to its limits, it was demonstrated that the proposed TDBP algorithm is a viable and robust processing method when a highly nonlinear sensor trajectory, in combination with a large synthetic aperture, would otherwise cause strong defocusing.

Aside from the higher susceptibility to nonlinear sensor motion, another limitation of the ECS&M approach is that the phase information is not retained in the final mosaicked image. The phase information is preserved when using the TDBP approach, even if the data are directly obtained in the map projection of choice.

A further advantage of the TDBP approach is that it allows any subregion of interest to be processed without the need to process the entire data set.

2.6 Conclusion

The TDBP algorithm proposed in this paper is well adapted for producing high-quality images for airborne SAR data from highly nonlinear flight tracks. The high processing quality and geometric fidelity of this method are demonstrated by comparing the results for a region common with all four data sets. A high focusing quality is achieved regardless of the acquisition geometry. The back-projection algorithm generates complex-valued georeferenced SAR images.

In Section 2.1, corridor mapping was mentioned as a potential application, i.e., mapping of curvilinear features such as rivers or traffic routes. The TDBP-based approach provides the means for such mapping tasks—flexible and parallelized processing of dedicated subareas of interest within a SAR data set acquired from virtually arbitrarily shaped flight tracks, combined with direct mapping functionality in any desired coordinate frame and map projection.

Acknowledgment

The authors would like to thank R. Horn, R. Scheiber, and M. Keller at the German Aerospace Center (DLR) for their cooperation and technical support and the anonymous reviewers for their valuable comments that improved this paper. This work was supported by the Procurement and Technology Center (armasuisse) of the Swiss Federal Department of Defense.

References

- [1] A. Moreira, J. Mittermayer, and R. Scheiber, "Extended chirp scaling algorithm for air- and spaceborne SAR data processing in stripmap and ScanSAR imaging modes," *IEEE Trans. Geosci. Remote Sens.*, vol. 34, no. 5, pp. 1123–1136, Sep. 1996.
- [2] M. Soumekh, "Reconnaissance with slant plane circular SAR imaging," *IEEE Trans. Image Process.*, vol. 5, no. 8, pp. 1252–1265, 1996.
- [3] K. Knaell, "Three-dimensional SAR from curvilinear apertures," in *Proc. SPIE*, vol. 2230, Orlando, FL, Jun. 1994, pp. 120–134.
- [4] J. Li, Z. Bi, Z. Liu, and K. Knaell, "Use of curvilinear SAR for three-dimensional target feature extraction," *Proc. Inst. Elect. Eng.—Radar, Sonar Navig.*, vol. 144, no. 5, pp. 275–283, Oct. 1997.
- [5] C. J. Nolan and M. Cheney, "Synthetic aperture inversion for arbitrary flight paths and nonflat topography," *IEEE Trans. Image Process.*, vol. 12, no. 9, pp. 1035–1043, Sep. 2003.
- [6] S. R. Axelsson, "Beam characteristics of three-dimensional SAR in curved or random paths," *IEEE Trans. Geosci. Remote Sens.*, vol. 42, no. 10, pp. 2324–2334, Oct. 2004.
- [7] L. Xiang and Y. Ruliang, "Study of composite mode curvilinear SAR," in *Proc. Int. Conf. Radar, CIE*, 2006, pp. 1–4.
- [8] Z. Su, Y. Peng, and X. Wang, "Evaluation of the aperture in the curvilinear SAR," in *Proc. Int. Conf. Radar, CIE*, 2006, pp. 1–4.
- [9] Z. Su, Y. Peng, and X. Wang, "Feature-independent aperture evaluator for the curvilinear SAR," *IEEE Geosci. Remote Sens. Lett.*, vol. 4, no. 2, pp. 191–195, Apr. 2007.

- [10] G. Vigurs, M. Wood, and M. Jarrett, “Non-linear synthetic aperture radar techniques,” in *Proc. EURAD*, Oct. 2005, pp. 13–16.
- [11] M. Soumekh, “Time domain non-linear SAR processing,” Dept. Elect. Eng., State Univ. New York, Buffalo, Tech. Rep., 2006.
- [12] M. Soumekh, *Synthetic Aperture Radar Signal Processing: With MATLAB Algorithms*. Hoboken, NJ: Wiley, 1999.
- [13] B. C. Barber, “Theory of digital imaging from orbital synthetic-aperture radar,” *Int. J. Remote Sens.*, vol. 6, no. 7, pp. 1009–1057, 1985.
- [14] J. C. Curlander and R. N. McDonough, *Synthetic Aperture Radar—Systems and Signal Processing*. Hoboken, NJ: Wiley, 1991.
- [15] L. M. H. Ulander, H. Hellsten, and G. Stenström, “Synthetic-aperture radar processing using fast factorized back-projection,” *IEEE Trans. Aerosp. Electron. Syst.*, vol. 39, no. 3, pp. 760–776, Jul. 2003.
- [16] A. F. Yegulalp, “Fast backprojection algorithm for synthetic aperture radar,” in *Proc. Rec. IEEE Radar Conf.*, 1999, pp. 60–65.
- [17] I. G. Cumming and J. R. Bennett, “Digital processing of SEASAT SAR data,” in *Proc. Rec. IEEE Int. Conf. Acoust., Speech Signal*, Washington, DC, Apr. 1979, pp. 710–718.
- [18] M. Y. Jin and C. Wu, “A SAR correlation algorithm which accomodates large range migration,” *IEEE Trans. Geosci. Remote Sens.*, vol. 22, no. 6, pp. 592–597, Jun. 1984.
- [19] C. Cafforio, C. Prati, and F. Rocca, “SAR data focusing using seismic migration techniques,” *IEEE Trans. Aerosp. Electron. Syst.*, vol. 27, no. 2, pp. 194–207, Mar. 1991.
- [20] R. K. Raney, H. Runge, R. Bamler, I. G. Cumming, and F. H. Wong, “Precision SAR processing using chirp scaling,” *IEEE Trans. Geosci. Remote Sens.*, vol. 32, no. 4, pp. 786–799, Jul. 1994.
- [21] A. Moreira and Y. Huang, “Airborne SAR processing of highly squinted data using a chirp scaling approach with integrated motion compensation,” *IEEE Trans. Geosci. Remote Sens.*, vol. 32, no. 5, pp. 1029–1040, Sep. 1994.
- [22] M. Soumekh, “Reconnaissance with slant plane circular SAR imaging,” *IEEE Trans. Image Process.*, vol. 5, no. 8, pp. 1252–1265, Aug. 1996.

- [23] E. Meier, U. Frei, and D. Nüesch, *SAR Geocoding: Data and Systems*. Karlsruhe, Germany: Wichmann, 1993, ch. Precise Terrain Corrected Geocoded Images, pp. 173–186.
- [24] A. Schubert, “Stereo-assisted interferometric SAR, Chap. 3.4 Geocoding,” Ph.D. dissertation, Univ. Zurich, Zurich, Switzerland, 2004.
- [25] M. Unser, A. Aldroubi, and M. Eden, “B-spline signal processing: Part I—Theory,” *IEEE Trans. Signal Process.*, vol. 41, no. 2, pp. 821–832, Feb. 1993.
- [26] M. Unser, A. Aldroubi, and M. Eden, “B-spline signal processing: Part II—Efficient design and applications,” *IEEE Trans. Signal Process.*, vol. 41, no. 2, pp. 834–848, Feb. 1993.
- [27] O. Frey, E. Meier, and D. Nüesch, “Processing SAR data of rugged terrain by time-domain back-projection,” in *Proc. SPIE*, vol. 5980, Bruges, Belgium, Sep. 2005, pp. 1–9.
- [28] O. Frey, E. Meier, and D. Nüesch, “An integrated focusing and calibration procedure for airborne SAR data,” in *Proc. EUSAR*, Dresden, Germany, May 2006, pp. 1–4.
- [29] D. Fraser, “Interpolation by the FFT revisited - An experimental investigation,” *IEEE Trans. Acoust., Speech, Signal Process.*, vol. 37, no. 5, pp. 665–675, May 1989.
- [30] “AEROcontrol IId Product Description,” [Online]. Available: http://www.igi-systems.com/downloads/specifications/specifications_aerocontrol.pdf, 2006.
- [31] G. Fornaro, G. Franceschetti, and S. Perna, “Motion compensation errors: Effects on the accuracy of airborne SAR images,” *IEEE Trans. Aerosp. Electron. Syst.*, vol. 41, no. 4, pp. 1338–1352, Oct. 2005.
- [32] ASAR-Cal/Val-Team, “Quality Measurements Definition for ASAR Level 1 Products,” ESA, Frascati, Italy, Tech. Rep. Iss. 1, Mar. 2002.
- [33] B. Rosich and P. Meadows, “Absolute calibration of ASAR level 1 products generated with PF-ASAR,” ESA, Frascati, Italy, Tech. Rep. Iss. 1 rev. 5, Oct. 2004.
- [34] A. Monti Guarnieri and C. Prati, “SAR interferometry: A “Quick and Dirty” coherence estimator for data browsing,” *IEEE Trans. Geosci. Remote Sens.*, vol. 35, no. 3, pp. 660–669, May 1997.

3 Tomographic Imaging of a Forested Area By Airborne Multi-Baseline P-Band SAR

This chapter has been published as: O. Frey, F. Morsdorf, and E. Meier, 2008. Tomographic Imaging of a Forested Area By Airborne Multi-Baseline P-Band SAR. Sensors, Special Issue on Synthetic Aperture Radar, 8(9):5884–5896.

Abstract

In recent years, various attempts have been undertaken to obtain information about the structure of forested areas from multi-baseline synthetic aperture radar data. Tomographic processing of such data has been demonstrated for airborne L-band data but the quality of the focused tomographic images is limited by several factors. In particular, the common Fourier-based focusing methods are susceptible to irregular and sparse sampling, two problems, that are unavoidable in case of multi-pass, multi-baseline SAR data acquired by an airborne system. In this paper, a tomographic focusing method based on the time-domain back-projection algorithm is proposed, which maintains the geometric relationship between the original sensor positions and the imaged target and is therefore able to cope with irregular sampling without introducing any approximations with respect to the geometry. The tomographic focusing quality is assessed by analysing the impulse response of simulated point targets and an in-scene corner reflector. And, in particular, several tomographic slices of a volume representing a forested area are given. The respective P-band tomographic data set consisting of eleven flight tracks has been acquired by the airborne E-SAR sensor of the German Aerospace Center (DLR).

3.1 Introduction

In a conventional synthetic aperture radar (SAR) image multiple back-scattering elements distributed along the elevation component are projected to the two-

dimensional slant-range plane. With Pol-InSAR techniques only a very limited number of different scattering elements can be localized within a resolution cell. Tomographic processing of SAR data, however, allows resolving the ambiguity in the elevation component and is therefore suitable to produce true three-dimensional images. Hence, different back-scattering elements within a volume can directly be localized. This property can be exploited for the reconstruction of volumetric structures, such as forested areas, as well as for a more detailed imaging of built-up areas and mountainous regions, which exhibit a high percentage of layover regions.

Tomographic processing of SAR data requires that the synthetic aperture in azimuth be extended by a second dimension in direction orthogonal to the plane spanned by the vectors in azimuth and the line of sight. The sampling in this direction, called the normal direction, is realized by coherently combining the data of a sufficient number of adequately separated flight tracks. The common Fourier-based SAR processing algorithm, the SPECAN (SPECtral ANalysis) approach, which has been used in [1], requires that the synthetic aperture be sampled regularly and densely. In reality, the sampling spacing is not uniform in case of airborne SAR data of multiple acquisition paths, and the synthetic aperture in the normal direction is sampled sparsely. As a result the tomographic image is subject to defocusing, high side lobes and ambiguities in the normal direction. In order to overcome the ambiguity problem and to improve the resolution modern spectral estimation methods have been proposed as a substitute to spectral estimation by FFT. These methods include spectral estimation by the Capon method [2] and subspace-based spectral estimators such as the MUSIC algorithm [3] [4]. These methods replace the last step, the spectral estimation by FFT, but any geometric approximation made in a previous processing step is still present in the data. We adopt a time-domain back-projection (TDBP) processing technique, which maintains the entire three-dimensional geometric relationship between the measured sensor positions and the illuminated area while focusing the data. So, the key feature of the TDBP approach is an accurate handling of the complex geometry of multi-baseline airborne SAR data. An extensive airborne SAR campaign has been accomplished in September 2006. Two fully polarimetric tomographic data sets - an L-band and a P-band data set - of a partially forested area have been acquired by the German Aerospace Center's E-SAR.

In the next section, the Fourier-based SPECAN approach is revised in order to highlight the approximations that are involved. The same framework is also used

to derive the sampling constraints and the spatial resolution for the design of the tomographic experiment and the data processing in the normal direction. Then, the formulation of the TDBP algorithm for tomographic processing is given. Further, the measurement set-up of the tomographic P-band SAR experiment is described and the focusing quality is assessed by analysing simulated and real point targets. Finally, the results obtained from the TDBP-based tomographic reconstruction of a forested area from the E-SAR P-band data are presented.

3.2 The SPECAN Algorithm, Resolution and Sampling in the Normal Direction

For the first demonstration of airborne L-band SAR tomography [1] the three-dimensional focusing of the data was accomplished by a combination of the extended chirp scaling algorithm [5], which was used to focus each data track in range and azimuth direction, and the SPECAN algorithm, which was applied to focus the data in the normal direction. The SPECAN approach was originally designed for azimuth compression of ScanSAR data. The peculiarity of this algorithm lies in the fact that the focused data is obtained by a Fourier transform after a deramping operation.

We want to look again in some detail at the derivation of the SPECAN algorithm for focusing in the normal direction for two reasons: first, to highlight the approximations that are involved in the SPECAN approach, and second, because it provides a good framework to derive two important parameters, the *spatial resolution* δ_n and the *Nyquist sampling spacing* d_n in the normal direction.

The model that is used to derive these parameters follows to a large extent the derivation presented in [1]. However, the signal model is loosely based on the derivation of the SPECAN algorithm for azimuth focusing as it is presented in [6].

The simplified tomographic acquisition geometry that forms the basis for the derivation of the spatial resolution and the sampling constraints in normal direction n – i.e. orthogonal to the plane spanned by the slant-range direction and the azimuth direction – is depicted in Fig. 3.1. r_0 is the range distance at the point of closest approach along the synthetic aperture in normal direction n . Equally spaced baselines d_n are assumed and the variation of the off-nadir angle is neglected, so, the vector \vec{n} in normal direction is assumed to be invariant

for all acquisition paths. Target coordinates are identified by a bar above the symbol. Assuming that the synthetic aperture in the normal direction n is con-

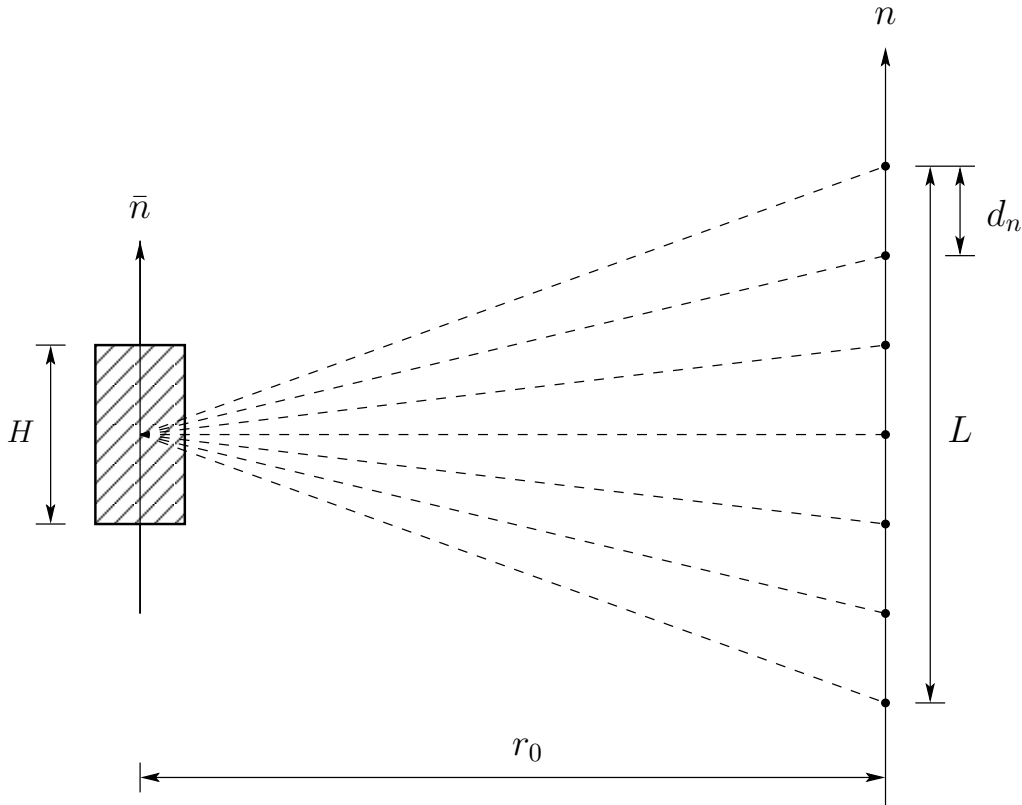


Figure 3.1: Simplified tomographic imaging geometry after [1]. A volume is illuminated from different positions along a synthetic aperture in normal direction n . Each position in normal direction corresponds to a sensor path in azimuth direction. The sensor paths are separated by a constant sampling spacing d_n . The maximal height of the volume is H . L is the length of the synthetic aperture in normal direction.

tinuous - imagine an infinite number of single look complex images, represented by s_r , acquired from an infinite number of different, parallel flight tracks along n - the focused signal in normal direction $v(\bar{n}_0)$ at position \bar{n}_0 in the object space can be written as the following convolution in the time domain:

$$v(\bar{n}_0) = \int_{-L/2}^{L/2} s_r(\bar{n}_0 - n)h(n)dn \quad (3.1)$$

This is equivalent to:

$$v(\bar{n}_0) = \int_{\bar{n}_0-L/2}^{\bar{n}_0+L/2} s_r(n)h(\bar{n}_0 - n)dn \quad (3.2)$$

L is the length of the synthetic aperture in normal direction n . s_r is the demodulated, received signal. h is the matched filter, i.e. the time-reversed reference function, which can be written as:

$$h(\bar{n}_0 - n) = \exp\left(\frac{ik}{r_0}(\bar{n}_0 - n)^2\right) \quad (3.3)$$

This formulation implements a quadratic phase history, which is obtained by approximating the hyperbolic range history by a second order Taylor series expansion about the point $n = \bar{n}_0$:

$$r(n, \bar{n}_0) = 2\sqrt{r_0^2 + (\bar{n}_0 - n)^2} \simeq 2r_0 + \frac{(\bar{n}_0 - n)^2}{r_0}. \quad (3.4)$$

$r(n, \bar{n}_0)$ is the two-way path length between the sensor at position n and a back-scatterer within the observed volume at height \bar{n}_0 , with a range distance r_0 at the point of closest approach. Inserting eq. (3.3) into eq. (3.2) and expanding the quadratic phase term yields:

$$v(\bar{n}_0) = \exp\left(\frac{ik}{r_0}\bar{n}_0^2\right) \cdot \int_{\bar{n}_0-L/2}^{\bar{n}_0+L/2} \underbrace{s_r(n) \exp\left(\frac{ik}{r_0}n^2\right)}_{s_d(n)} \exp\left(-\frac{i2k}{r_0}\bar{n}_0n\right) dn. \quad (3.5)$$

The exponential within the underbraced term in eq. (3.5) can be interpreted as a deramping operation which leads to the deramped signal s_d . Then, the whole integral is equivalent to a Fourier transform of the deramped signal s_d :

$$v(\bar{n}_0) = \exp\left(\frac{ik}{r_0}\bar{n}_0^2\right) \int_{\bar{n}_0-L/2}^{\bar{n}_0+L/2} s_d(n) \exp\left(-\frac{i2k}{r_0}\bar{n}_0n\right) dn. \quad (3.6)$$

So, in practice, the focused image $v(\bar{n}_0)$ can be obtained by applying a FFT to the deramped signal s_d .

The phase term in the exponent of eq. (3.6) can be written as:

$$-\frac{2k}{r_0}\bar{n}_0n = -K_{nr}\bar{n}_0n \quad (3.7)$$

where $K_{nr} = \frac{2k}{r_0}$ is interpreted as the spatial frequency modulation rate of the signal in normal direction. As it is well known from pulse compression of linear FM signals in range direction, the resolution in the time domain after compression is given by the reciprocal of the processed bandwidth, which is the product of the FM rate and the integration time. Translated to the normal direction and expressed in the spatial domain, the spatial resolution δ_n is the inverse of the product of the spatial frequency modulation rate K_{nr} and the integration path L times 2π :

$$\delta_n = \frac{2\pi}{K_{nr} \cdot L} = \frac{2\pi}{\frac{2 \cdot 2\pi}{r_0 \lambda} \cdot L} = \frac{\lambda r_0}{2L}. \quad (3.8)$$

The Nyquist sampling spacing d_n in normal direction is equivalent to the inverse of the spatial bandwidth k_n times 2π , where $k_n(\bar{n}_0) = K_{nr} \cdot \bar{n}_0 = \frac{2k}{r_0} \bar{n}_0$:

$$d_n(\bar{n}_0) \leq \left| \frac{2\pi}{k_n(\bar{n}_0)} \right| = \frac{2\pi}{K_{nr} \cdot \bar{n}_0} = \frac{\lambda r_0}{2\bar{n}_0}. \quad (3.9)$$

Eq. (3.9) describes the relationship between sampling spacing and the maximal height $\bar{n}_0 = H$ of the imaged volume that can be reconstructed unambiguously:

$$d_n(\bar{n}_0 = H) \leq \frac{\lambda r_0}{2H}. \quad (3.10)$$

The respective values for the nominal resolution δ_n and the unambiguous height H , which correspond to the tomographic P-band data set presented in this paper, are given in Table 3.2.

3.3 3D Focusing in the Time-Domain

In [7] an algorithm has been proposed which is based on single look complex images processed by the extended chirp scaling algorithm including aircraft motion compensation to a straight line. However, instead of focusing the data by deramping and spectral estimation, which would previously involve generating synthetic tracks and a regularization of the samples in the normal direction, a time-domain beamformer (TDB) was applied to focus the data in the third dimension. Every voxel within the volume is focused by a so-called *ad hoc* reference function as it is also known from time-domain back-projection processing. The focusing quality of the TDB approach was found to be superior to the

SPECAN based algorithm presented in [1] for unevenly spaced baselines. But in spite of the fact that the TDB directly accounts for the irregular track distribution in normal direction it is still based on artificial, linearized flight tracks, which lie in parallel to each other and which do not represent the true geometry of the flight tracks. In [8] an enhanced method for tomographic focusing of multi-baseline airborne SAR data has been proposed. The core improvement consists of an approximative height-dependent motion compensation and coregistration (HMCC) method. The HMCC approach starts with a stack of range- and azimuth-focused SAR images, which were processed using the extended chirp scaling algorithm including motion compensation with respect to a fixed reference terrain height. Thus, the height dependent motion compensation and coregistration approach is applied to the already focused 2D images. The HMCC approach consists of a so-called *un-moco* step where the motion compensation to the nominal (linearized) track is undone. Then for each 2D SAR image and each height occurring in the tomogram a new post-processing motion compensation (*re-moco*) to the nominal track is carried out with respect to the height under consideration. Eventually, the images are coregistered according to the reference height, to which they have been post-processed. Having applied this HMCC method to an L-band multi-baseline data set the authors of [8] report a considerable improvement in focusing quality compared to the tomographic processing without any height dependent corrections.

We aim at a complete processing in the time domain – after range compression – and focus the data by using the true geometry of the irregularly sampled tomographic acquisition pattern. I.e., every voxel of the 3D SAR image is focused based on the true acquisition geometry, limited only by the accuracy of the navigation data and uncompensated propagation delays. A TDBP processor, which has been tested with airborne [9] and spaceborne SAR data [10], has been extended in order to work with a two-dimensional synthetic aperture. The key idea is that the geometric relationship between every sensor position and the illuminated volume is maintained during focusing without introducing any geometric approximations. Following the signal model presented in [10] the back-projected signal s_k corresponding to the flight track k can be expressed as a function of the position \vec{r}_i on the reconstruction grid:

$$s_k(\vec{r}_i) = \sum_{j=a_k(\vec{r}_i)}^{b_k(\vec{r}_i)} g_k(R_{k_{ij}}, \vec{r}_{S_{jk}}) \cdot R_{k_{ij}} \cdot \exp(i2k_c R_{k_{ij}}) . \quad (3.11)$$

\vec{r}_i	: position vector of the target
a_k, b_k	: indices of first, last azimuth position of the sensor within the synthetic aperture of the target position \vec{r}_i
$\vec{r}_{S_{jk}}$: position vector of the sensor, $j \in [a_k, b_k]$
$R_{k_{ij}}$	$= \vec{r}_i - \vec{r}_{S_{jk}} $: range distance
$g_k(\cdot)$: range-compressed signal of data track k
k_c	$= 2\pi f_c/c$: central wavenumber
f_c	: carrier frequency
c	: speed of light

By extending the coherent addition of the signal contributions to the normal direction the back-projected signal v is obtained, which maps the volume at the position \vec{r}_i :

$$v(\vec{r}_i) = \sum_{k=1}^m \sum_{j=a_k(\vec{r}_i)}^{b_k(\vec{r}_i)} g_k(R_{k_{ij}}, \vec{r}_{S_{jk}}) \cdot R_{k_{ij}} \cdot \exp(i2k_c R_{k_{ij}}), \quad (3.12)$$

where m is the number of flight tracks that build the tomographic pattern. The boundaries of the synthetic aperture in azimuth direction, a_k and b_k , vary as a function of the grid position \vec{r}_i . This means that we sum up the contributions from those sensor positions $\vec{r}_{S_{jk}}$ which actually build the synthetic aperture for the grid position \vec{r}_i . Note that an appropriate interpolation procedure (interpolation by FFT) is required in order to retrieve the data values at the correct range distances because of the discrete representation of the range-compressed data.

3.4 Experimental Set-Up

An extensive airborne SAR campaign has been carried out in September 2006. Two fully polarimetric tomographic data sets - a P-band and an L-band data set - of a partially forested area have been acquired by the German Aerospace Center's E-SAR system. Eight corner reflectors were deployed for geometric and radiometric calibration purposes. The positions of the corner reflectors were measured by carrier-phase differential GPS. In the following, we restrict ourselves to describing the results obtained so far with the P-band data set.

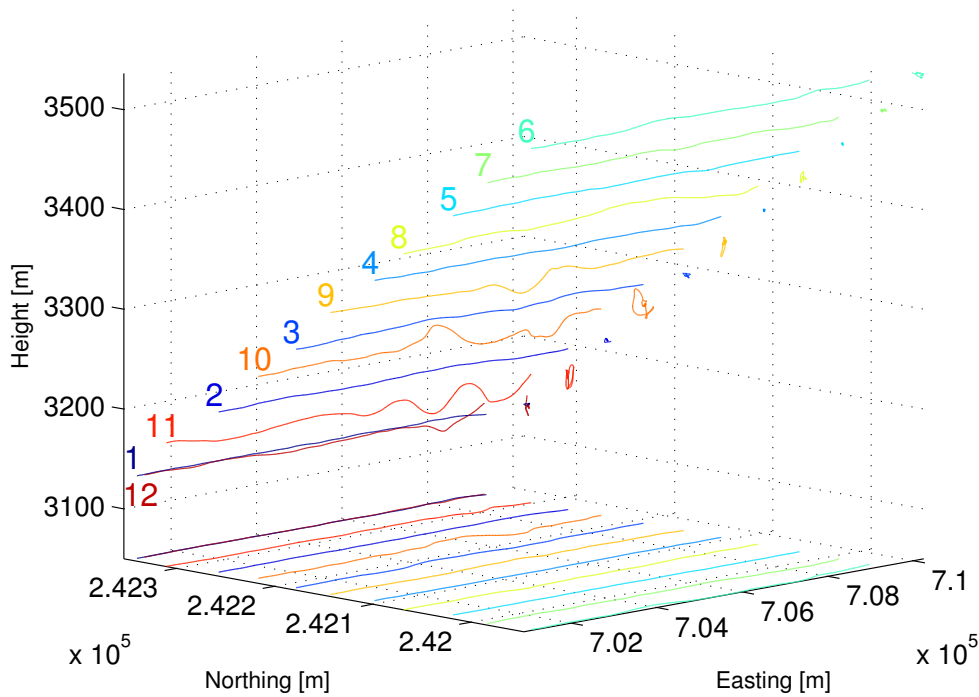


Figure 3.2: P-band tomographic acquisition pattern consisting of 11 flight tracks + 1 control track. The flight direction is from east to west and the sensor is left-looking. In addition to the actual flight tracks, their projections to the horizontal plane and to the northing-height plane are depicted.

The relationship of the sampling spacing d_n in normal direction and the height H of the volume that may be imaged unambiguously is given by eq. (3.10), and spatial resolution δ_n is given by eq. (3.8). Given a limited number of sensor passes a trade-off has to be made between the achievable resolution and the maximal unambiguous height H .

For the design of our experiment the total number of flight tracks that span the synthetic aperture in normal direction was limited to 11 tracks. We have chosen a regular distribution of the flight tracks orthogonal to a mean line of sight at an off-nadir angle of 45° (see Fig. 3.4) with horizontal and vertical baselines of 40 m. This results in a sampling spacing $d_n = 56.7$ m and a synthetic aperture $L = 567$ m in the normal direction. Using these figures, a mean range distance $r_0 = 3900$ m, and the wavelength of the carrier signal $\lambda = 0.856$ m we obtain a nominal spatial resolution $\delta_n \approx 3$ m and a nominal unambiguous height $H \approx 30$ m in normal direction.

Table 3.1: E-SAR P-band system parameters.

Carrier frequency	350 MHz
Chirp bandwidth	70 MHz
Sampling rate	100 MHz
Polarizations	HH-HV-VV-VH
PRF	500 Hz
Ground speed	90 m/s

Table 3.2: Nominal parameters used in the set-up of the P-band tomographic SAR experiment.

Number of flight tracks	11+1
Nominal track spacing d_n	56.7 m
Horizontal baselines	40 m
Vertical baselines	40 m
Synthetic aperture in normal direction L	567 m
Nominal resolution in normal direction δ_n	3 m
Approx. unambiguous height H	30 m

In Table 3.1 the parameters of the E-SAR P-band system are summarized. Note that the reduced chirp bandwidth of only 70 MHz in the P-band is due to restrictions imposed by the Swiss Federal Office of Communications to prevent interference of the radar signal with existing RF communication services within the band 390-395 MHz. The nominal chirp bandwidth would be 94 MHz. The E-SAR system is equipped with a modern computer-controlled CCNS4 navigation system combined with a highly precise DGPS/IMU system of the type AEROcontrol IId, both by IGI mbH. The relative positioning accuracy is approximately 0.01 m RMS (see [11]), the accuracies of the attitude angles are given as $\sigma_{\theta_r} = \sigma_{\theta_p} = 0.004^\circ$ RMS for roll and pitch angle and $\sigma_{\theta_h} = 0.01^\circ$ RMS for the heading, and the velocity is measured with an accuracy of $\sigma_V = 0.005$ m/s [12].

The TDBP-based tomographic processing of the P-band data set as presented

in this paper does not include a point target based phase calibration. For the E-SAR P-band system the carrier frequency is $f_c = 350$ MHz and the respective wavelength is $\lambda_c \approx 0.86$ m. A range error $r_e = 0.01$ m corresponds approximately to $\lambda_c/80$ or equivalently, to a phase error $\varphi_e = \pi/20$. Thus, the impact on the tomographic focusing quality is relatively small compared to the L-band case, where the wavelength is shorter by a factor of 3.7 and tomographic processing of the multi-baseline data set is not feasible without appropriate phase calibration.

The 12 P-band data sets were acquired within one air mission. The maximal time span between the first and the last track is approximately 2 h. The tracks of the tomographic pattern were flown in an interleaved manner in case that an unexpected incidence would have caused an untimely abortion of the data acquisition. In Fig. 3.4 the geometric configuration of the flight tracks for the P-band tomographic data set is shown. The flight direction is from east to west and the sensor is left-looking. In addition to the actual flight tracks, their projections to the horizontal plane and to the northing-height plane are also depicted. The mission was completed by a control track which has the same nominal flight geometry as the first track. This allows assessing the amount of temporal decorrelation between the first and the last track. Table 3.2 contains a summary of the parameters which characterize the tomographic data set.

As an external reference, a digital elevation model (DEM) derived from airborne laser scanning (Falcon II, Toposys GmbH) is available for comparison of the ground level and a digital surface model (DSM) acquired by the same sensor is also at hand. The airborne laser scanning data were acquired in spring of 2003. It has to be assumed that the deciduous trees were mostly transparent to the laser signal and therefore do not appear in the LiDAR-derived DSM. In view of this limitation a region that is dominated by coniferous trees has been chosen as test area.

3.5 Simulated Data

In order to quantify the performance of the tomographic processing by TDBP two complete tomographic P-band raw data sets have been simulated and then focused. The raw data simulator emulates the true 3D acquisition geometry using the navigation data of the actual flight tracks and the 3D position of a point target. The same system parameters have been used as they are given for

the real-world P-band data set acquired by the E-SAR system.

In Fig. 3.5 the respective impulse responses resulting from TDBP tomographic imaging in the normal direction are given for the three cases: a single simulated point target (black line), two simulated point targets which are separated by a distance of 12 m in normal direction (red line), and a real, in-scene corner reflector (blue line). The simulated data is based on exactly the same geometry as in the real situation. In all cases the point targets are focused properly in terms of resolution ($\delta_n \approx 3$ m). But, the focused signal of the two simulated point targets aligned along the normal direction exhibits a rather strong ambiguous target detection and the focused signal of the in-scene corner reflector shows a considerable amount of anomalous side lobes.

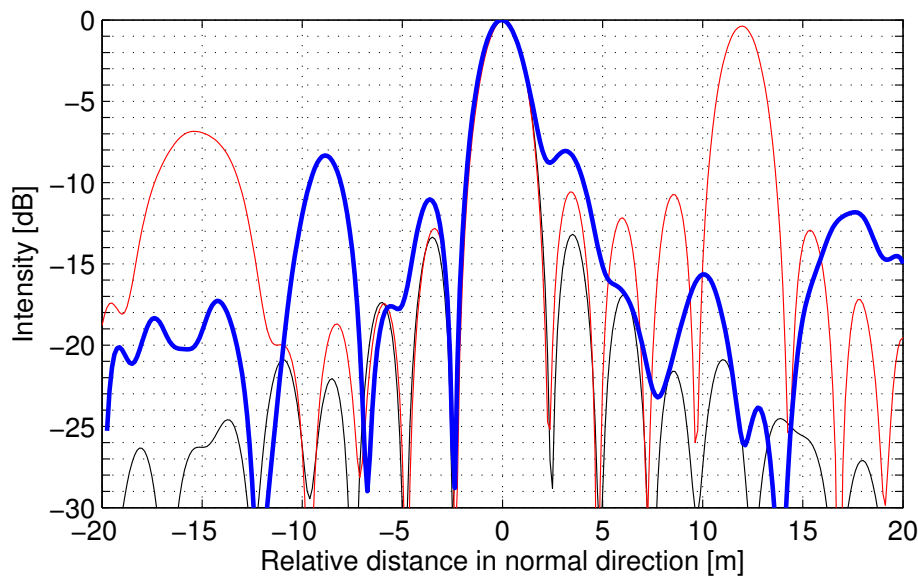


Figure 3.3: Impulse responses resulting from TDBP tomographic imaging of the multi-baseline P-band raw data set of: a single simulated point target (black line), two simulated point targets which are separated by a distance of 12 m in normal direction (red line), a real, in-scene corner reflector (blue line).

3.6 Experimental Results

A partially forested area of 400 m x 1000 m size has been selected in order to demonstrate tomographic processing by TDBP using the HH channel of the

multi-baseline P-band SAR data set. Since the selected area is relatively flat, a 3D reconstruction grid consisting of a set of *horizontal* layers has been chosen. The voxel spacing is 1 m for both, easting and northing direction, and 1.5 m in vertical direction. A top view of the test area is given in Fig. 3.4(a) in the form of an orthorectified RGB image. As an external reference data set the LiDAR-based DEM and DSM are used. The RGB ortho-image has been taken at the time of acquisition of the airborne laser scanning data. In Fig. 3.4(b), a horizontal layer (height level $H = 551$ m) of the SAR tomographic image is depicted. The coherence map (see Fig. 3.4(c)) of the zero baseline configuration obtained from track No. 1 and control track No. 12. indicates a low temporal decorrelation for the forested regions of the test area during the total time of data acquisition. All data sets have been processed to zero Doppler centroid frequency.

Seven vertical tomographic slices of the imaged volume separated by a regular spacing have been selected for visualization: In Fig. 3.6 three slices (No. 1-3) running in south-northern direction at easting values $E = 704400$ m, $E = 704500$ m, and $E = 704600$ m are depicted and in Fig. 3.6 four slices (No. 4-7) running in west-eastern direction at northing values from $N = 239300$ m to $N = 239900$ m are given. For smoother visualization the data have been upsampled in the vertical direction by a factor of 2 after focusing. The tomographic slices represent the measured radar intensity values in dB. The red and the green lines indicate the reference height information obtained from the laser DEM or DSM, respectively.

3.7 Discussion and Conclusion

To the authors' knowledge, for the first time P-band tomographic SAR images of a larger forested area (400 m x 1000 m) have been presented. Compared to previous work in the field of SAR tomography (e.g. [1,7]) a different 3D focusing concept, namely, a complete time-domain back-projection processing to a 3D reconstruction grid, has been successfully applied.

A comparison of the tomographic slices resulting from the airborne multi-baseline P-band data set with the DEM/DSM obtained from laser scanning indicates that high intensity values are predominantly located at the ground level within forested areas. This outcome conforms with what can be expected from horizontally polarized P-band radar back-scattering of a forested area,

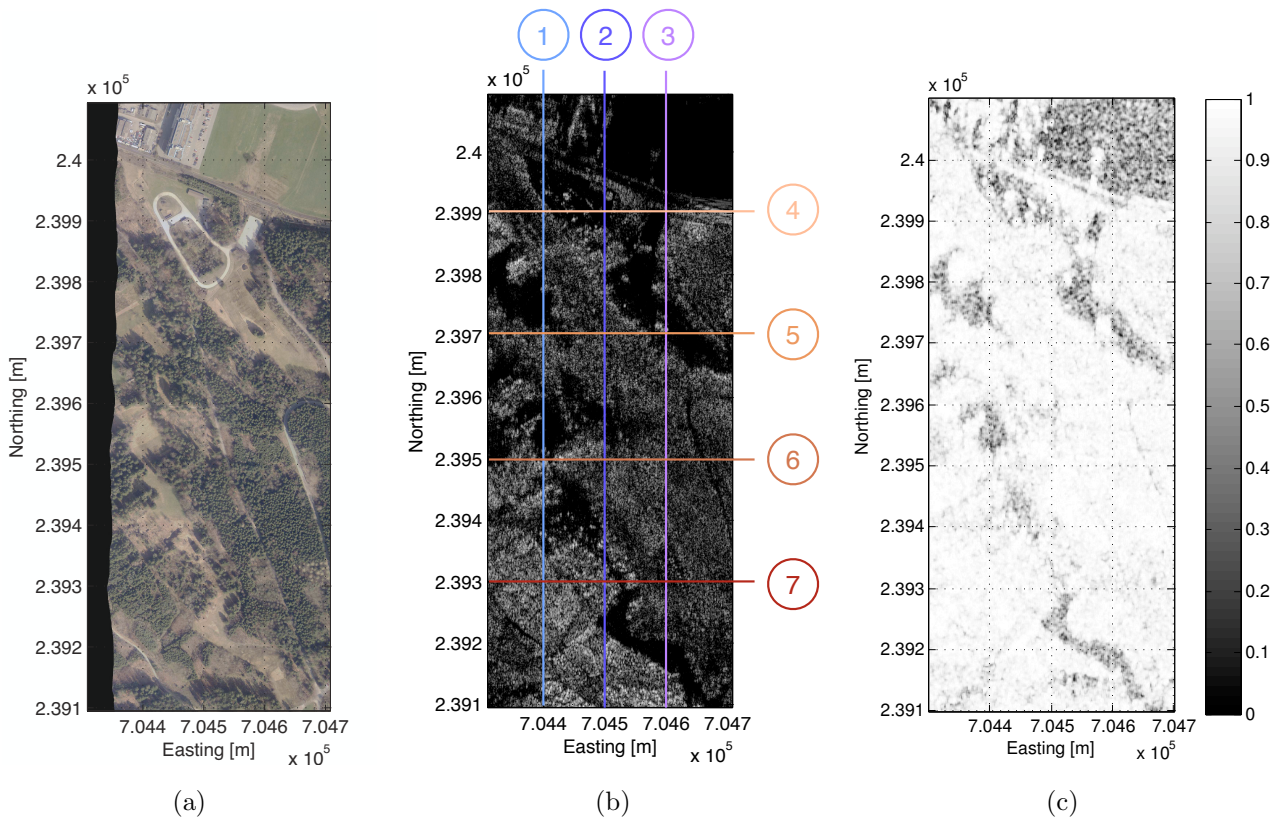


Figure 3.4: (a) RGB ortho-image of the partially forested area selected for tomographic imaging taken at the time of acquisition of the reference DEM/DSM data sets by airborne laser scanning (Falcon II, TopoSys GmbH), (b) SAR intensity values within a horizontal tomographic slice of the reconstruction grid on the height level $H = 551$ m. (c) Coherence map of the zero baseline configuration (track no. 1 and track no. 12).

where double-bounce scattering from the ground surface and tree trunks is a dominant scattering mechanism. Furthermore, this result supports the claim that DEMs obtained by means of P-Band interferometry provide a good estimation of the ground topography underneath canopy.

However, high intensity values within the tomographic images are often accompanied by considerable side lobes and ambiguities in the normal direction.

The simulations show that the point targets are well-focused by tomographic processing using the TDBP algorithm in terms of resolution and separability. The anomalous side lobes that appear for the in-scene corner reflector might be due to a remaining geometric calibration error of the multi-baseline data. If multiple targets are distributed along the normal direction the focused signal is disturbed by ambiguities as a result of the sparsely sampled synthetic aperture

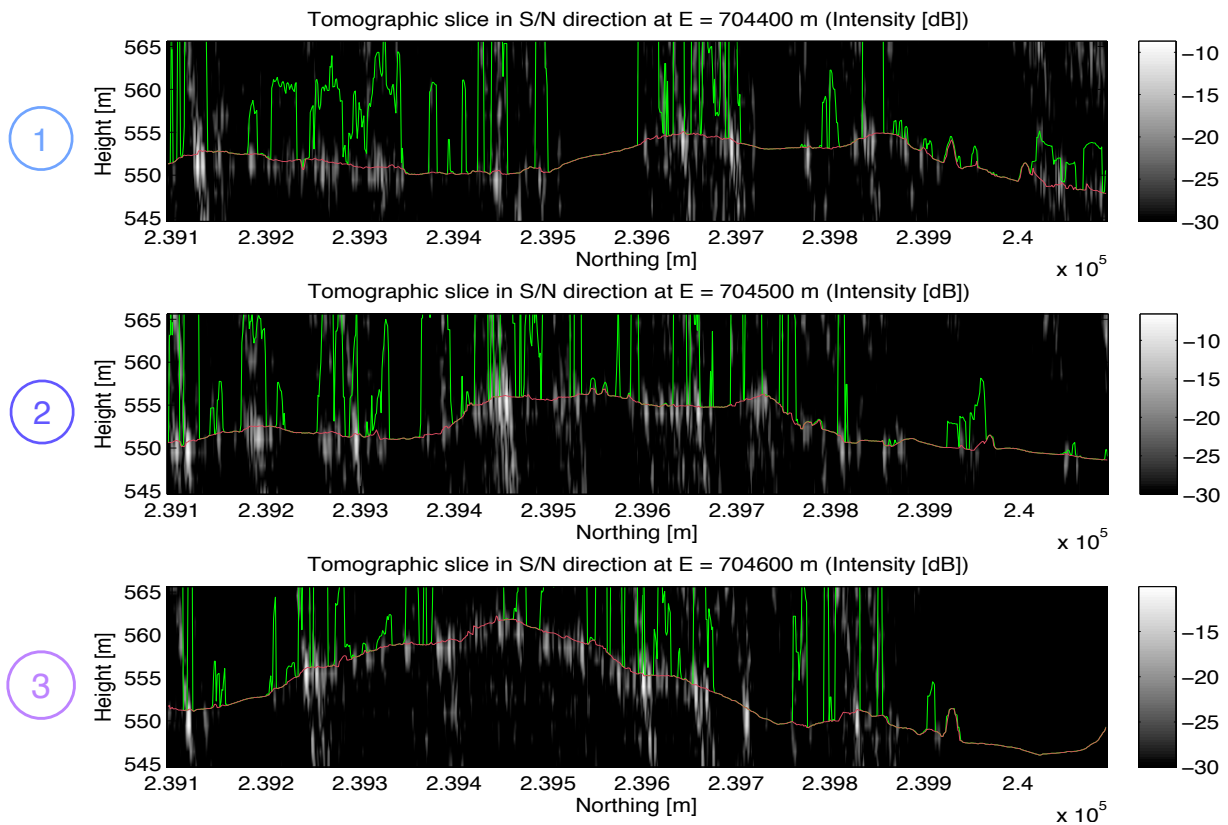


Figure 3.5: Vertical slices of the SAR tomographic image in south-northern direction. Red/green lines in the tomographic slices: High resolution DEM/DSM from airborne laser scanning (Falcon II, TopoSys GmbH) indicating the ground level and canopy height as a reference.

in normal direction. This system inherent problem is given by the limited unambiguous height in the normal direction. Therefore, suppression of ambiguities is a main concern in order to further improve the quality of the tomographic images in a future step.

Acknowledgment

The authors would like to thank R. Horn, R. Scheiber and M. Keller at the German Aerospace Center (DLR) for their ongoing cooperation and technical support. They would also like to thank the procurement and technology center of the Swiss Federal Department of Defense (armasuisse) for funding and supporting this work.

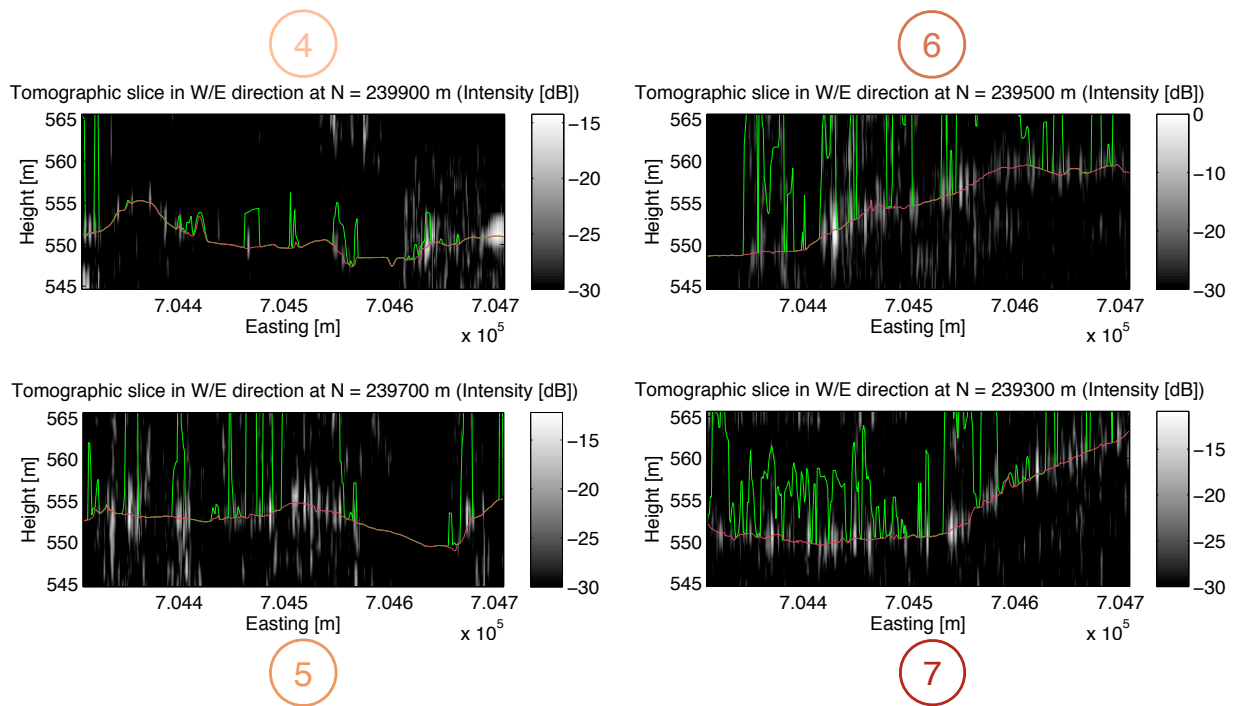


Figure 3.6: Vertical slices of the SAR tomographic image in west-eastern direction. Red/green lines in the tomographic slices: High resolution DEM/DSM from airborne laser scanning (Falcon II, TopoSys GmbH) indicating the ground level and canopy height as a reference.

References

- [1] A. Reigber and A. Moreira, “First Demonstration of Airborne SAR Tomography Using Multibaseline L-Band Data,” *IEEE Transactions on Geoscience and Remote Sensing*, vol. 38, no. 5, pp. 2142–2152, 2000.
- [2] F. Lombardini and A. Reigber, “Adaptive spectral estimation for multibaseline SAR tomography with airborne L-band data,” in *IEEE International Geoscience and Remote Sensing Symposium, IGARSS '03*, vol. 3, 2003, pp. 2014–2016.
- [3] S. Guillaso and A. Reigber, “Polarimetric SAR Tomography (POLTOM-SAR),” in *Proceedings of POLINSAR'05, Frascati, Italy*, 2005.
- [4] F. Gini and F. Lombardini, “Multibaseline cross-track SAR interferometry: a signal processing perspective,” *IEEE Aerospace and Electronic Systems Magazine*, vol. 20, no. 8, pp. 71–93, 2005.
- [5] A. Moreira and Y. Huang, “Airborne SAR Processing of Highly Squinted

- Data Using a Chirp Scaling Approach with Integrated Motion Compensation,” *IEEE Transactions on Geoscience and Remote Sensing*, vol. 32, no. 5, pp. 1029–1040, Sep. 1994.
- [6] I. G. Cumming and F. H. Wong, *Digital Processing of Synthetic Aperture Radar Data: Algorithms and Implementation*. Boston, London: Artech House Inc., 2005.
- [7] M. Nannini and R. Scheiber, “A Time Domain Beamforming Algorithm for SAR Tomography,” in *Proc. of EUSAR 2006 - 6th European Conference on Synthetic Aperture Radar*, 2006.
- [8] M. Nannini and R. Scheiber, “Height dependent motion compensation and coregistration for airborne SAR tomography,” in *International Geoscience and Remote Sensing Symposium, 2007. IGARSS 2007*, 2007, pp. 5041–5044.
- [9] O. Frey, E. Meier, and D. Nüesch, “An Integrated Focusing and Calibration Procedure for Airborne SAR Data,” in *Proc. of EUSAR 2006 - 6th European Conference on Synthetic Aperture Radar*, 2006.
- [10] O. Frey, E. Meier, and D. Nüesch, “A Study on Integrated SAR Processing and Geocoding by Means of Time-Domain Backprojection,” in *Proceedings of the Int. Radar Symposium, Berlin*, 2005.
- [11] A. Reigber and A. Ulbricht, “P-band repeat-pass interferometry with the DLR experimental SAR,” in *International Geoscience and Remote Sensing Symposium, 1998. IGARSS '98*, vol. 4, 1998, pp. 1914–1916.
- [12] “AEROcontrol IId Product Description,” [Online]. Available: http://www.igi-systems.com/downloads/specifications/specifications_aerocontrol.pdf, 2006.

4 3D SAR Imaging of a Forest Using Airborne Multibaseline Data at L- and P-Band

This chapter has been submitted as: O. Frey, E. Meier, 2010. 3D SAR Imaging of a Forest Using Airborne Multibaseline Data at L- and P-Band. IEEE Transactions on Geoscience and Remote Sensing, submitted, June 2010.

Abstract

In this paper, a time-domain back-projection based tomographic processing approach to a three-dimensional reconstruction grid is detailed, the focusing in the third dimension being either modified versions of multilook standard beamforming, robust Capon beamforming, or multiple signal classification. The focusing methods have been applied to experimental multibaseline quad-pol SAR data at L- and P-band acquired by DLR's E-SAR sensor. An analysis of the focusing performance is given for the full as well as a reduced synthetic aperture in the normal direction. The analysis indicates that robust Capon beamforming or multiple signal classification by using a reduced number of baselines can indeed deliver a similar focusing performance as multilook beamforming using the full aperture, however, at the cost of sacrificing the polarimetric channels' phase information. Thus, it is supposed that for a localization of the main scattering sources, e.g., for ground detection at P-band, one of the superresolution techniques can be used with a reduced synthetic aperture. In addition, tomographic images of a partially forested area, including a three-dimensional voxel plot that visualizes the unprecedented level of detail of the tomographic image, are shown.

4.1 Introduction

Tomographic imaging using multibaseline (MB) synthetic aperture radar (SAR) data extends the two-dimensional imaging capabilities of conventional SAR to

the third dimension by forming a synthetic aperture in two dimensions, the azimuth direction and the normal direction (orthogonal to both, azimuth direction and the line of sight). In a single SAR image multiple back-scattering elements distributed along the normal direction are projected to the two-dimensional slant-range plane and can therefore not be resolved. PolInSAR techniques [1] already provide a means to discriminate the phase centers of different scattering mechanism in the normal direction from a fully polarimetric single-baseline dataset. However, the approach is limited to cases where no more than one scatterer with the same scattering mechanism occurs or where no generally distributed scattering mechanisms are present.

By tomographic processing of MB SAR data, however, different scatterers—with whatever scattering mechanisms—that lie within the same range distance in conventional SAR images are no longer inseparable. This property can be exploited for the reconstruction of volumetric structures that are semitransparent to microwaves and that are subject to volume scattering, such as forested areas, as well as for a more detailed imaging of built-up areas and mountainous regions, which exhibit a high percentage of layover regions.

4.1.1 Previous Work/State of the Art

Tomographic processing of experimental airborne SAR data by means of conventional Fourier beamforming—also termed the spectral analysis (SPECAN) method, which consists of a deramping step followed by a fast Fourier transform (FFT)—has been demonstrated by Reigber and Moreira [2]. However, airborne SAR tomography using FFT-based focusing in the normal direction is affected by unsatisfactory imaging quality as a consequence of sparse sampling and irregular distribution. It has been shown already in [3] that time-domain based beamforming in the normal direction is less susceptible to irregular sampling than FFT-based methods. In recent years, a number of approaches in order to improve the quality of tomographic SAR imaging have been proposed: In [4], an approach similar to the SPECAN method is pursued, the difference being that the FFT is replaced by the Capon beamformer. Fornaro et al. [5] tackled the problem by casting it into a linear inverse problem framework, in particular, using the singular value decomposition (SVD) in order to analyze the amount of independent information. Further, a priori information about the extent of illuminated scene is included in order to stabilize the inversion. The approach was tested using spaceborne SAR data. In [6], a method called linear minimum

mean square error (LMMSE) focusing is proposed which, unlike the SPECAN or SVD method, accounts for the fact that the baselines generally suffer from miscalibration.

Beamforming techniques such as the Capon beamformer [7] and multiple signal classification (MUSIC) [8] provide superresolution, a property which allows for still achieving a high resolution of the tomographic image and good side lobe suppression in spite of using only a shorter synthetic aperture or in spite of the presence of irregular and sparse sampling, respectively. While the MUSIC algorithm possesses an inherent robustness against steering vector errors, as has been shown in [9], in the case of the Capon beamformer, an improved resolution and a better reduction of the side lobes can either be obtained if the steering vector is calibrated perfectly, or, if the Capon beamformer is extended in such a way that the unknown true steering vector \mathbf{a} is estimated along with the power, a method termed robust Capon beamforming (RCB) [10]. In [11], MUSIC beamforming is used for tomographic focusing and a method to estimate the dimension of the signal subspace based on the prolate spheroidal wave functions is proposed with the aim to determine the minimum number of baselines needed for tomographic focusing.

A method that aims at a unified framework including model-based, model-free, and hybrid approaches for simultaneous tomographic imaging and separation of scattering mechanisms based on fully-polarimetric MB SAR data was introduced in [12]. It is based on the assumption that the data covariance matrix can be represented as a sum of Kronecker products (SKP) of a polarimetric signature matrix and a structure matrix. Experimental results at P-band of a forest test site in Sweden also obtained by the E-SAR system with a chirp bandwidth reduced to 30MHz and an estimation window size of $50\text{m} \times 50\text{m}$ (ground range, azimuth) for the sample coherence matrix have been presented including Capon-based tomographic imaging of different polarimetric channels and isolated scattering mechanism.

In [13], a so-called sector interpolation approach is investigated by means of simulated data in order to reconstruct a set of uniform baselines based on a priori information on the potential location of the scattering sources.

The TDBP-based approach that is presented in this paper, although using a different framework, also makes use of that a priori information by processing the data to a 3D reconstruction grid at a known location followed by a recalibration of the data to an evenly-spaced set of baselines. The motivation to

process the data entirely in the time domain is driven by the need to achieve maximal focusing quality for both, L- and P-band MB data sets. Our TDBP-based implementation has proven to yield excellent imaging results even in case of atypical acquisition geometries [14]. In [15, 16], first tomographic images at P-band obtained from an airborne MB data set have been presented using the TDBP method to produce three-dimensional single-look tomograms of a forested area. Despite of having achieved a good focusing performance in terms of resolution, the suppression of anomalous side lobes and ambiguous targets was unsatisfactory supposedly due to single-look focusing in the normal direction.

4.1.2 Aim of This Paper

In this paper, a modified time-domain tomographic processing approach is pursued to obtain a three-dimensional image of a partially forested area: namely, a combination of standard TDBP processing for azimuth focusing and time-domain multilook-based methods for tomographic focusing in the normal direction. Two airborne MB data sets, at L- and P-band [see Table 4.1, p. 102] are used as experimental data to examine the performance of the different algorithms. In particular, the emphasis of this paper is on:

- A detailed description and derivation of the focusing algorithms. A common formulation is given for the three approaches: multilook beamforming (MLBF), RCB, and MUSIC beamforming. The time-domain based MLBF and the RCB methods are both non-parametric methods for direction of arrival estimation, i.e., they make no assumption about the covariance structure of the data [17], whereas the MUSIC method is a parametric approach in the sense that the number of scattering sources is assumed to be known.
- Assessing the tomographic focusing performance on the basis of the impulse response obtained from an in-scene corner reflector and analyzing the imaging capabilities at the two frequencies, L- and P-band, the imaging technique applied for tomographic focusing (MLBF, RCB, MUSIC), as well as, the full and a reduced synthetic aperture in normal direction.
- In addition, a three-dimensional representation as well as vertical slices of the polarimetric tomographic image are given in order to illustrate the high level of detail that is accomplished.

In an attempt to keep separate signal processing issues concerned with tomographic imaging, on the one hand, and the analysis of the resulting data products, on the other hand, this paper is restricted to the imaging part. A thorough analysis of the fully polarimetric MB data including vertical back-scattering profiles for the polarimetric channels and polarimetric decompositions thereof, and comparisons with respect to cross-reference and ground truth data will be treated in a separate paper.

The structure of this paper is as follows. In Section 4.2, the underlying data model and the TDBP processing strategy to a three-dimensional reconstruction grid is presented. All three tomographic focusing methods, MLBF, RCB, and MUSIC beamforming are explained in detail. In Section 4.3, the airborne MB SAR experimental data is described. The results Section 4.4 contains an analysis of the focusing performance and the tomographic images obtained by processing the two MB data sets with the three different beamforming techniques. The results are discussed in Section 4.5, and eventually, conclusions are drawn in Section 4.6.

4.2 Data Model and Focusing Methods

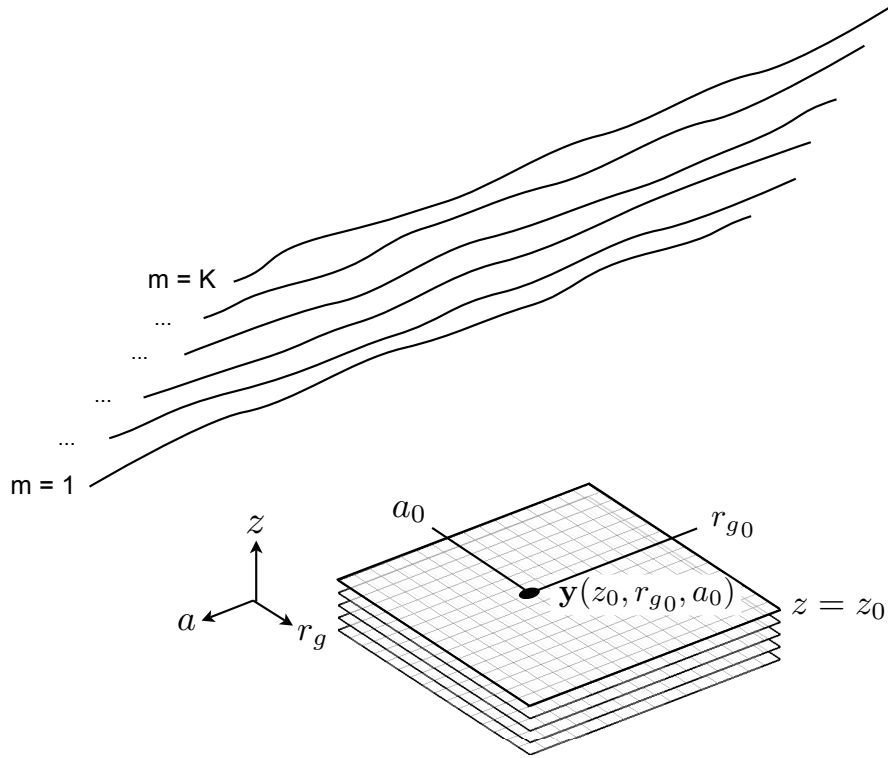
In Fig. 4.1, a MB flight pattern is depicted representing a typical airborne case where motion deviations from ideally linear and parallel flight tracks are present. In addition, the three-dimensional reconstruction grid to which the data are focused within the pursued TDBP processing scheme is depicted. There are K individual flight tracks flown in an, ideally, parallel fashion. The vector $\mathbf{y}(z_0, r_{g0}, a_0)$ contains the demodulated azimuth focused signals from K flight tracks at position (z_0, r_{g0}, a_0) of the reconstruction grid. In general, the signal vector \mathbf{y} is:

$$\mathbf{y}(z, r_g, a) = [y_1(z, r_g, a) \dots y_K(z, r_g, a)]^T \quad (4.1)$$

where r_g is the ground range position, a is the azimuth position, and z indicates the height within the imaged volume.

This representation of the signal vector is given with respect to the coordinate system of the three-dimensional reconstruction grid. For the sake of readability, the horizontal positioning (r_g and a) of the data vector is omitted in the following. Hence, $\mathbf{y}(z)$ is the signal for a specific voxel at height z .

In the following, the signal model is detailed from the point of view of how the



$$\mathbf{y}(z_0, r_{g0}, a_0) = [y_1(z_0, r_{g0}, a_0) \dots y_K(z_0, r_{g0}, a_0)]^T$$

Figure 4.1: Tomographic acquisition scenario and the three-dimensional reconstruction grid. $\mathbf{y}(z_0, r_{g0}, a_0)$ is a vector containing the azimuth focused signals from K flight tracks at position (z_0, r_{g0}, a_0) of the reconstruction grid. r_g is the ground range, a is the azimuth direction, and z indicates the height within the imaged volume.

backscattering sources contribute to the measured signal. The original signal s by a particular source (back-scattering element) is

$$s = \alpha e^{i\phi}, \quad (4.2)$$

where α and ϕ are the amplitude and the phase of s , respectively. So the complex demodulated signal vector \mathbf{y} for that particular source s yields

$$\mathbf{y} = \mathbf{a}s + \mathbf{e} \quad (4.3)$$

where $\mathbf{a} = [1 e^{i\varphi_2} \dots e^{i\varphi_K}]^T$ is called the steering vector with $\varphi_m = -2k_c(r_m - r_1)$, $m = 1 \dots K$; k_c is the central wavenumber and r_m is the range distance from the backscattering element to the m -th sensor position, $\mathbf{e} = [e_1 \dots e_K]^T$ denotes uncorrelated noise. \mathbf{y} and \mathbf{e} are assumed to be zero-mean complex Gaussian distributed with covariance matrices $\mathbf{R} = \mathbf{y}\mathbf{y}^H$ and $\sigma^2\mathbf{I}$, respectively; $(\cdot)^H$ stands for the complex conjugate transpose of a matrix and \mathbf{I} is the identity matrix.

Thus, for p sources the signal vector \mathbf{y} , which represents the signal impinging on the individual across-track positions (repeat-pass flight tracks) of the antenna array synthesized in the normal direction becomes

$$\mathbf{y} = [\mathbf{a}_1 \quad \dots \quad \mathbf{a}_p] \begin{bmatrix} s_1 \\ \vdots \\ s_p \end{bmatrix} + \mathbf{e} = \mathbf{A}\mathbf{s} + \mathbf{e}. \quad (4.4)$$

4.2.1 Multilook Standard Beamforming (MLBF) and the One-Look Special Case

The TDBP tomographic focusing scheme presented in [16] can be written as follows:

$$v(z) = \sum_{m=1}^K y_m(z) \cdot e^{i2k_c(r_m(z) - r_1(z))}, \quad (4.5)$$

where $v(z)$ is the focused signal at height z (for a specific ground-range/azimuth position), K is the number of flight tracks that build the tomographic pattern, $y_m(z)$ is the azimuth-focused signal from flight track m for that specific ground-range/azimuth pixel focused to a reconstruction grid at height z . k_c is the central wavenumber and $r_m(z)$ is the closest range distance between the source at height z and the m -th flight track. There are two modifications in the notation of eq. (4.5) compared with the formulation in [16]. The first modification is that the focused data are demodulated with respect to a master track $m = 1$ and, the second, that the range distance multiplication is assumed to be included in the term $y_m(z)$.

Adopting the TDBP focusing approach to a three-dimensional reconstruction grid the back-scattering sources are found by scanning through the vertical component of the 3D grid. For this reason, all the data and steering vectors are given with respect to the coordinate system of the reconstruction grid (z, r_g, a) , however, omitting the ground range and the azimuth coordinates for the sake of readability.

Using the following two vector notations, a steering vector $\mathbf{a}(z)$:

$$\mathbf{a}(z) = [1 \ e^{i\varphi_2(z)} \ \dots \ e^{i\varphi_K(z)}]^T, \quad (4.6)$$

with $\varphi_m(z) = -2k_c(r_m(z) - r_1(z))$, $m = 1, \dots, K$; and a signal vector $\mathbf{y}(z)$:

$$\mathbf{y}(z) = [y_1(z) \ \dots \ y_K(z)]^T, \quad (4.7)$$

the focused signal $v(z)$ of eq. (4.5) can be written as:

$$v(z) = \mathbf{a}^H(z)\mathbf{y}(z) . \quad (4.8)$$

Then, the power image $\hat{P}_T(z) = |v(z)|^2$, i.e., the focused signal obtained from TDBP processing for a certain ground-range azimuth position on a horizontal layer at height z is:

$$\hat{P}_T(z) = |v(z)|^2 = |\mathbf{a}^H(z)\mathbf{y}(z)|^2 \quad (4.9)$$

$$= \mathbf{a}^H(z)\mathbf{y}(z)\mathbf{y}(z)^H\mathbf{a}(z) \quad (4.10)$$

$$= \mathbf{a}^H(z)\left(\hat{\mathbf{R}}(z)\right)_{N=1}\mathbf{a}(z) . \quad (4.11)$$

$\mathbf{y}(z)\mathbf{y}(z)^H$ corresponds to the sample covariance matrix $\hat{\mathbf{R}}(z)$ of the standard beamformer [17] in the case where the number of looks $N = 1$:

$$\hat{\mathbf{R}}(z) = \frac{1}{N} \sum_{n=1}^N \mathbf{y}(n, z)\mathbf{y}^H(n, z) \quad (4.12)$$

In other words, the power image after time-domain back-projection processing can be interpreted as the standard beamforming method for the single-look case $N = 1$.

There are several possibilities in terms of improving the focusing quality and the side lobe level of the tomographic image while maintaining the time-domain focusing scheme to a 3D reconstruction grid.

A proximate step towards a better estimation of the tomographic signal is processing the data to N looks, which are assumed to be independent and identically distributed. However, multilooking is at the expense of the resolution in ground range and azimuth. Processing multiple looks in the time-domain corresponds to the standard beamforming approach where the sample covariance matrices, which are calculated for each look, are averaged as in eq. (4.12):

$$\hat{P}_B(z) = \mathbf{a}^H(z)\hat{\mathbf{R}}(z)\mathbf{a}(z) \quad (4.13)$$

Compared to the usual formulation of beamforming [4, 17] there is one substantial difference with respect to how the focusing in normal direction is carried out: In our TDBP-based processing scheme a new covariance matrix $\hat{\mathbf{R}}(z)$ is

calculated for each horizontal layer (distinguished by the height z) of the reconstruction grid. Recall, that within our approach, the SAR data from the K different flight tracks are focused and thereby coregistered on a three dimensional reconstruction grid. So, given a back-scatterer located at height $z = z_0$ and non-linear airborne flight tracks, a target will be reconstructed best for all K flight tracks – in terms of azimuth focusing – when it is focused on the horizontal layer at the correct height $z = z_0$. And as a consequence, the azimuth-focused signals from the K flight tracks should be more similar at a particular ground-range azimuth coordinate at the correct height $z = z_0$ than for all other heights $z \neq z_0$. This is the motivation to calculate the sample covariance matrix $\hat{\mathbf{R}}(z)$ separately for each height z and this is also, besides the different azimuth focusing technique, the difference to the deramp and FFT (SPECAN) beamforming approach proposed by Reigber et al. [2].

4.2.2 Multiple Signal Classification (MUSIC)

The key idea behind the MUSIC algorithm [8] is to provide an estimate of the location of the p sources (back-scattering elements) based on a separation of the K -dimensional data space (4.17) into two subspaces, a signal space \mathbf{S} and a noise space \mathbf{G} , which are derived from the eigendecomposition of the sample covariance matrix \mathbf{R} .

In the following, the MUSIC pseudospectrum estimator is derived from the signal model given in (4.2) – (4.4) which yields the following covariance model

$$\mathbf{R} = E \{ \mathbf{y}\mathbf{y}^H \} = \mathbf{A}\mathbf{P}\mathbf{A}^H + \sigma^2\mathbf{I}; \quad \mathbf{P} = \begin{bmatrix} \alpha_1^2 & & 0 \\ & \ddots & \\ 0 & & \alpha_K^2 \end{bmatrix} \quad (4.14)$$

The matrix $\mathbf{A}\mathbf{P}\mathbf{A}^H$ has rank p (number of sources) and therefore $\mathbf{A}\mathbf{P}\mathbf{A}^H$ has p positive eigenvalues and the remaining $(K - p)$ eigenvalues are zero. After calculating the eigenvalue decomposition of the covariance matrix \mathbf{R}

$$\mathbf{R} = \mathbf{U}\mathbf{T}\mathbf{U}^H, \quad (4.15)$$

where $\mathbf{U} = [\mathbf{u}_1 \dots \mathbf{u}_K]$ contains the eigenvectors corresponding to the eigenvalues

contained in the diagonal matrix $\mathbf{\Gamma}$,

$$\mathbf{\Gamma} = \begin{bmatrix} \gamma_1 & 0 & \dots & & \dots & 0 \\ 0 & \ddots & 0 & \dots & & \vdots \\ \vdots & 0 & \gamma_p & 0 & & \\ & & 0 & \gamma_{p+1} & 0 & \vdots \\ \vdots & & & 0 & \ddots & 0 \\ 0 & \dots & & \dots & 0 & \gamma_K \end{bmatrix} \quad (4.16)$$

with the eigenvalues $\gamma_m = \gamma_m^{APA^H} + \sigma^2$ of \mathbf{R} sorted in non-increasing order the following relationship holds [17]

$$\begin{cases} \gamma_m > \sigma^2 & \text{for } m = 1, \dots, p \\ \gamma_m = \sigma^2 & \text{for } m = p + 1, \dots, K \end{cases} \quad (4.17)$$

The signal space is spanned by the matrix

$$\mathbf{S} = [\mathbf{u}_1 \dots \mathbf{u}_p] \quad (4.18)$$

where $\mathbf{u}_m, m = 1 \dots p$ are the orthonormal eigenvectors corresponding to the p largest eigen-values $\gamma_1 \dots \gamma_p$. Analogously, the noise space is spanned by the matrix

$$\mathbf{G} = [\mathbf{u}_{p+1} \dots \mathbf{u}_K]. \quad (4.19)$$

Then, the following relationships hold

$$\mathbf{U} = [\mathbf{S} \ \mathbf{G}], \mathbf{S}^H \mathbf{S} = \mathbf{I}, \mathbf{G}^H \mathbf{G} = \mathbf{I}, \quad (4.20)$$

and, in particular, the two sub-spaces spanned by \mathbf{S} and \mathbf{G} are orthogonal:

$$\mathbf{S}^H \mathbf{G} = \mathbf{0}, \quad (4.21)$$

and since the eigenvectors \mathbf{u}_m are orthonormal

$$\mathbf{S}\mathbf{S}^H + \mathbf{G}\mathbf{G}^H = \mathbf{I}. \quad (4.22)$$

Right-hand multiplying \mathbf{G} to both sides of (4.15) and using $\mathbf{U} = [\mathbf{S} \ \mathbf{G}]$ yields

$$\mathbf{R}\mathbf{G} = \mathbf{U}\mathbf{U}^H\mathbf{G} \quad (4.23)$$

$$= [\mathbf{S} \ \mathbf{G}] \mathbf{\Gamma} \begin{bmatrix} \mathbf{S}^H \\ \mathbf{G}^H \end{bmatrix} \mathbf{G} \quad (4.24)$$

and using (4.20) and (4.21)

$$= [\mathbf{S} \ \mathbf{G}] \mathbf{\Gamma} \begin{bmatrix} \mathbf{0} \\ \mathbf{I} \end{bmatrix} \quad (4.25)$$

$$= [\mathbf{S} \ \mathbf{G}] \begin{bmatrix} \mathbf{0} & & \\ \gamma_{p+1} & \dots & 0 \\ & & \gamma_K \end{bmatrix} \quad (4.26)$$

$$= \mathbf{G} \begin{bmatrix} \gamma_{p+1} & \dots & 0 \\ & \dots & \\ 0 & & \gamma_K \end{bmatrix} = \sigma^2 \mathbf{G}. \quad (4.27)$$

The last equation in (4.27) holds due to (4.17). Right-hand multiplying \mathbf{G} to both sides of (4.14) yields

$$\mathbf{R}\mathbf{G} = \mathbf{A}\mathbf{P}\mathbf{A}^H\mathbf{G} + \sigma^2\mathbf{G}. \quad (4.28)$$

Combining (4.23), (4.27) and (4.28) yields

$$\mathbf{A}\mathbf{P}\mathbf{A}^H\mathbf{G} + \sigma^2\mathbf{G} = \sigma^2\mathbf{G} \quad (4.29)$$

$$\mathbf{A}\mathbf{P}\mathbf{A}^H\mathbf{G} = \mathbf{0}, \quad (4.30)$$

and since the matrix $\mathbf{A}\mathbf{P}$ has full column rank K

$$\mathbf{A}^H\mathbf{G} = \mathbf{0}. \quad (4.31)$$

Equation (4.31) is satisfied if

$$\mathbf{a}^H\mathbf{G}\mathbf{G}^H\mathbf{a} = 0 \quad (4.32)$$

holds for all p source locations. In practice, the p back-scattering elements are found at the p dominant peaks of the following function

$$P_{MU} = \frac{1}{\mathbf{a}^H\mathbf{G}\mathbf{G}^H\mathbf{a}}, \quad (4.33)$$

by scanning through an array of discrete potential locations. P_{MU} is also called the pseudo-powerspectrum.

The MUSIC algorithm [8] is a model based spectral estimator in the sense that the number of sources must be known. Thus, in practice, the *unknown* number of sources have to be determined. In general, the rank of the sample covariance matrix, determined based on a SVD and an appropriate threshold, is an estimator for the number of sources that span the signal space. In this paper a heuristic approach also applied by [11] is followed in order to choose the number of sources that are displayed: only the eigenvalues that are greater than ten percent of the largest eigenvalue are considered as back-scattering sources that form the signal subspace.

The individual steps to compute the MUSIC-based tomograms are:

1. Calculate the sample covariance matrix $\hat{\mathbf{R}}(z)$ at each location.
2. Calculate the eigen-decomposition of the sample covariance matrix

$$\hat{\mathbf{R}} = \mathbf{U}\mathbf{\Gamma}\mathbf{U}^H \quad (4.34)$$

3. Permute the matrices such that the eigenvalues in $\mathbf{\Gamma}$ are sorted in non-increasing order: $\gamma_1 \geq \gamma_2 \geq \dots \geq \gamma_K$; the matrix of eigenvectors \mathbf{U} is adjusted accordingly.
4. Set a threshold for the eigenvalue that separates the signal- and the noise-subspace, respectively.
5. Estimate the locations of the sources in the vertical direction by scanning through the reconstruction grid.

$$\hat{P}_{MU}(z) = \frac{1}{\mathbf{a}^H(z)\mathbf{G}(z)\mathbf{G}^H(z)\mathbf{a}(z)} \quad (4.35)$$

4.2.3 Robust Capon Beamforming (RCB)

In a similar way, Capon beamforming can be applied within the time-domain 3D focusing framework. After matrix inversion of the sample covariance matrix $\hat{\mathbf{R}}(z)$ the Capon estimated power \hat{P}_C is obtained for each layer on height z :

$$\hat{P}_C(z) = \frac{1}{\mathbf{a}^H(z)\hat{\mathbf{R}}(z)^{-1}\mathbf{a}(z)} \quad (4.36)$$

Lombardini et al. [4] have proposed to include diagonal loading when building the sample covariance estimate $\hat{\mathbf{R}}(\mathbf{z})$.

Beamforming techniques such as MUSIC and the Capon beamformer provide superresolution, a property which allows for still achieving a high resolution of the tomographic image in spite of using only a shorter synthetic aperture — or, equivalently in case of beamforming in the normal direction, a lower number of flight tracks.

While the MUSIC algorithm possesses an inherent robustness against steering vector errors, as has been shown in [9], in the case of the Capon beamformer, an improved resolution and a better reduction of the side lobes can either be obtained if the steering vector is calibrated perfectly, or, if the Capon beamformer is extended in such a way that the unknown true steering vector \mathbf{a} is estimated along with the power P_C .

Li et al. [18] and Stoica et al. [10] have proposed such a robust version of the Capon beamformer that can still be solved in an efficient manner. Their approach has been adopted in this paper for robust Capon beamforming and shall be explained here in some detail. The main idea behind this robust technique is, that the true steering vector \mathbf{a} is unknown, but the additional information is given that \mathbf{a} belongs to the following uncertainty ellipsoid

$$(\mathbf{a} - \bar{\mathbf{a}})^H \mathbf{C}^{-1} (\mathbf{a} - \bar{\mathbf{a}}) \leq 1, \quad (4.37)$$

where \mathbf{a} is the actual steering vector to be estimated and $\bar{\mathbf{a}}$ is the measured steering vector. The robust Capon beamformer is found by solving the following expression [18]

$$\max_{\mathbf{a}, P_C} P_C \quad \text{subject to} \quad \mathbf{R} - P_C \mathbf{a} \mathbf{a}^H \quad (4.38)$$

$$(\mathbf{a} - \bar{\mathbf{a}})^H \mathbf{C}^{-1} (\mathbf{a} - \bar{\mathbf{a}}) \leq 1. \quad (4.39)$$

Using (1) the fact that $P_C = \frac{1}{\mathbf{a}^H \mathbf{R}^{-1} \mathbf{a}}$ maximizing P_C is equivalent to minimizing $\mathbf{a}^H \mathbf{R}^{-1} \mathbf{a}$, and (2) assuming that $\mathbf{a} = 0$ is not part of the uncertainty ellipsoid — i.e. the solution to \mathbf{a} will lie on the boundary of the ellipsoid — and further (3) as there is not sufficient a priori information about the variance of the individual components of the steering vector the covariance matrix \mathbf{C} is set to $\mathbf{C} = \epsilon \mathbf{I}$ the estimation problem reduces to the following quadratic problem with a quadratic equality constraint

$$\min_{\mathbf{a}} \mathbf{a}^H \mathbf{R}^{-1} \mathbf{a} \quad \text{subject to} \quad \|\mathbf{a} - \bar{\mathbf{a}}\|^2 = \epsilon. \quad (4.40)$$

The expression (4.40) can then be solved efficiently by using the Lagrange multiplier approach

$$F(\mathbf{a}, \lambda) = \mathbf{a}^H \mathbf{R}^{-1} \mathbf{a} + \lambda \cdot \left(\|\mathbf{a} - \bar{\mathbf{a}}\|^2 - \epsilon \right). \quad (4.41)$$

Taking the derivative of $F(\mathbf{a}, \lambda)$ with respect to \mathbf{a} and setting $\frac{\delta F(\mathbf{a}, \lambda)}{\delta \mathbf{a}} = 0$ yields

$$\mathbf{R}^{-1} \mathbf{a} + \lambda \cdot (\mathbf{a} - \bar{\mathbf{a}}) = 0, \quad (4.42)$$

and eventually

$$\mathbf{a} = \left(\frac{\mathbf{R}^{-1}}{\lambda} + \mathbf{I} \right)^{-1} \bar{\mathbf{a}}. \quad (4.43)$$

Equivalently, $\frac{\delta F(\mathbf{a}, \lambda)}{\delta \lambda} = 0$ yields the original quadratic equality constraint:

$$\|\mathbf{a} - \bar{\mathbf{a}}\|^2 - \epsilon = 0. \quad (4.44)$$

Using the Woodbury matrix identity

$$(\mathbf{A} + \mathbf{UCV})^{-1} = \mathbf{A}^{-1} - \mathbf{A}^{-1} \mathbf{U} (\mathbf{C}^{-1} + \mathbf{VA}^{-1} \mathbf{U})^{-1} \mathbf{VA}^{-1} \quad (4.45)$$

and assuming $\mathbf{U} = \mathbf{I}$, $\mathbf{V} = \mathbf{I}$, $\mathbf{A} = \mathbf{I}$, and $\mathbf{C} = 1/\lambda \cdot \mathbf{R}^{-1}$ (4.45) becomes

$$\left(\frac{\mathbf{R}^{-1}}{\lambda} + \mathbf{I} \right)^{-1} = \mathbf{I} - (\lambda \mathbf{R} + \mathbf{I})^{-1} \quad (4.46)$$

and thus the term in (4.43) can be written as

$$\mathbf{a} = \bar{\mathbf{a}} - (\lambda \mathbf{R} + \mathbf{I})^{-1} \bar{\mathbf{a}}. \quad (4.47)$$

Using (4.47) in (4.43) and (4.43) in (4.44) yields

$$\|(\mathbf{I} + \lambda \mathbf{R})^{-1} \bar{\mathbf{a}}\|^2 = \epsilon. \quad (4.48)$$

The eigenvalue decomposition of \mathbf{R} is

$$\mathbf{R} = \mathbf{U} \mathbf{\Gamma} \mathbf{U}^H \quad (4.49)$$

where $\mathbf{U} = [\mathbf{u}_1 \dots \mathbf{u}_K]$ is the matrix of eigenvectors \mathbf{u}_m , $m = 1 \dots K$, and the diagonal elements of the diagonal matrix $\mathbf{\Gamma}$ contain the corresponding eigenvalues $\gamma_1 \geq \gamma_2 \geq \dots \geq \gamma_K$. Additionally, setting

$$\mathbf{b} = \mathbf{U} \bar{\mathbf{a}} \quad (4.50)$$

the left-hand side of (4.48) can be rewritten as

$$\|(\mathbf{I} + \lambda \mathbf{R})^{-1} \bar{\mathbf{a}}\|^2 = \bar{\mathbf{a}}^H [\mathbf{U}(\mathbf{I} + \lambda \mathbf{\Gamma})\mathbf{U}^H]^{-2} \bar{\mathbf{a}} \quad (4.51)$$

$$= \bar{\mathbf{a}}^H \mathbf{U}(\mathbf{I} + \lambda \mathbf{\Gamma})^{-2} \mathbf{U}^H \bar{\mathbf{a}} \quad (4.52)$$

$$= \mathbf{b}^H (\mathbf{I} + \lambda \mathbf{\Gamma})^{-2} \mathbf{b} \quad (4.53)$$

$$= \sum_{m=1}^K \frac{|b_m|^2}{(1 + \lambda \gamma_m)^2} = \epsilon. \quad (4.54)$$

It can be shown [17] that there is a unique solution to (4.54) within the interval $[\lambda_{low}, \lambda_{up}]$, where

$$\lambda_{low} = \frac{\|\bar{\mathbf{a}}\| - \sqrt{\epsilon}}{\gamma_1 \sqrt{\epsilon}}, \quad (4.55)$$

and

$$\lambda_{up} = \frac{\|\bar{\mathbf{a}}\| - \sqrt{\epsilon}}{\gamma_K \sqrt{\epsilon}}. \quad (4.56)$$

Eventually, the computation of the robust Capon beamformer consists of the following steps:

1. Determine the eigen-decomposition of the sample covariance matrix \mathbf{R}

$$\mathbf{R} = \mathbf{U} \mathbf{\Gamma} \mathbf{U}^H \quad (4.57)$$

and set

$$\mathbf{b} = \mathbf{U}^H \bar{\mathbf{a}}. \quad (4.58)$$

2. Solve

$$\sum_{m=1}^K \frac{|b_m|^2}{(1 + \lambda \gamma_m)^2} = \epsilon \quad (4.59)$$

for the Lagrange multiplier λ , given the fact, that there is a unique solution in the interval $[\lambda_{low}, \lambda_{up}]$.

3. Calculate an estimate of the unknown steering vector \mathbf{a}

$$\mathbf{a} = \bar{\mathbf{a}} - \mathbf{U}(\mathbf{I} + \lambda \mathbf{\Gamma})^{-1} \mathbf{b}. \quad (4.60)$$

4. Using the knowledge that the true steering vector satisfies the condition $\mathbf{a}^H \mathbf{a} = K$ the estimated power finally yields [17]

$$P_C = \frac{\mathbf{a}^H \mathbf{a}}{K \mathbf{a}^H \mathbf{U} \mathbf{\Gamma}^{-1} \mathbf{U}^H \mathbf{a}}. \quad (4.61)$$

The term $\frac{\mathbf{a}^H \mathbf{a}}{K}$ is necessary to get rid of a scaling ambiguity in the signal covariance term $P_C \mathbf{a} \mathbf{a}^H$ of (4.38) in the sense that each pair $P_C/\mu, \sqrt{\mu} \mathbf{a}$, for any $\mu > 0$, yields the same covariance term [17].

4.2.4 A Few Comments on the Processing Approach

Since for MLBF, RCB, and MUSIC beamforming the sample covariance matrix $\hat{\mathbf{R}}(\mathbf{z})$ has actually to be calculated the data are demodulated after the TDBP azimuth focusing to the various layers. It is further necessary to keep track of the range distances at the closest point of approach used for demodulation. They are needed to build the appropriate steering vectors.

Lombardini et al. [4], for instance, applied Capon beamforming for tomographic focusing after having processed the data by the extended chirp scaling algorithm and after having coregistered the focused data sets from the K flight tracks to a common geometry. They calculated *one* sample covariance matrix $\hat{\mathbf{R}}$ for a certain pixel in this coregistered range-azimuth geometry, therefore, $\hat{\mathbf{R}}$ does not depend on the height z . In contrast, within the approach presented here, the data are processed onto several (horizontal) layers and, in particular, a sample covariance matrix $\hat{\mathbf{R}}(z)$ is calculated at each point on the reconstruction grid *for each layer* on height z . So, a data vector $\mathbf{y}_z(n, z)$ is set up for each height z and for each look. $\hat{\mathbf{R}}(z)$ is then calculated from the demodulated K data sets on a particular height z . The high geometric fidelity that is maintained by following this time-domain approach has the potential to lead to an improved focusing quality, and eventually, a higher level of detail of the tomographic images.

The TDBP processing of the data to the reconstruction grid was performed as described in [14].

4.2.5 A Note On Baseline Calibration

In the following, the processing approach used for baseline calibration is given. Although each data track is processed in the time domain based on the original

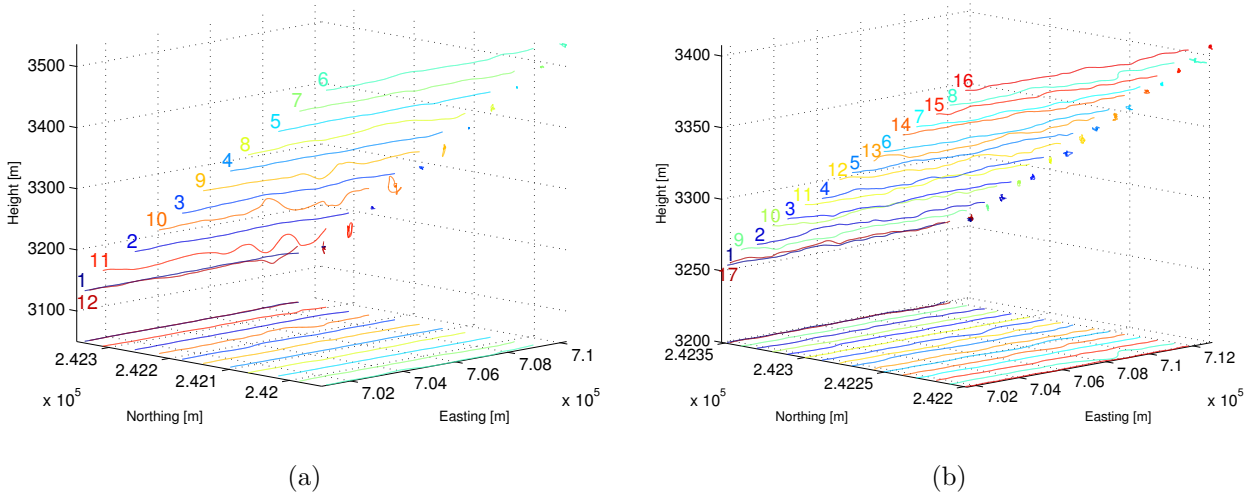


Figure 4.2: Tomographic acquisition patterns: (a) P-band, 11 MB tracks + 1 control track; (b) L-band, 16 MB tracks + 1 control track. The flight directions are from east to west and the sensors are left-looking. In addition to the actual flight tracks, their projections to the horizontal plane and to the northing-height plane are depicted.

flight path, the data is reassigned to a common azimuth direction for all flight tracks as detailed below:

1. Calculation of a linear approximation of each flight track by fitting the linear flight track model to the measured antenna positions in 3D space in a total least squares sense (also termed orthogonal regression).
2. A common azimuth direction is then determined by averaging the direction vectors of the individual linearized flight tracks.
3. Based on the common azimuth direction the 3D reconstruction grid is built in an azimuth/ground-range/height layout [see Fig. 4.1, p. 90].
4. Time-domain back-projection processing of all data sets using the *original, measured antenna positions* onto the 3D reconstruction grid. For each data point the range distance r_{DC} corresponding to the Doppler centroid frequency f_{DC} is stored.
5. Then, the 2D-focused SAR data sets are reassigned to the common azimuth direction to ensure a unified geometry and zero Doppler annotation before tomographic focusing. To this end, a phase multiply $e^{i4\pi/\lambda(r_{DC}-r_{PCA})}$ is applied to each data point on the reconstruction grid, where r_{DC} is the range distance corresponding to the Doppler centroid frequency f_{DC} and where r_{PCA} is the range distance at the point of closest approach (PCA).

6. Eventually, the remaining global phase offsets between the individual tracks of the tomographic data set are removed.

4.3 Description of the Experiment

4.3.1 Experimental Set-Up for SAR Tomography

Two fully polarimetric MB data sets—an L-band and a P-band data set—of a partially forested test site in Switzerland have been acquired by the German Aerospace Center’s E-SAR system, in September 2006. In Fig. 4.2(a) and Fig. 4.2(b), respectively, the geometric configurations of the actual flight tracks for both tomographic data sets, P- as well as L-band, are shown. In addition to the flight tracks their projections to the horizontal plane and to the northing-height plane are also depicted. Both MB data takes were completed by a control track which has the same nominal flight geometry as the first track.

In both cases, the tracks of the tomographic pattern were flown in an interleaved manner. The flight directions are from east to west and both sensors are left-looking.

	P-band	L-band
Carrier frequency	350 MHz	1.3 GHz
Chirp bandwidth	70 MHz	94 MHz
Sampling rate	100 MHz	100 MHz
PRF	500 Hz	400 Hz
Ground speed	90 m/s	90 m/s
No. of data tracks	11+1	16+1
Nominal track spacing d_n	57 m	14 m
Horizontal baselines	40 m	10 m
Vertical baselines	40 m	10 m
Synthetic aperture in normal direction L	570 m	210 m
Nominal resolution in normal direction δ_n	3 m	2 m
Approx. unambiguous height H	30 m	30 m

Table 4.1: E-SAR system specifications and nominal parameters of the tomographic acquisition patterns for both multibaseline data sets at P-band and L-band.

The P-band MB data set was acquired within one air mission, the maximal time span between the first and the last track being approximately 2 h. The large number of baselines of the L-band MB data set required two separate missions, flown on the same day which resulted in a maximal time span of approximately 4.5 h between the first track of the first mission and the ultimate track of the second mission.

In Table 4.1 the sensor specifications and a summary of the parameters which characterize the tomographic data sets are given. Note that the chirp bandwidth had to be reduced to 70MHz for the P-band sensor to prevent interference of the radar signal with existing RF communication services within the band 390-395 MHz. The nominal chirp bandwidth would be 94 MHz for both L- and P-band. In addition, a total number of eight corner reflectors were deployed within the area and their position has been measured by carrier-phase differential GPS.

4.3.2 Cross-Validation Data

An accurate digital elevation model (DEM) of 1m x 1m pixel spacing derived from airborne laser scanning (ALS) is used (Falcon II, Toposys GmbH) for a comparison of the ground level and a digital surface model (DSM) acquired by the same sensor is also at hand indicating the vegetation cover.

The airborne laser scanning data were acquired in spring of 2003. It has to be assumed that the deciduous trees were mostly transparent to the laser signal and, therefore, do not appear in the ALS-derived DSM—on the other hand, the forest within the test site is dominated by evergreen coniferous trees (about 80%). Nonetheless, the DSM has been manually updated using two additional data sets: another ALS-derived data set from summer 2002 was utilized in order to manually correct for the missing deciduous trees, and airborne ortho-images acquired in the summer of 2006 were used to manually mask additional clear-cuts.

4.4 Results

4.4.1 Analysis of the Impulse Response

In the following, the basis for a comparison of the focusing quality in the normal direction is given by means of an analysis of the different impulse responses

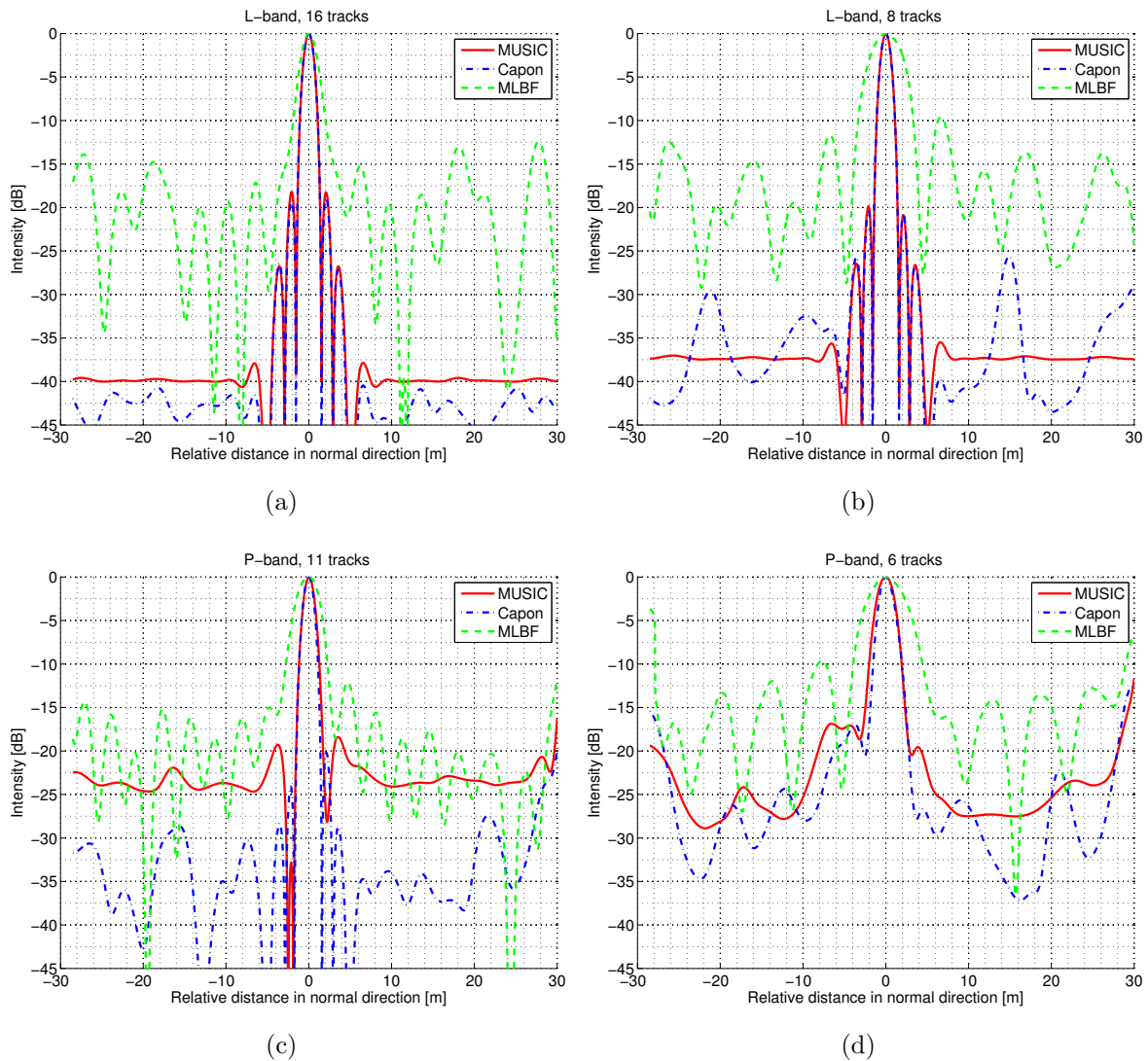


Figure 4.3: Impulse responses obtained from an in-scene trihedral reflector using three different approaches to focus the MB data in the normal direction: multilook standard beamforming, robust Capon beamforming, and MUSIC beamforming. (a) L-band, full synthetic aperture (16 adjacent tracks), (b) L-band, reduced synthetic aperture (8 adjacent tracks), (c) P-band, full synthetic aperture (11 adjacent tracks). (d) P-band, reduced synthetic aperture (6 adjacent tracks).

obtained by varying the parameters listed subsequently:

1. Focusing technique: MLBF, RCB, and MUSIC beamforming.
2. Full and reduced (half) length of the synthetic aperture in the normal direction.
3. Frequency: L-band and P-band MB data.

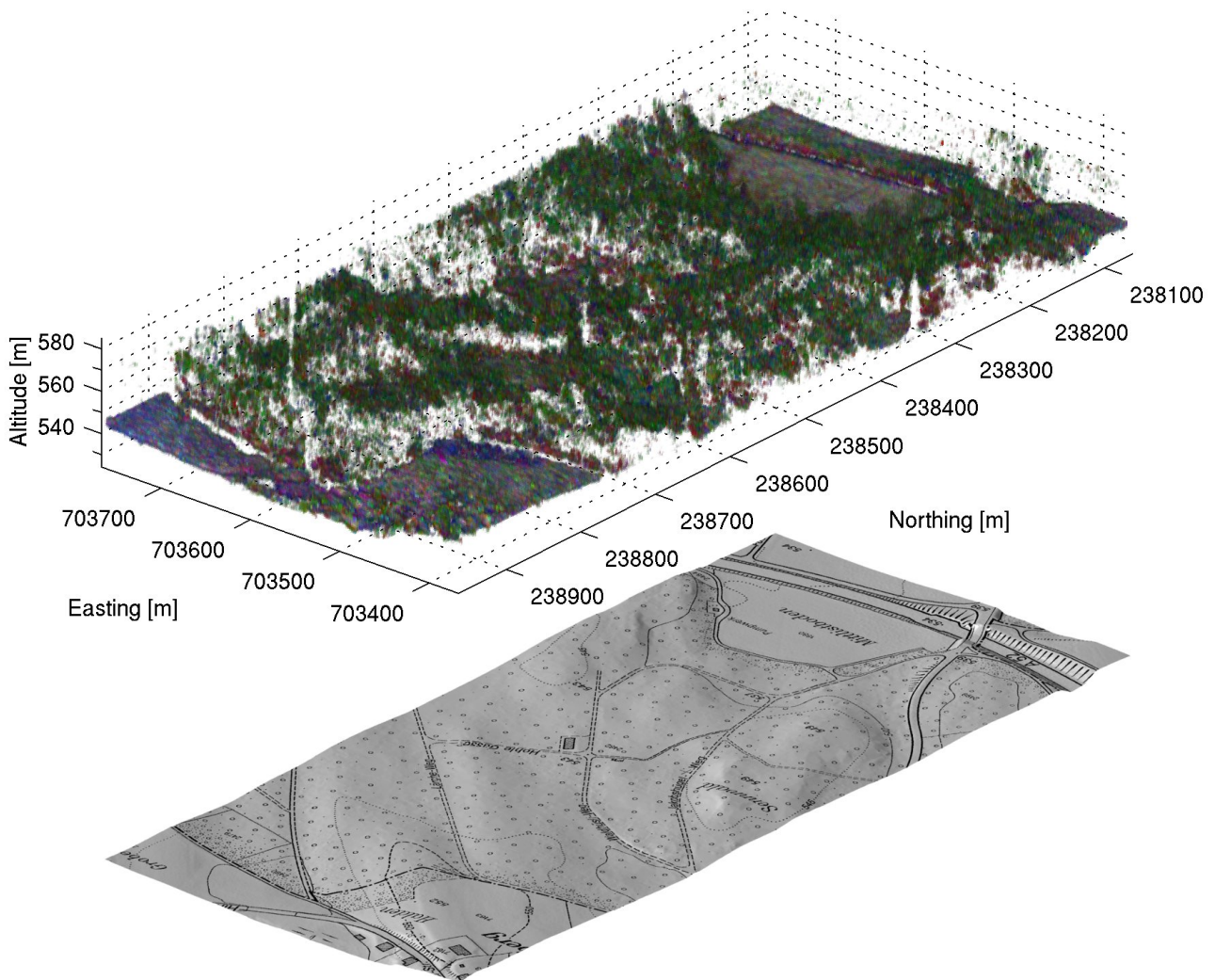


Figure 4.4: Tomographic image (3D voxel plot) of a partially forested area obtained from combined TDBP and MUSIC beamforming of polarimetric airborne repeat-pass multibaseline SAR data at L-band. For visualization purposes each channel has been scaled individually. Red (HH), green (HV), blue (VV). Low intensity = high transparency of the voxel. Beneath, a 1:5000-scale digital map of the same area, warped on a DEM obtained by ALS, is shown to give a comparative picture of the outer boundaries of the forested area, the underlying terrain, and additional features, such as forest roads, for instance. Map reproduced by permission of the Cantonal Office of Spatial Planning and Surveying, Zurich (20100019).

The respective impulse responses as a function of the relative distance in the normal direction are shown in Fig. 4.3. The impulse responses have been measured based on an in-scene trihedral reflector ($\text{RCS}_{\text{dB}} = 22.13 \text{ dB} \cdot \text{m}^2$ at L-band, $\text{RCS}_{\text{dB}} = 10.74 \text{ dB} \cdot \text{m}^2$ at P-band).

4.4.2 Tomographic Images

Fig. 4.4 depicts a three-dimensional voxel plot representation of the partially forested area under study obtained from combined TDBP and MUSIC beamforming of the polarimetric MB SAR data at L-band using the full synthetic aperture in normal direction. The polarimetric channels HH (red), HV (green), and VV (blue) are given in an RGB color scheme scaled by a transparency value to represent the signal intensity. A very detailed picture of the forest is obtained as can be readily verified qualitatively when comparing the tomography data with the detailed map, below in Fig. 4.4. Even details, such as small forest roads, are well visible as gaps in the canopy cover.

In Fig. 4.5, samples of a vertical tomographic slice through the 3D volume are given as they are obtained from processing the L-band MB data using the three different approaches MLBF, RCB and MUSIC beamforming. The vertical profiles are in south-northern direction. On the left-hand side (a), the tomographic slices are depicted for MLBF (top), RCB (middle), and MUSIC (bottom); the greyed areas indicate the ambiguous target regions. On the right-hand side (b), the tomographic images being one meter offset in easting direction from the ones in (a) are shown overlaid by the DEM (solid red line) and the DSM (solid green line) from ALS. This enables a qualitative discussion about the imaging capabilities and the fidelity relative to the laser scanning data as well as advantages and disadvantages of the processing approaches. A detailed analysis of the fully polarimetric tomographic data products and comparisons with respect to cross-reference and ground truth data is out of the scope of this paper, which focuses on the actual imaging of the MB data, and will, therefore, be given in a separate paper. Analogously as in Fig. 4.5, the vertical tomographic slices of the focused P-band MB data are given in Fig. 4.6.

4.5 Discussion

4.5.1 Analysis of the Impulse Response

Compared to MLBF both superresolution techniques, RCB and MUSIC beamforming, deliver a much improved suppression of the side lobes in all cases, the full and the reduced synthetic aperture as well as at both frequencies. Further, RCB and MUSIC are able to maintain a high resolution also for the reduced

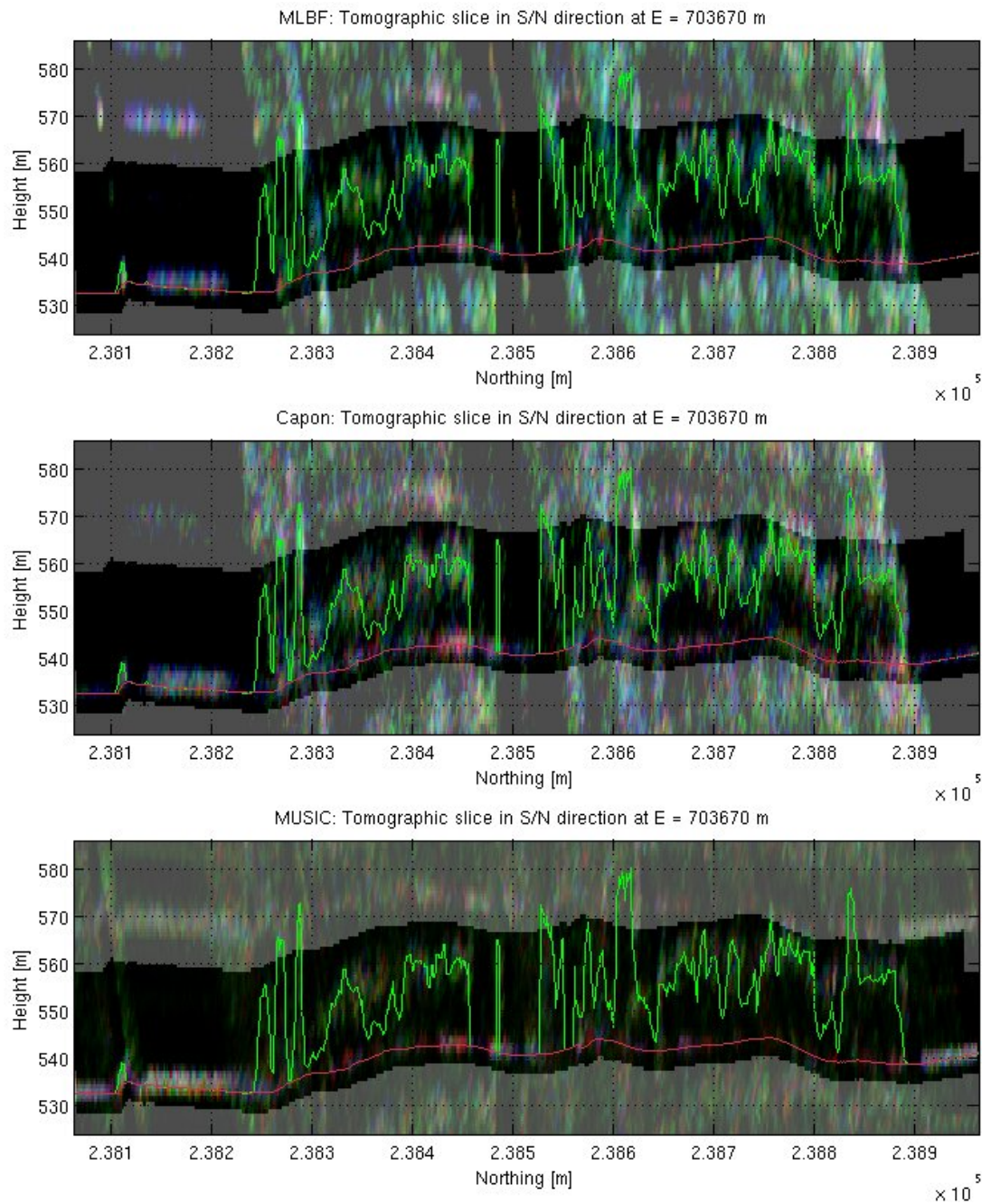


Figure 4.5: Vertical slices through a 3D volume of a forested area obtained from a polarimetric multibaseline L-Band data set using all (16) data tracks. Red (HH), green (HV), blue (VV). Each channel has been scaled individually. Greyed areas indicate ambiguous target regions. The tomographic slices run in south-northern direction (at easting coordinate $E = 703670$ m) and are overlaid by the DEM (solid red line) and the DSM (solid green line) from ALS. Top: MLBF, middle: RCB, bottom: MUSIC.

synthetic aperture, whereas for MLBF the resolution degrades considerably.

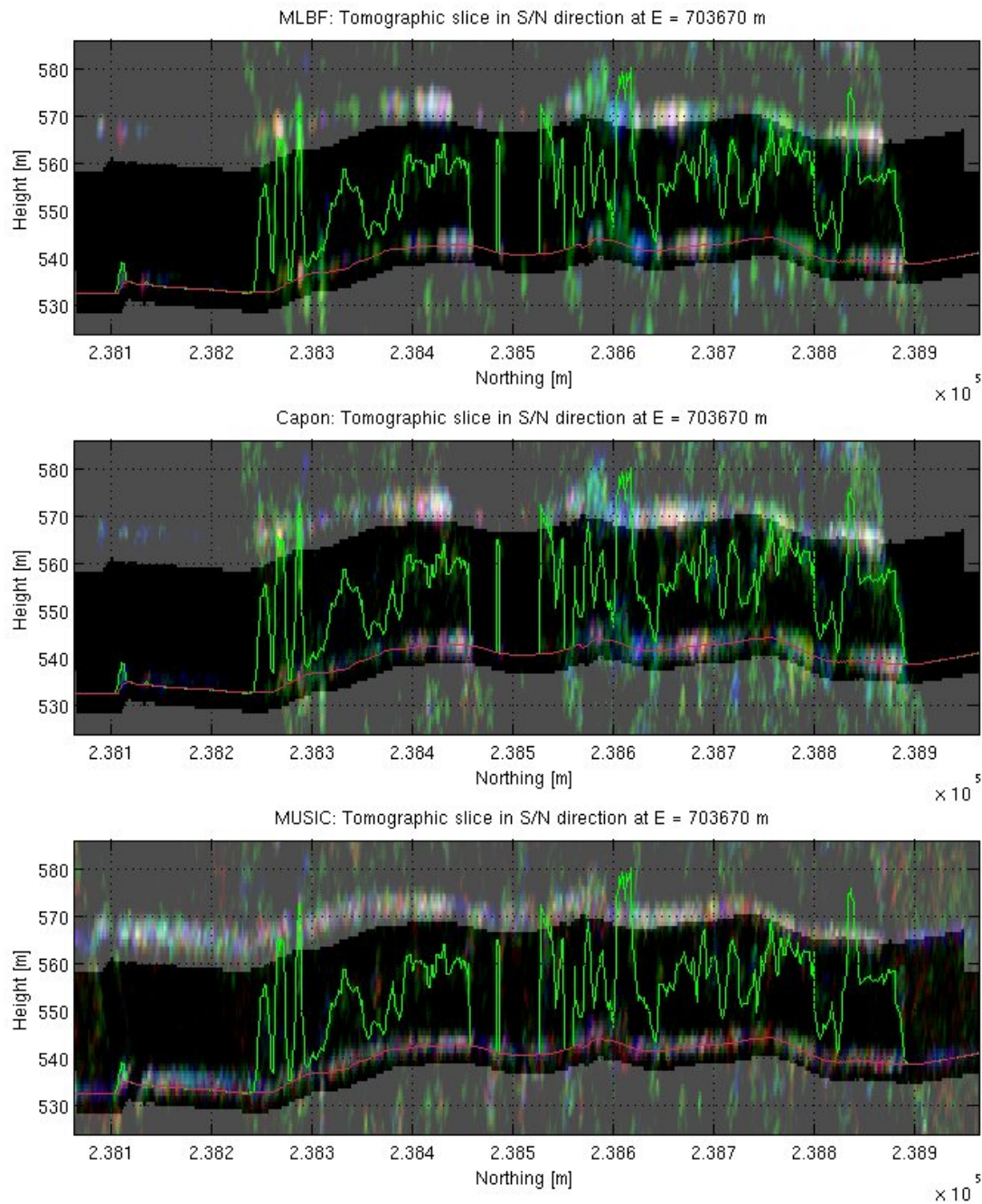


Figure 4.6: Vertical slices through a 3D volume of a forested area obtained from a polarimetric multibaseline P-Band data set using all (11) data tracks. Red (HH), green (HV), blue (VV). Each channel has been scaled individually. Greyed areas indicate ambiguous target regions. The tomographic slices run in south-northern direction (at easting coordinate $E = 703670$ m) and are overlaid by the DEM (solid red line) and the DSM (solid green line) from ALS. Top: MLBF, middle: RCB, bottom: MUSIC.

Using the superresolution techniques the side lobes are low (this is also visible in

the vertical profile plot when examining the non-forested areas). The remaining calibration errors in the steering vectors can be mitigated by using RCB or MUSIC, which are both robust against miscalibration, and they therefore leave the focusing quality unaffected.

4.5.2 Tomographic Images

A tomographic 3D voxel image of a forested area at an unprecedented level of detail is obtained. For instance, gaps in the canopy due to features like small forest roads of a width of a few meters only are clearly visible at the given ground range azimuth resolution. Other techniques that have been proposed in literature to characterize forest by either SAR tomography or PolInSAR approaches work with an averaging at a completely different scale (Tebaldini [12], for instance, used a 50m x 50m averaging window, corresponding to about 350 independent looks, whereas 20 looks have been applied in this work.

Firstly, it can be stated that at L-band both, the canopy layer and the ground level are detected. Also at P-band the canopy and the ground beneath are well separated. However, back-scattering from the crown layer occurs only sparsely compared to the L-band data. On the other hand, the ground level is virtually continuously detected at P-band indicating a high level of foliage-penetration.

Around the northing coordinate 236300m a strong back-scattering contribution from the canopy of a large tree is observed in all images, at L-band and P-band. At the respective position the DSM clearly indicates that a tree, which exceeds the unambiguous region, is the source of this contribution. While the back-scattering from the crown is well visible, this example also demonstrates the limits of the experimental setup: Since the tree height exceeds the unambiguous height for this particular case the back-scattering contribution from the crown is ambiguously appearing again within the unambiguous imaging region and can therefore be mixed with other, “true” targets.

The high level of detail of the tomographic images becomes obvious in a situation where a single tree is standing in a clear cut area (between northing coordinates 238480m and 238490m). The tree is indicated by the ALS DSM and all tomographic MB SAR images at both frequency bands. The SAR images show strong back-scattering behavior within the crown and at the ground level.

The regions outside the forested area confirm the observation made by means

of the point target analysis that the focusing quality is generally good for all three methods—given their different side lobe level by default. Non surprisingly, MLBF is the method that is the most susceptible to high anomalous side lobes as can be observed in the tomographic images at locations where strong targets are present.

A drawback in all 3D images is certainly the given unambiguous height of 30m in normal direction, which leads to incorrect imaging of large trees: the tree top is mixed with the response from the ground or even the lower part of the canopy. This is a generic problem that is due to the mission design which is a trade-off between a number of factors. Most importantly, the idea was to obtain a useful resolution in normal direction also for the MLBF case, given a limited number of flight tracks.

4.6 Conclusion

A time-domain based tomographic SAR imaging method has been presented that encompasses multilook standard beamforming, robust Capon beamforming and MUSIC beamforming.

An example of a MUSIC-focused L-band MB data set, given as a three-dimensional voxel plot, demonstrates the unprecedented level of detail that is achieved compared to other methods described in literature, so far, where a lot of detail in the range azimuth domain is lost due to excessive multilooking. In our example, features such as gaps in the canopy can be observed at locations where the forest is intersected by narrow roads.

With the help of an exemplary vertical profile through the 3D volume provided for both frequencies, L-band and P-band, a qualitative impression of the high level of detail is obtained, whereas the good focusing performance is illustrated by means of a quantitative analysis of the impulse responses obtained from the different processing methods and configurations. For a localization of the main scattering sources, e.g., for ground detection at P-band, one of the superresolution techniques can be applied even with a reduced synthetic aperture in normal direction.

For the first time, high resolution tomographic SAR images of the same forested area have been presented at both, L-band and P-band. While the emphasis of this paper has been on the description of a new high resolution processing

scheme for SAR tomography and its evaluation regarding the focusing performance as well as regarding the overall resolution and level of detail that is accomplished, in a separate paper, a detailed analysis of the back-scattering behavior based on the fully-polarimetric data of both, the L-band and the P-band data set will be given.

References

- [1] S. R. Cloude and K. P. Papathanassiou, "Polarimetric SAR interferometry," *IEEE Trans. Geosci. Remote Sens.*, vol. 36, no. 5, pp. 1551–1565, Sep. 1998.
- [2] A. Reigber and A. Moreira, "First demonstration of airborne SAR tomography using multibaseline L-band data," *IEEE Trans. Geosci. Remote Sens.*, vol. 38, no. 5, pp. 2142–2152, 2000.
- [3] M. Nannini and R. Scheiber, "A time domain beamforming algorithm for SAR tomography," in *Proc. of EUSAR 2006 - 6th European Conference on Synthetic Aperture Radar*, 2006.
- [4] F. Lombardini and A. Reigber, "Adaptive spectral estimation for multi-baseline SAR tomography with airborne L-band data," in *Proc. IEEE Int. Geosci. and Remote Sens. Symp.*, vol. 3, 2003, pp. 2014–2016.
- [5] G. Fornaro, F. Serafino, and F. Soldovieri, "Three-dimensional focusing with multipass SAR data," *IEEE Trans. Geosci. Remote Sens.*, vol. 41, no. 3, pp. 507–517, 2003.
- [6] G. Fornaro and A. Pauciullo, "LMMSE 3-D SAR focusing," *IEEE Trans. Geosci. Remote Sens.*, vol. 47, no. 1, pp. 214–223, Jan. 2009.
- [7] J. Capon, "High-resolution frequency-wavenumber spectrum analysis," *Proceedings of the IEEE*, vol. 57, no. 8, pp. 1408–1418, Aug. 1969.
- [8] R. O. Schmidt, "Multiple emitter location and signal parameter estimation," *IEEE Transactions on Antennas and Propagation*, vol. 34, no. 3, pp. 276–280, Mar. 1986.
- [9] P. Stoica, Z. Wang, and J. Li, "Extended derivations of MUSIC in the presence of steering vector errors," *IEEE Trans. Signal Process.*, vol. 53, no. 3, pp. 1209–1211, Mar. 2005.

-
- [10] P. Stoica, Z. Wang, and J. Li, “Robust Capon beamforming,” *IEEE Signal Processing Letters*, vol. 10, no. 6, pp. 172–175, Jun. 2003.
 - [11] M. Nannini, R. Scheiber, and A. Moreira, “Estimation of the minimum number of tracks for SAR tomography,” *IEEE Trans. Geosci. Remote Sens.*, vol. 47, no. 2, pp. 531–543, Feb. 2009.
 - [12] S. Tebaldini, “Algebraic synthesis of forest scenarios from multibaseline PolInSAR data,” *IEEE Trans. Geosci. Remote Sens.*, vol. 47, no. 12, pp. 4132–4142, Dec. 2009.
 - [13] F. Lombardini and M. Pardini, “3-D SAR tomography: The multibaseline sector interpolation approach,” *IEEE Geosci. Remote Sens. Lett.*, vol. 5, no. 4, pp. 630–634, Oct. 2008.
 - [14] O. Frey, C. Magnard, M. Rüegg, and E. Meier, “Focusing of airborne synthetic aperture radar data from highly nonlinear flight tracks,” *IEEE Trans. Geosci. Remote Sens.*, vol. 47, no. 6, pp. 1844–1858, Jun. 2009.
 - [15] O. Frey, F. Morsdorf, and E. Meier, “Tomographic imaging of a forested area by airborne multi-baseline P-band SAR,” *Sensors, Special Issue on Synthetic Aperture Radar*, vol. 8, no. 9, pp. 5884–5896, Sep. 2008.
 - [16] O. Frey, F. Morsdorf, and E. Meier, “Tomographic processing of multi-baseline P-band SAR data for imaging of a forested area,” in *Proc. IEEE Int. Geosci. and Remote Sens. Symp.*, Jul. 2007, pp. 156–159.
 - [17] P. Stoica and R. L. Moses, *Spectral Analysis of Signals*. Upper Saddle River, NJ: Prentice Hall, 2005.
 - [18] J. Li, P. Stoica, and Z. Wang, “On robust Capon beamforming and diagonal loading,” *IEEE Trans. Signal Process.*, vol. 51, no. 7, pp. 1702–1715, 2003.

5 Analyzing Tomographic SAR Data of a Forest With Respect to Frequency, Polarization, and Focusing Technique

This chapter has been submitted as: O. Frey, E. Meier, 2010. Analyzing Tomographic SAR Data of a Forest With Respect to Frequency, Polarization, and Focusing Technique. IEEE Transactions on Geoscience and Remote Sensing, submitted, June 2010.

Abstract

Forest canopies are semi-transparent to microwaves at both, L- and P-band. Thus, a number of scattering sources and different types of scattering mechanisms may contribute to a single range cell of a SAR image. By appropriately combining SAR data of multiple parallel flight paths, a large two-dimensional aperture is synthesized, which allows for tomographic imaging of the three-dimensional structure of such semi-transparent media and the underlying ground.

A separate paper [1] deals with the actual tomographic imaging part that leads to the three-dimensional data cube. In particular, three focusing techniques are described and analyzed: multilook beamforming, robust Capon beamforming, and MUSIC beamforming.

In this paper, the resulting data products obtained by tomographically focusing two airborne multibaseline SAR data sets of a partially forested area, one at L-band and another at P-band, are subject to a detailed analysis with respect to the location and the type of back-scattering sources. In particular, the following aspects are investigated: 1) The forest structure as obtained from vertical profiles of intensities at sample plot locations within the forest is compared to the height distribution of the top of the forest canopy as derived from airborne laser scanning data. Profiles are presented for all polarimetric channels and focusing techniques, as well as at both frequencies. 2) Type and location of scattering mechanisms are analyzed as a function of height for the two fre-

quencies, L- and P-band, and using the polarimetric channels, as well as Pauli- and Cloude-Pottier-decompositions thereof. 3) The accuracy of the ground elevation estimation obtained from the different focusing techniques and the two frequencies is assessed with the help of a lidar-derived digital elevation model.

5.1 Introduction

Research towards improving the knowledge about the backscattering behavior of forests by means of synthetic aperture radar (SAR) tomography with the eventual goal of estimating its biophysical parameters has become a major topic within the SAR remote sensing community [2–16].

With three prospective spaceborne SAR remote sensing missions, BIOMASS [17, 18] at P-band, Tandem-L [19, 20], and DESDynI [21], both at L-band, which are all aimed at a global mapping and monitoring of carbon stock by assessing the above ground biomass of forests as well as forest dynamics such as the amount of deforestation and re-growth, these two frequency bands have gained in importance. Establishing a good understanding of the interaction of microwaves at L-band and P-band with vegetation, and in particular, with forests, is a prerequisite in order to develop reliable biomass products.

As has been stated in [2, 22–24], simple back-scattering based measurement of biomass is not feasible for dense forested areas due to saturation levels around 100 t/ha at L-band and 200 t/ha at P-band. Inevitably, additional measures, such as the forest height (involving the extraction of the underlying terrain height) and structural information about the forest are to be incorporated into an improved estimation of forest biomass.

Although a number of publications treat advanced algorithms for tomographic SAR imaging (see e.g. [25–38]) much less research has been done that actually incorporates and evaluates real tomographic SAR data of forested areas. In particular, this is the case for P-band data. In [7], back-scattering profiles of a forest extracted from tomographic L-band SAR data were shown and the additional benefit of three-dimensional imaging of forests was highlighted. Excerpts of the same L-band data set are also used in [39], where the superior performance of the Capon beamformer with respect to SPECAN-based beamforming is demonstrated. In [40], FFT, Capon, and MUSIC beamforming approaches based on the deramping and spectral estimation scheme of a stack of coregistered single

look complex images are discussed.

In September 2006, an airborne SAR campaign was flown by the German Aerospace Center's E-SAR system over a test site in Switzerland. Two fully polarimetric tomographic data sets (L-band and P-band) of a partially forested area were taken within this campaign (see Table 5.1 for the sensor specifications and a summary of the parameters which characterize the tomographic data sets). Using this data, first tomographic images of a forest at P-band were presented by Frey et al. [11,12]. The HH polarization channel of the multibaseline P-band data set was tomographically focused using a TDBP approach and a qualitative comparison with an airborne laser scanning (ALS) DEM/DSM data set was carried out. In [41], the TDBP-based focusing methodology was extended towards multilook-based standard and Capon beamforming.

In [13], data from another multibaseline dataset at L-band, also acquired in 2006, was used to experimentally test a method, based on the prolate spheroidal wave functions, to estimate the dimension of the signal subspace for MUSIC beamforming in order to determine the minimum number of baselines needed for tomographic focusing of a forest scenario.

Most recently, Tebaldini [16] proposed a theoretical framework to separate different scattering mechanisms based on polarimetric multibaseline SAR data. Experimental results were provided using an airborne P-band data set acquired during the BioSAR campaign in 2007. In contrast to the tomographic SAR data evaluated in this paper, Tebaldini employed a rather high number of looks (350 looks) to focus the data in the normal direction, leading to a drastic loss of resolution in the range/azimuth domain. In particular, detailed features such as gaps in the canopy due to forest roads or smaller glades and clear cuts are lost to a large extent.

As documented in the recommendations of the PolInSAR 2009 workshop [42], there is still a need for research about the interactions of microwaves at different frequencies with forested areas. The vertical forest structure and terrain reflectivity under vegetated canopies need to be investigated including the polarimetric signature.

5.1.1 Aim of This Paper

This paper attempts to contribute some pieces to diminish this research gap by providing a detailed analysis of the localization of the main back-scattering

	P-band	L-band
Carrier frequency	350 MHz	1.3 GHz
Chirp bandwidth	70 MHz	94 MHz
Sampling rate	100 MHz	100 MHz
PRF	500 Hz	400 Hz
Ground speed	90 m/s	90 m/s
No. of data tracks	11+1	16+1
Nominal track spacing d_n	57 m	14 m
Horizontal baselines	40 m	10 m
Vertical baselines	40 m	10 m
Synthetic aperture in normal direction L	570 m	210 m
Nominal resolution in normal direction δ_n	3 m	2 m
Approx. unambiguous height H	30 m	30 m

Table 5.1: E-SAR system specifications and nominal parameters of the tomographic acquisition patterns for both multibaseline data sets at P-band and L-band.

elements within a three-dimensional SAR data cube. The focused data was obtained by means of non-model-based¹ tomographic processing of two airborne fully-polarimetric multibaseline SAR data sets of the same forested area at both frequencies, L- and P-band (see Table 5.1 for the specifications). Based on a time-domain back-projection approach [43] to a reconstruction grid, three different tomographic focusing techniques: multilook standard beamforming, robust Capon beamforming, and multiple signal classification were applied to the data. For a detailed description of the data processing, an analysis of the focusing performance, and tomographic images of the forest see the companion paper [1].

In this paper, the emphasis is laid on investigating the vertical structure of the forest and its underlying terrain as it appears in the two remotely sensed multibaseline (MB) SAR data sets. To this end, the focused three-dimensional SAR data cubes are analyzed with respect to 1) the location of the main scattering sources within the forested area at the two frequencies with the help of vertical profiles, 2) the type of scattering mechanisms (using the Cloude-Pottier

¹Non-model-based in the sense that no forest model is used. However, multiple signal classification is a model-based direction-of-arrival estimator in the sense that the number of scattering sources are assumed to be known.

decomposition) as a function of height above ground, and 3) the accuracy of the detection of the ground below forest at L-band and P-band using the three different focusing techniques. The 3D SAR data sets are evaluated and cross-validated with high resolution DSM/DEM models derived from ALS.

To the authors' knowledge, this is the first time that a detailed analysis of tomographic SAR data sets, at both, L- *and* P-band, of a forested area is given in combination with high resolution ALS cross-reference data. The authors intend to foster the discussion of the potential of L-band and/or P-band (MB) SAR for the determination of biophysical parameters of forests in the context of biomass/carbon stock assessment.

The remainder of this paper is organized as follows. In Section 5.2, the experimental data is described and the methods used to evaluate the tomographic data are detailed. In the results section, Section 5.3, the back-scattering profiles as analyzed in terms of the parameters frequency, polarization channels, scattering mechanisms, as well as in terms of the focusing technique are presented. In Section 5.4, the results are discussed and conclusions are drawn.

5.2 Data and Methods

5.2.1 Focused Tomographic Data

In Fig. 5.1, the geometric configurations of the actual flight tracks for both tomographic data sets is shown. The flight direction is from east to west and the sensor is left-looking. In addition to the actual flight tracks, their projections to the horizontal plane and to the northing-height plane are also depicted. Both missions were completed by a control track.

The analyses presented in this paper start at the product level of the 3D focused SAR data. For both multibaseline data set, three data products were generated using a time-domain back-projection based approach in combination with

1. coherent multilook beamforming (MLBF)
2. robust Capon beamforming (RCB)
3. multiple signal classification (MUSIC).

A detailed description of the time-domain based focusing methods is given in [41] for MLBF and in a companion paper [1] for RCB and MUSIC, respectively. In

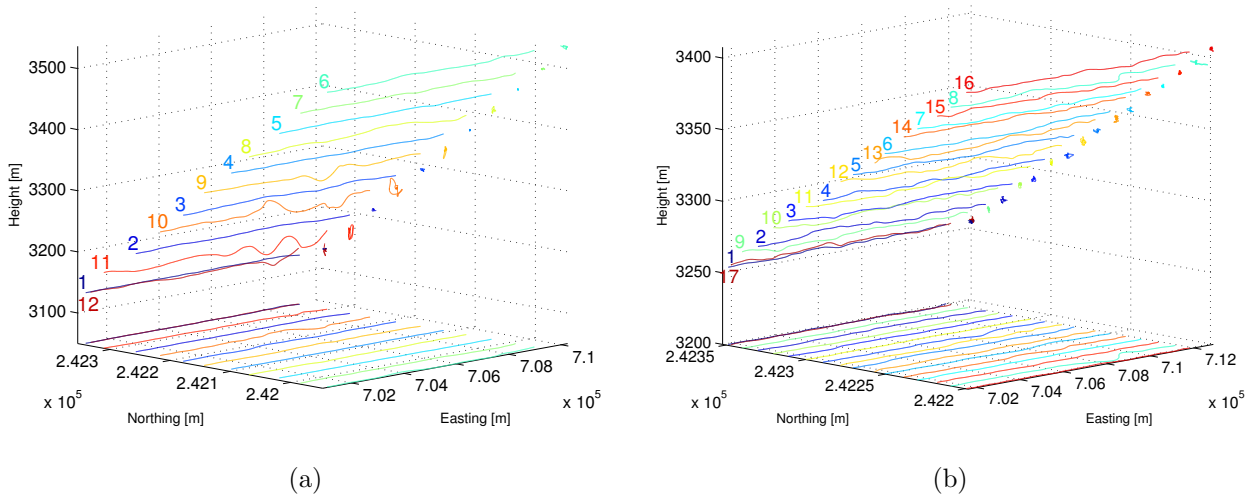


Figure 5.1: Tomographic acquisition patterns at P-band (a), consisting of 11 flight tracks and a control track, and at L-band (b), consisting of 16 flight tracks and a control track. The flight directions are from east to west and the sensors are left-looking. In addition to the actual flight tracks, their projections to the horizontal plane and to the northing-height plane are depicted.

each case, the sample covariance matrix was estimated using approximately 20 looks obtained by spatial averaging.

In our experiment, unambiguous tomographic imaging is limited to 30m in the direction perpendicular to the average line of sight. This constraint is a result of a trade-off which had to be made during the design of the experimental setup of the multibaseline data acquisition for tomographic imaging. The trade-off is between maximizing the height resolution (a synthetic aperture in normal direction as large as possible) and maximizing the unambiguous volume height (the baselines between passes as small as possible) given a limited number of parallel flight paths due to pecuniary constraints, maximal mission time etc. For the given test site and experimental setup this leads to *vertical* unambiguous height values of approximately 16m to 22m depending on the topography and the ground range distance. The tree heights found in the forest under study go up to 40m. The validation of the SAR tomography data is limited to sample plots where the tree height does not exceed the unambiguous height since back-scattering sources that are located beyond that threshold lead to aliasing in the form of ghost targets, which spuriously appear within the unambiguous height.

5.2.2 Validation Data

External reference data in the form of a digital elevation model (DEM) derived from airborne laser scanning (Falcon II, Toposys GmbH) is available for a comparison of the ground level. A digital surface model (DSM) acquired by the same sensor is also at hand (see [1]). Both data sets are given at a sample spacing of 1m x 1m.

The airborne laser scanning data were acquired in spring of 2003. It has to be assumed that the deciduous trees were mostly transparent to the laser signal and therefore do not appear in the LiDAR-derived DSM. However, the forest within the test site is dominated by evergreen coniferous trees (80% of the trees within the sample plots in the area of study are evergreen coniferous trees, predominantly norway spruce ‘*picea abies*’ and european silver fir ‘*abies alba*’, which make up 59% and 20% of all trees, respectively).

As the forest is managed, timber cutting took place between 2003 and 2006. Therefore, additional clear-cuts had to be masked manually into the ALS DSM, based on airborne ortho-images acquired in the summer of 2006. However, cuts of single trees within forest stands are not accounted for. In order to manually insert missing deciduous trees into the DSM, another ALS-derived DSM from summer 2002 was also used.

5.2.3 Methods Used for Data Analysis

In order to analyze the backscattering behavior as a function of height above ground the additional information contained in the polarization channels was exploited. In particular, the Pauli decomposition and the Cloude-Pottier decomposition (entropy/anisotropy/ α) of the polarimetric data were calculated and evaluated as a function of height above ground. In the following, the Pauli decomposition and the Cloude-Pottier decomposition are exposed in some detail for the sake of completeness.

Pauli Decomposition

Using the 2x2 identity matrix and the three Pauli matrices, the scattering matrix \mathbf{S} can be represented as a superposition of four coherent elementary scattering

mechanisms:

$$\mathbf{S} = \begin{bmatrix} S_{HH} & S_{HV} \\ S_{VH} & S_{VV} \end{bmatrix} = \frac{a}{\sqrt{2}}\mathbf{S}_a + \frac{b}{\sqrt{2}}\mathbf{S}_b + \frac{c}{\sqrt{2}}\mathbf{S}_c + \frac{d}{\sqrt{2}}\mathbf{S}_d, \quad (5.1)$$

where

$$\begin{aligned} a &= \frac{S_{HH} + S_{VV}}{\sqrt{2}}, b = \frac{S_{HH} - S_{VV}}{\sqrt{2}}, \\ c &= \frac{S_{HV} + S_{VH}}{\sqrt{2}}, d = i \frac{S_{HV} - S_{VH}}{\sqrt{2}}, \\ \mathbf{S}_a &= \frac{1}{\sqrt{2}} \begin{bmatrix} 1 & 0 \\ 0 & 1 \end{bmatrix}, \mathbf{S}_b = \frac{1}{\sqrt{2}} \begin{bmatrix} 1 & 0 \\ 0 & -1 \end{bmatrix} \\ \mathbf{S}_c &= \frac{1}{\sqrt{2}} \begin{bmatrix} 0 & 1 \\ 1 & 0 \end{bmatrix}, \mathbf{S}_d = \frac{1}{\sqrt{2}} \begin{bmatrix} 0 & -i \\ i & 0 \end{bmatrix}. \end{aligned} \quad (5.2)$$

In the monostatic case reciprocity applies, i.e. $S_{HV} = S_{VH}$ and thus $d = 0$. The remaining three components a, b, and c can be written as the elements of a three-dimensional target vector \mathbf{k} in the Pauli basis [44]

$$\mathbf{k} = \begin{bmatrix} a \\ b \\ c \end{bmatrix} = \frac{1}{\sqrt{2}} \begin{bmatrix} S_{HH} + S_{VV} \\ S_{HH} - S_{VV} \\ 2S_{HV} \end{bmatrix}. \quad (5.3)$$

The components a, b, and c stand for odd-bounce scattering (surface, trihedral reflector), even-bounce scattering from corners with a relative orientation of 0° (dihedral), and 45° (tilted dihedral), respectively.

Cloude-Pottier Decomposition

The Cloude-Pottier decomposition (CPD) [44, 45] is based on the eigenvalue decomposition of the $\mathbf{T3}$ coherency matrix which is constructed from the outer product of the Pauli target vector \mathbf{k} and its Hermitian transpose \mathbf{k}^H

$$\mathbf{T3} = \mathbf{k}\mathbf{k}^H. \quad (5.4)$$

In practice, this single-look representation of the coherency matrix is rank deficient. Assuming ergodicity, a spatial average over n adjacent pixels is taken

(instead of a number of snapshots) which yields the multilook coherency matrix

$$\langle \mathbf{T3} \rangle = \sum_{j=1}^n \mathbf{k}_j \mathbf{k}_j^H . \quad (5.5)$$

Performing the eigenvalue decomposition of the multilook coherency matrix $\langle \mathbf{T3} \rangle$ yields the eigenvalues $\lambda_j, j = 1 \dots 3$, sorted in non-increasing order. Then, the first parameter of the CPD, the entropy H , is calculated as

$$H = \sum_{j=1}^3 -p_j \log_3(p_j) \quad \text{where} \quad p_j = \frac{\lambda_j}{\sum_{m=1}^3 \lambda_m} . \quad (5.6)$$

$H \in [0, 1]$ is a measure for the randomness of a scattering medium from quasi deterministic scattering ($H = 0$) to completely random scattering ($H = 1$). The second parameter, the average alpha angle α , is defined as

$$\alpha = p_1 \alpha_1 + p_2 \alpha_2 + p_3 \alpha_3 \quad (5.7)$$

where $\alpha_j = \arccos(u_{1j})$, as a consequence of the following parameterization of the eigenvectors \mathbf{u}_j of the coherency matrix as introduced in [45],

$$\mathbf{u}_j = [\cos \alpha_j \quad \sin \alpha_j \cos \beta_j e^{i\delta_j} \quad \sin \alpha_j \sin \beta_j e^{i\gamma_j}]^T . \quad (5.8)$$

The average alpha angle α indicates the averaged target scattering mechanism from surface scattering ($\alpha = 0^\circ$), over dipole scattering ($\alpha = 45^\circ$) to dihedral scattering ($\alpha = 90^\circ$), β is the target orientation angle ($-180^\circ \leq \beta < 180^\circ$) and δ and γ are target phase angles [46]. The third parameter of the CPD, which is not used in this paper, is called anisotropy A and is calculated as $A = (p_2 - p_3)/(p_2 + p_3)$. In Fig. 5.2, the H/α plane is shown divided into zones representing different physical scattering characteristics according to the definitions in [45, 47]:

- Z1 High entropy multiple scattering.
- Z2 High entropy vegetation scattering.
- Z3 Non-feasible region.
- Z4 Medium entropy multiple scattering.
- Z5 Medium entropy vegetation scattering.

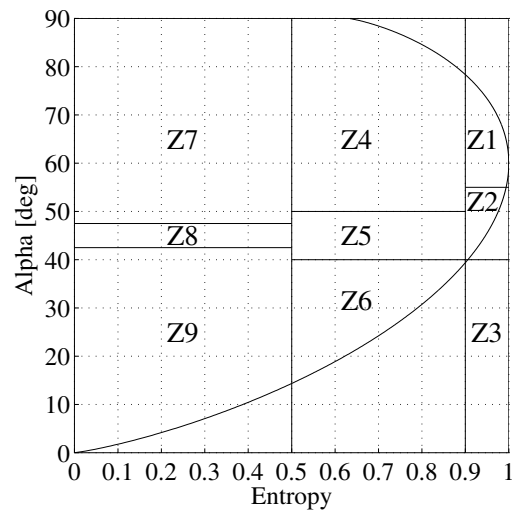


Figure 5.2: Entropy/alpha classification scheme after Cloude and Pottier [45]. See section 5.2.3 for a description of the zones Z1-Z9. Zone 3, the area outside the delineating curve, represents the mathematically non-feasible region.

Z6 Medium entropy surface scattering.

Z7 Low entropy multiple scattering.

Z8 Low entropy dipole scattering.

Z9 Low entropy surface scattering.

In the following, the CPD is used to analyze the back-scattering behavior as a function of the height above ground. The scatter plots at different height levels above ground are distinguishable by different color coding. In addition, the sum of the eigenvalues of the multilook coherency matrix $\langle \mathbf{T3} \rangle$ is incorporated in the form of a transparency value assigned to each data point (see Fig. 5.6 for details). The sum of eigenvalues indicates the total scattering power and is assigned to a transparency value using a logarithmic scale (dB). This additional feature is essential in order to allow for a meaningful interpretation of the H/α scatter plots at different horizontal layers of the three-dimensional data set.

Preparation of the Data Cubes for Analysis

The analyses of the 3D SAR data cubes that are presented in the results section are all made with respect to a ground reference in the form of the DEM from airborne Laser scanning. Prior to any analysis, the data cubes were interpolated in the vertical direction to a sample spacing of 0.15m and each vertical

column was then shifted vertically by a number of voxels corresponding to the point of intersection of the ALS DEM and the three-dimensional voxel grid at each easting/northing position. Thus, the basis for any analysis given in this paper is a modified data cube that has a “flat” horizontal ground elevation at every position and that exhibits an interpolated sample spacing of 0.15m in the vertical direction.

5.3 Experimental Results

5.3.1 Vertical Profiles

In Figs. 5.3 & 5.4, for L-band and P-band, respectively, vertical profiles of relative intensities obtained by averaging the focused, ground-level adjusted tomographic data over a circular sample plot of 300m² are depicted. Profile plots are given for the polarimetric channels HH, HV, and VV, for the three beamforming techniques used for focusing in the normal direction, MLBF, RCB, and MUSIC, as well as for the Pauli basis. The sample plot with numbers 1, 5, and 17 are situated within the forest, whereas the plot number 20 is located on a meadow outside the forested area, with the intention to provide a reference plot that is not subject to volume scattering at canopy level. For the same sample plots, histograms of the difference between the DSM and the DEM obtained from airborne laser scanning were calculated, which are used as a cross-reference estimate of tree heights occurring within a sample plot. The histograms are shown in Fig. 5.5.

5.3.2 Entropy/ α Scatter Plots

In order to discriminate the dominant scattering mechanisms, the entropy/ A/α decomposition at different height levels within the DEM-adjusted three-dimensional SAR data cube was calculated for the four sample plots. In Fig. 5.6, entropy/ α scatter plots are depicted for different horizontal layers at 0m (red), 5m (green), 10m (blue), and 15m (black) above ground. The entropy/ α data points of each layer are plotted using a transparency scaling which is based on the sum of the eigenvalues of the $\mathbf{T3}$ coherence matrix (0dB \rightarrow opaque, ≤ -25 dB \rightarrow transparent).

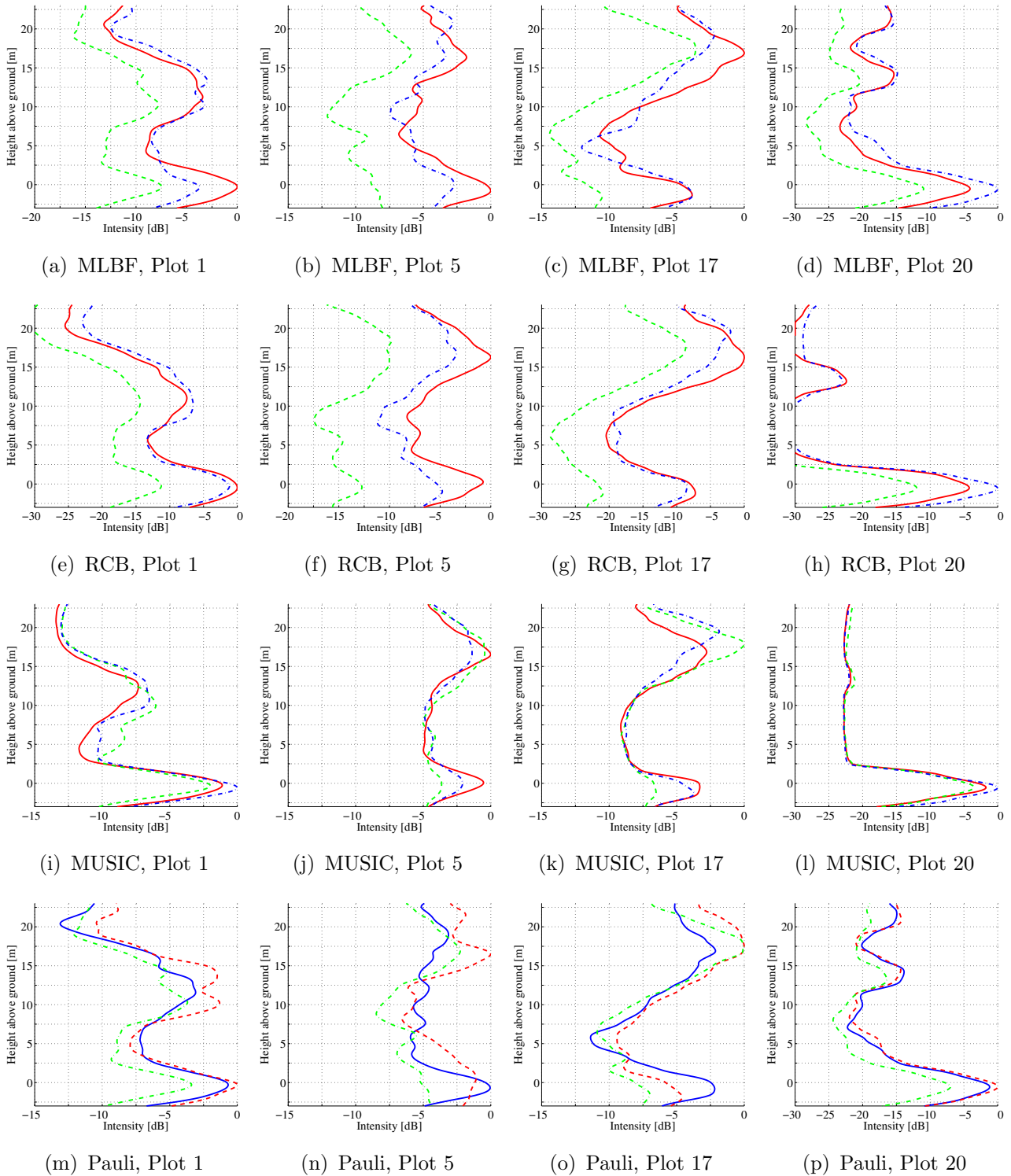


Figure 5.3: Vertical profiles of relative intensities from L-band tomographic data of a forest (Plot 1, 5, and 17) and grass land (Plot 20), respectively, averaged over a circular sample plot of 300m^2 for the polarimetric channels HH (—), HV (---), and VV (---), MLBF, RCB, and MUSIC, as well as the Pauli-basis $HH+VV$ (—), $HH-VV$ (---), and $2*HV$ (---) obtained from MLBF.

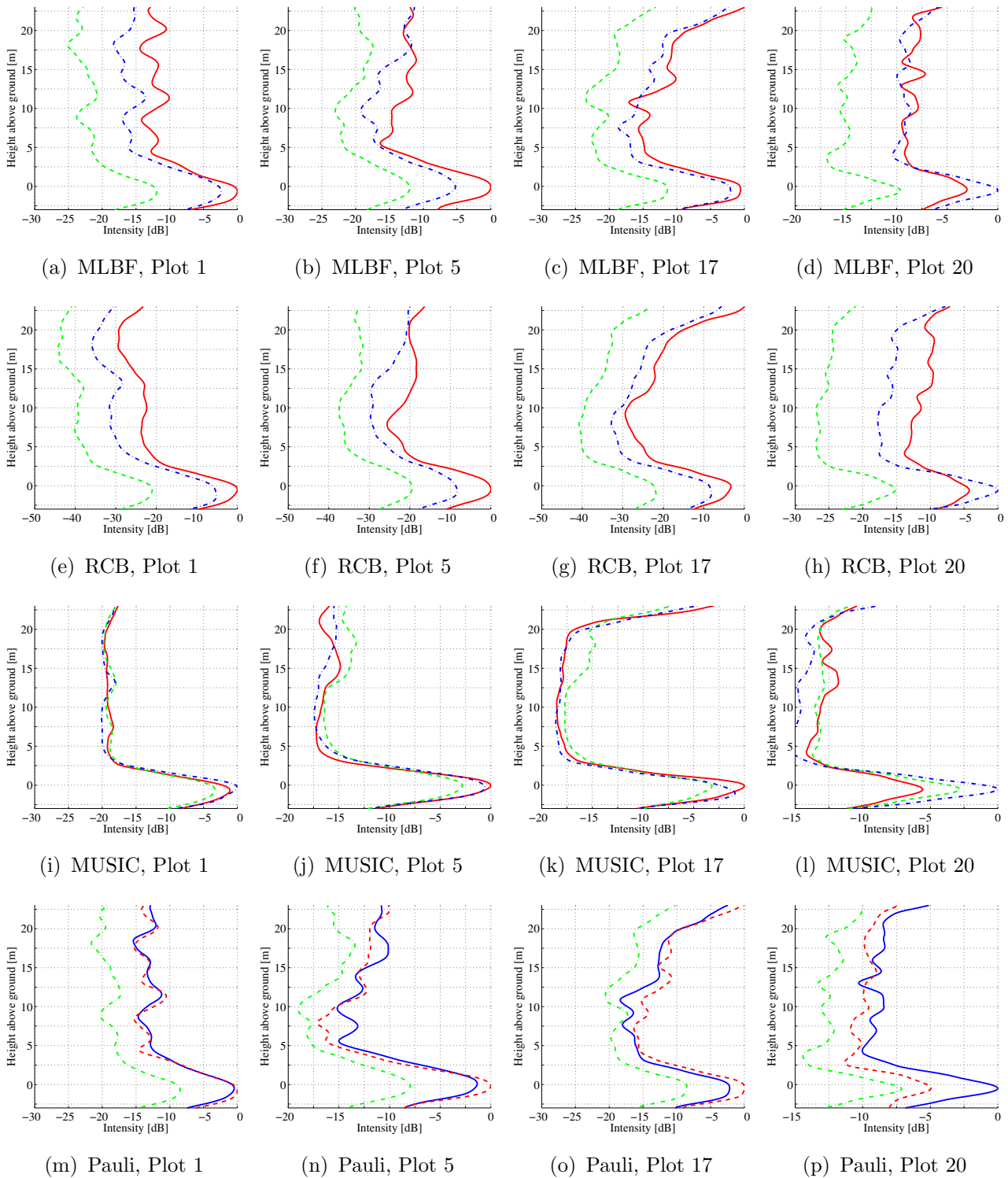


Figure 5.4: Vertical profiles of relative intensities from P-band tomographic data of a forest (Plot 1, 5, and 17) and grass land (Plot 20), respectively, averaged over a circular sample plot of 300m^2 for the polarimetric channels HH (—), HV (---), and VV (---), MLBF, RCB, and MUSIC, as well as the Pauli-basis HH+VV (—), HH-VV (---), and $2*HV$ (-.-) obtained from MLBF.

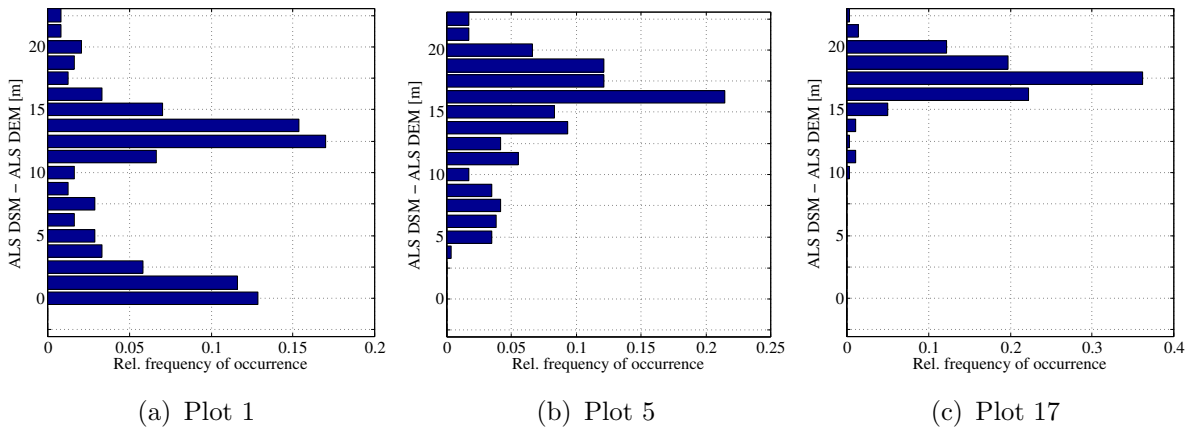


Figure 5.5: Distribution of tree heights occurring within the respective sample plots as estimated by histograms of height differences between the ALS DSM and the ALS DEM.

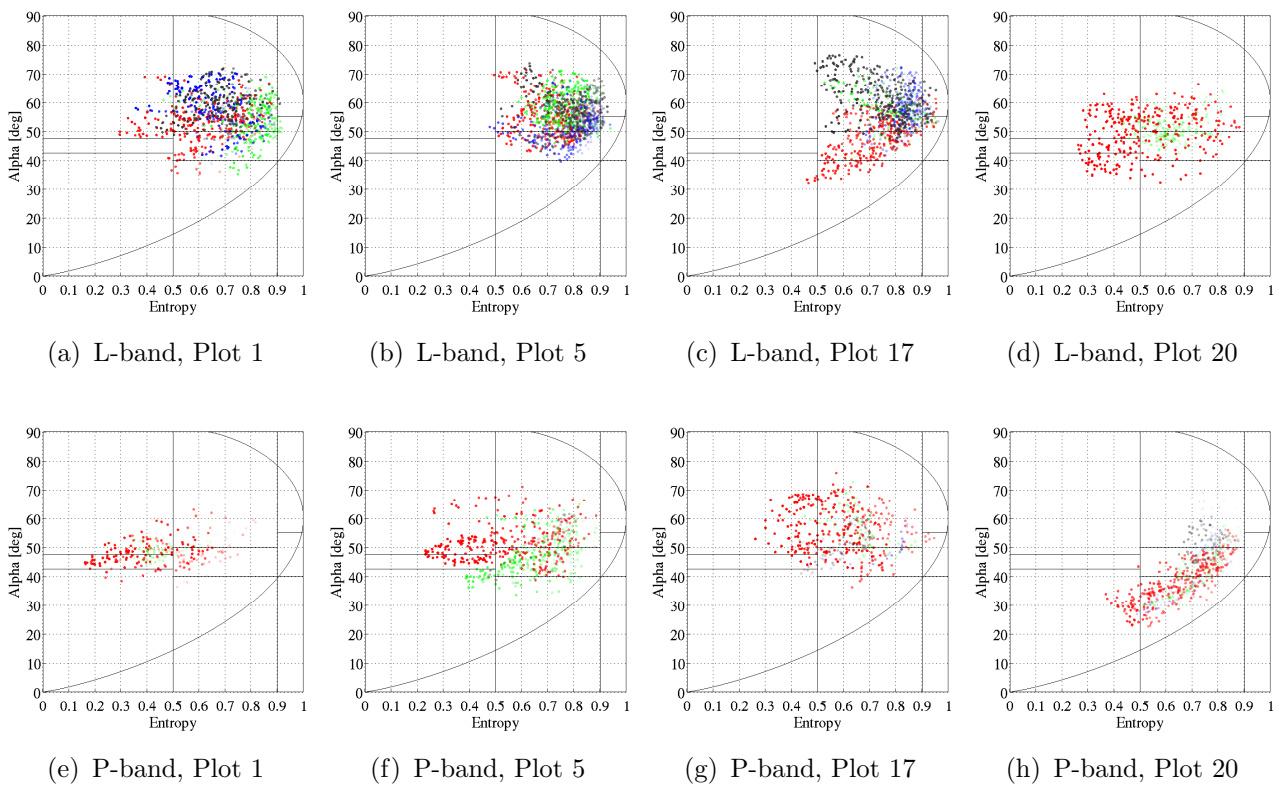


Figure 5.6: Entropy/ α scatter plot for different horizontal slices centered at 0m (red), 5m (green), 10m (blue), 15m (black) above ground (using the ALS-derived DEM as a reference). The entropy/ α data points of each slice are plotted using transparency scaling based on the sum of the eigenvalues of the $\mathbf{T3}$ coherence matrix: 0dB \rightarrow opaque, ≤ -25 dB \rightarrow transparent.

5.3.3 Ground Level Detection

The quality assessment of the ground level detection is based on the assumption that the maximum intensity value within a vertical window of $\pm 4\text{m}$ around the ground level, as indicated by the ALS DEM, represents the location where the backscattering at ground level actually occurs. The relative vertical position of the maximum intensity value was determined for all pixels within a forested subset of the dimension $360\text{m} \times 550\text{m}$ of the area under study. In Figs. 5.7 & 5.8, for L-band and P-band, respectively, the histograms of the relative vertical positions of the maximum intensity value, as well as the corresponding mean values, and standard deviations are given. They indicate the quality of ground level detection below canopy as obtained for the polarization channels HH, HV, VV, and the three focusing techniques MLBF, RCB, and MUSIC.

5.4 Discussion

5.4.1 Vertical Profiles

At L-band, pronounced local maxima are found at both, ground and canopy level in the vertical profiles of relative back-scattering intensities (see Fig. 5.3). In Plot 1, for the MLBF data, distinct back-scattering at canopy level occurs between 7.5m and 16m , with maxima around 12m in the HH channel, 10m in the HV channel, and between 10m and 13m in the VV channel. In Plot 5, the maximum at canopy level is found around $16\text{--}17\text{m}$ in the HH and HV channels, whereas no distinct maximum is observed in the VV channel in the case of the MLBF data set—the RCB and MUSIC beamformers, however, yield a pronounced maximum at the same location. Plot 17 shows high average back-scattering intensity around $17\text{--}18\text{m}$ in the HH and HV channels and $18\text{--}19\text{m}$ above ground in the VV channel.

All three beamforming methods consistently yield intensity maxima at the same locations while the individual shape of the profiles depends on the beamforming method with the, non-surprising, tendency that the superresolution methods, RCB and MUSIC, deliver more pronounced maxima, or a reduced clutter level, respectively. MUSIC beamforming destroys the intensity ratio between the polarization channels.

The maxima of the histograms of the forest tree heights from laser scanning data

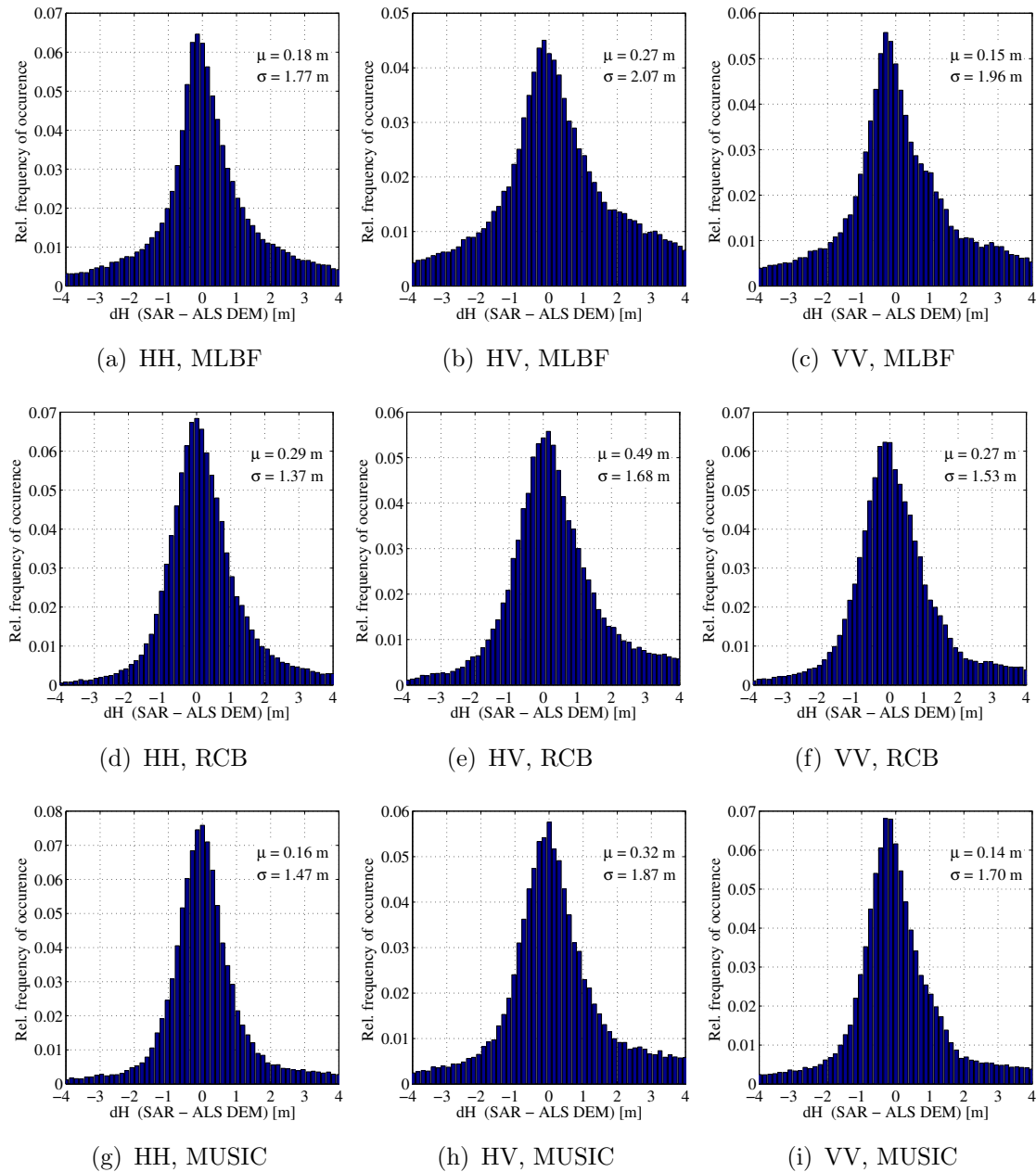


Figure 5.7: Ground level detection below canopy at L-band: Within a vertical window of ± 4 m around the ground level, as indicated by the ALS DEM, the relative vertical position of the maximum intensity value was determined for all pixels within the forested area. The resulting histograms, mean values, and standard deviations are depicted for the polarization channels HH, HV, VV, and the three focusing techniques MLBF, RCB, and MUSIC.

(see Fig. 5.5) are found around 12.5m above ground for Plot 1, 16.25m for Plot 5, and 17.5m for Plot 17. From the coinciding locations of the maxima in the intensity profiles and the histograms, it can be inferred that the intensity profiles

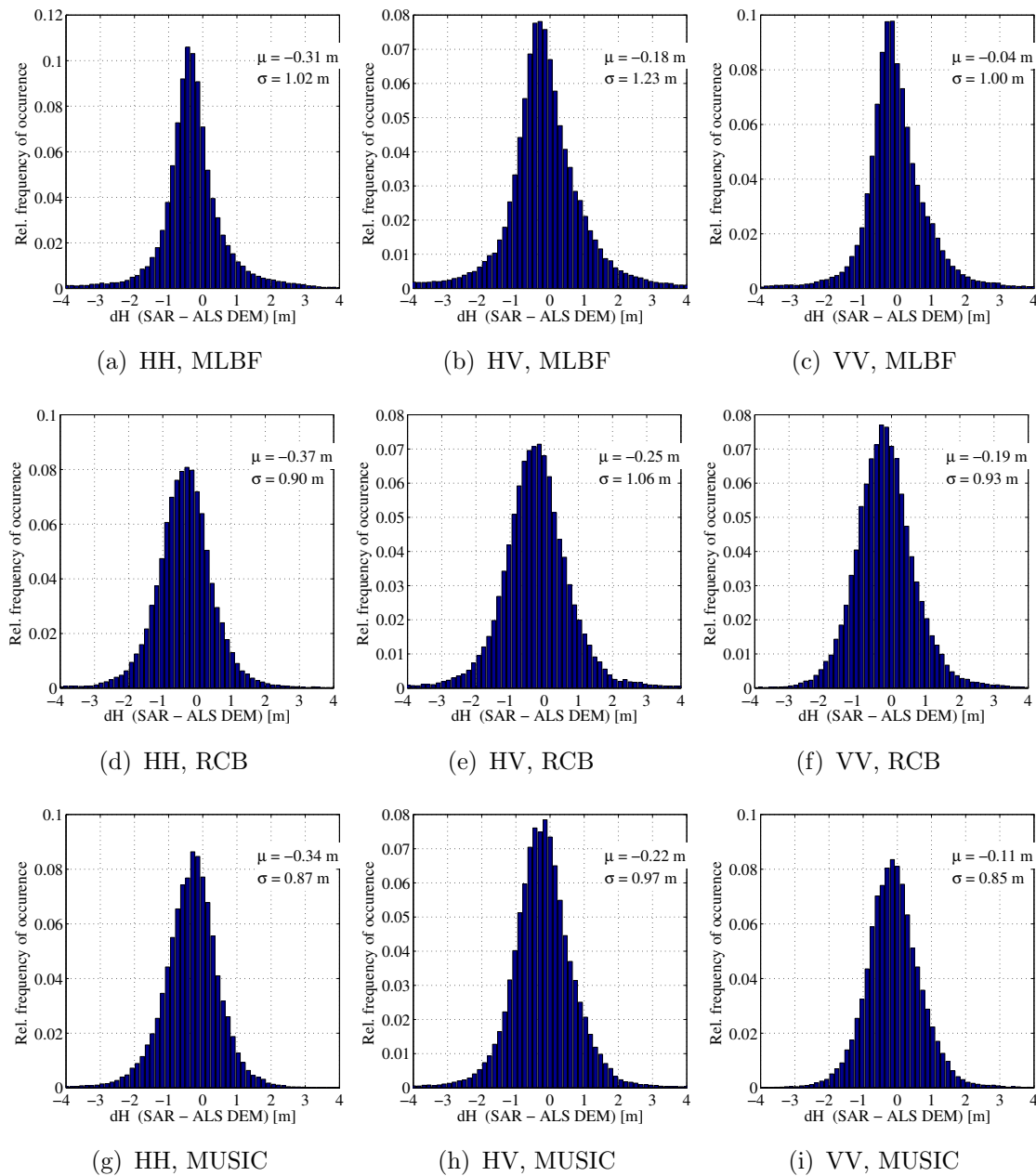


Figure 5.8: Ground level detection below canopy at P-band: Within a vertical window of ± 4 m around the ground level, as indicated by the ALS DEM, the relative vertical position of the maximum intensity value was determined for all pixels within the forested area. The resulting histograms, mean values, and standard deviations are depicted for the polarization channels HH, HV, VV, and the three focusing techniques MLBF, RCB, and MUSIC.

reflect the distribution of tree heights found within a sample plot. This leads to the conclusion that, at L-band, coherent back-scattering within the canopy layer occurs predominantly in the tree-top region for the forest under study.

In Plot 20, which represents grass land outside the forested area, the back-scattering at ground level is clearly visible, accompanied by an anomalous side lobe, which is well-suppressed only by the MUSIC beamformer. Yet visible in the MLBF- and RCB-focused data, the dB-level of the anomalous side lobe is on a lower level compared to the signal stemming from the microwave interaction at canopy-level in Plot 1, 5, and 17.

At P-band, very much in contrast to the L-band case, the ratio between the back-scattering intensity at canopy level and back-scattering intensity at ground level is very low (see Fig. 5.4). Without previous knowledge the canopy level can hardly be localized, at least in the MLBF data set. Nonetheless, a notion of back-scattering measured at canopy level can be observed in some channels for the RCB and MUSIC data sets. A consistent detection of the canopy level seems to be unrealistic; best results would be obtained if only the HV channel was used for the localization of the back-scattering within the canopy layer. Throughout all plots, back-scattering predominantly, if not exclusively, occurs at ground level. Somewhat surprisingly, this observation is made in all polarization channels. The same behavior was also observed by Tebaldini et al. [48, 49] for a different P-band data set. In addition, compared to the L-band case, the unambiguous height appears to be smaller, such that strong ghost target detection occurs around 20m above ground, in particular in Plot 17. Plot 20 again shows the profile for the grass land. In contrast to the L-band case, the signal-clutter-ratio is rather small using MLBF, since grass land is not a strong back-scattering element at wavelengths of 0.75-1m. A much better detection of the ground level is obtained by MUSIC beamforming.

5.4.2 Entropy/ α Scatter Plots

At L-band, for Plot 1 and Plot 5, back-scattering at all height levels is predominantly classified as medium entropy multiple scattering (Z4), medium entropy vegetation scattering (Z5), as well as some low entropy multiple scattering (Z7) for Plot 1 (see Fig. 5.6). Only for Plot 17, a clear separation in the entropy/ α -plane is observed between the contribution at ground level and at canopy level, respectively. The distribution of tree heights in Fig. 5.5 reveals that in Plot 1 and Plot 5 a well-developed understory is present whereas in Plot 17 no understory is identified. This explains why only in Plot 17 distinct surface scattering is found at ground level. The relatively strong back-scattering that is observed within some of the slices centered at 5m above ground has its origin in the

fact that in order to calculate the **T3** coherency matrix a spatial averaging is needed. Thus, through the averaging process in combination with the limited Fourier resolution in normal direction (2m for L-band, 3m for P-band) signal contributions that actually stem from the ground level are attributed to the slice 5m above ground.

At P-band, relevant back-scattering is virtually exclusively found at ground level. Plot 1 exhibits a somewhat complementary picture to the L-band case: back-scattering at ground level is primarily classified as low entropy dipole (Z8) and low entropy multiple scattering (Z7). A possible explanation for the high portion of volume scattering detected at ground level within the forest, as found in Plot 5 and Plot 17, is the moderately non-zero slope of the underlying terrain.

Substantial surface scattering is found for the grass land sample plot at P-band (Plot 20), whereas at L-band a mixed picture of mostly medium entropy scattering is present.

5.4.3 Ground Level Detection

As is readily observed in Figs. 5.7 & 5.8, the ground level is properly detected at both L-band and P-band. At L-band, the average vertical position of the maximum intensity within a window of $\pm 4\text{m}$ around the reference ground level from ALS lies between 0.15m and 0.49m indicating a slightly positive bias compared to the reference ground level. The best standard deviation (1.37m) is achieved for RCB of the HH channel. At P-band, the ground level is underestimated on average by -0.04m to -0.37m with respect to the cross-reference data. The standard deviations range from 0.85m to 1.23m with the best value obtained for MUSIC beamforming of the VV channel. In general, the detection of the ground level is slightly better at P-band as indicated by the narrower shape of the histograms and the lower standard deviations. This outcome is in line with the results obtained from analyzing the profile plots and the entropy/ α plots, where strong back-scattering at ground level has also been found at both frequencies with higher relative intensity values at P-band.

5.5 Conclusion

An extensive analysis of polarimetric SAR tomography data sets of a forested area, for the first time at both frequencies, L-band and P-band, has been presented. Three data products obtained by time-domain based MLBF, RCB, and MUSIC beamforming have been investigated for each frequency.

At L-band, main back-scattering contributions are observed at both the ground level and around the tree top. RCB and MUSIC beamforming based vertical profiles exhibit a more distinct tomographic image by increasing the signal-to-clutter ratio and the resolution in normal direction. Thus, in order to just detect the location of the main back-scattering contributions they provide an improved performance compared to MLBF.

A comparison of the vertical profiles of relative intensities of the SAR tomography data and the histograms of the tree heights, as estimated from the difference between the DSM and the DEM from airborne laser scanning, revealed a striking difference in terms of the location of dominant back-scatterers for the two wavelengths: at L-band, coherent back-scattering from the canopy (mostly in the tree-top region) is present in all polarization channels, whereas, at P-band, only the HV channel exhibits a, still very moderate, local maximum at the canopy level. We conclude that, at P-band, the canopy of the forest under study is virtually transparent to the microwaves, whereas, at L-band, both the forest canopy as well as the ground level are detected. Somewhat unexpectedly, at P-band, the main scattering within the forest occurs at the ground level not only in the HH and VV channels, but *also in the cross-polarized channels*. The same behavior was also observed by Tebaldini et al. [48, 49] for a different P-band data set.

Within the forest, surface scattering is very limited even at L-band. Only for Plot 17, where no understory is present, (medium entropy) surface scattering is shown by the entropy/ α scatter plot. Interestingly, the back-scattering classification does not change much as a function of height within the forest volume at L-band. This indicates that back-scattering sources at ground level and within the canopy layer are not necessarily distinguishable only by their polarimetric signature. At P-band, where scattering at the ground level dominates, the entropy/ α plots show hardly any surface scattering but mostly dipole and volume scattering.

The ground level is well detected at both, L-band and P-band, and in all polar-

ization channels; the detection of the ground level is slightly superior at P-band, though.

As mentioned, the study is limited in so far, that only a sector of 30m in normal direction can be imaged unambiguously, which renders regions of higher canopy out of the scope of this analysis. However, for the selected sample plots, which feature tree heights within this limit, the actual location and type of back-scattering mechanisms within the conifer-dominated forest was successfully assessed at L-band and P-band with the help of experimental polarimetric SAR tomography data sets.

In view of the potential upcoming mission BIOMASS, it is interesting to note that, at P-band, coherent back-scattering occurs at the ground level. Thus, mapping of the terrain underneath foliage by means of SAR interferometry is a potential scenario. On the other hand, repeat pass interferometry at P-band is limited, due to the small bandwidth assigned at this frequency range, due to the resulting moderate resolution, and to some extent also due to temporal decorrelation effects.

Looking at the fact that, at L-band, two main locations of back-scattering sources could be identified—canopy top and ground level—a single-pass interferometric system, such as sketched in the Tandem-L proposal, appears to be favorable compared to a pure repeat-pass imaging system at L-band.

An open question is to what extent back-scattering sources at the various height levels within a forest can be separated reliably in cases where only a very limited number of baselines are available.

References

- [1] O. Frey and E. Meier, “3D SAR imaging of a forest using airborne multi-baseline data at L- and P-band,” *IEEE Trans. Geosci. Remote Sens.*, pp. –, 2010, submitted.
- [2] M. L. Imhoff, “Radar backscatter and biomass saturation: ramifications for global biomass inventory,” *IEEE Trans. Geosci. Remote Sens.*, vol. 33, no. 2, pp. 511–518, Mar. 1995.
- [3] J. Hagberg, L. Ulander, and J. Askne, “Repeat-pass SAR interferometry over forested terrain,” *IEEE Trans. Geosci. Remote Sens.*, vol. 33, no. 2, pp. 331–340, Mar. 1995.

- [4] R. N. Treuhaft, S. N. Madsen, M. Moghaddam, and J. J. van Zyl, "Vegetation characteristics and underlying topography from interferometric radar," *Radio Science*, vol. 31, no. 6, pp. 1449–1485, 1996.
- [5] S. R. Cloude and K. P. Papathanassiou, "Polarimetric SAR interferometry," *IEEE Trans. Geosci. Remote Sens.*, vol. 36, no. 5, pp. 1551–1565, Sep. 1998.
- [6] R. N. Treuhaft and S. R. Cloude, "The structure of oriented vegetation from polarimetric interferometry," *IEEE Trans. Geosci. Remote Sens.*, vol. 37, no. 5, pp. 2620–2624, Sep. 1999.
- [7] A. Reigber and A. Moreira, "First demonstration of airborne SAR tomography using multibaseline L-band data," *IEEE Trans. Geosci. Remote Sens.*, vol. 38, no. 5, pp. 2142–2152, 2000.
- [8] J.-S. Lee, S. R. Cloude, K. P. Papathanassiou, M. R. Grunes, and I. H. Woodhouse, "Speckle filtering and coherence estimation of polarimetric SAR interferometry data for forest applications," *IEEE Trans. Geosci. Remote Sens.*, vol. 41, no. 10, pp. 2254–2263, Oct. 2003.
- [9] R. N. Treuhaft, B. E. Law, and G. P. Asner, "Forest attributes from radar interferometric structure and its fusion with optical remote sensing," *BioScience*, vol. 54, no. 6, pp. 561–571, 2004.
- [10] B. Hallberg, G. Smith, A. Olofsson, and L. M. H. Ulander, "Performance simulation of spaceborne P-band SAR for global biomass retrieval," in *Proc. IEEE Int. Geosci. and Remote Sens. Symp.*, Sep. 2004, pp. 503–506.
- [11] O. Frey, F. Morsdorf, and E. Meier, "Tomographic processing of multi-baseline P-band SAR data for imaging of a forested area," in *Proc. IEEE Int. Geosci. and Remote Sens. Symp.*, Jul. 2007, pp. 156–159.
- [12] O. Frey, F. Morsdorf, and E. Meier, "Tomographic imaging of a forested area by airborne multi-baseline P-band SAR," *Sensors, Special Issue on Synthetic Aperture Radar*, vol. 8, no. 9, pp. 5884–5896, Sep. 2008.
- [13] M. Nannini, R. Scheiber, and A. Moreira, "Estimation of the minimum number of tracks for SAR tomography," *IEEE Trans. Geosci. Remote Sens.*, vol. 47, no. 2, pp. 531–543, Feb. 2009.
- [14] R. N. Treuhaft, B. D. Chapman, J. R. dos Santos, F. G. Gonçalves, L. V. Dutra, P. M. L. A. Graça, and J. B. Drake, "Vegetation profiles in tropical forests from multibaseline interferometric synthetic aperture radar, field, and lidar measurements," *J. Geophys. Res.*, vol. 114, pp. 1–16, Dec. 2009.

- [15] F. Garestier, P. C. Dubois-Fernandez, D. Guyon, and T. Le Toan, "Forest biophysical parameter estimation using L- and P-band polarimetric SAR data," *IEEE Trans. Geosci. Remote Sens.*, vol. 47, no. 10, pp. 3379–3388, Oct. 2009.
- [16] S. Tebaldini, "Algebraic synthesis of forest scenarios from multibaseline PolInSAR data," *IEEE Trans. Geosci. Remote Sens.*, vol. 47, no. 12, pp. 4132–4142, Dec. 2009.
- [17] "Candidate Earth explorer core mission BIOMASS - report for assessment," ESA SP-1313/2, Tech. Rep., Nov. 2008. [Online]. Available: http://esamultimedia.esa.int/docs/SP1313-2_BIOMASS.pdf
- [18] F. Hélière, C. Lin, F. Fois, M. Davidson, A. Thompson, and P. Bensi, "BIOMASS: A P-band SAR Earth explorer core mission candidate," in *Proc. IEEE Radar Conf.*, May 2009, pp. 1–6.
- [19] A. Moreira, G. Krieger, I. Hajnsek, K. Papathanassiou, M. Eineder, F. D. Zan, M. Younis, and M. Werner, "Tandem-L: Monitoring the Earth's dynamics with InSAR and Pol-InSAR," in *Proc. PolInSAR*, Frascati, Italy (ESA SP-668), Jan. 2009.
- [20] G. Krieger, I. Hajnsek, K. P. Papathanassiou, M. Eineder, M. Younis, F. De Zan, P. Prats, S. Huber, M. Werner, H. Fiedler, A. Freeman, P. Rosen, S. Hensley, W. Johnson, L. Villeux, B. Grafmueller, R. Werninghaus, R. Bamler, and A. Moreira, "The Tandem-L mission proposal: Monitoring Earth's dynamics with high resolution SAR interferometry," in *Proc. IEEE Radar Conf.*, May 2009, pp. 1–6.
- [21] A. Donnellan, P. Rosen, J. Graf, A. Loverro, A. Freeman, R. Treuhaft, R. Oberto, M. Simard, E. Rignot, R. Kwok, X. Pi, J. Blair, W. Abdalati, J. Ranson, H. Zebker, B. Hager, H. Shugart, M. Fahnestock, and R. Dubayah, "Deformation, ecosystem structure, and dynamics of ice (DESDynI)," in *Proc. IEEE Aerospace Conf.*, Mar. 2008, pp. 1–13.
- [22] M. C. Dobson, F. T. Ulaby, T. LeToan, A. Beaudoin, E. S. Kasischke, and N. Christensen, "Dependence of radar backscatter on coniferous forest biomass," *IEEE Trans. Geosci. Remote Sens.*, vol. 30, no. 2, pp. 412–415, Mar. 1992.
- [23] H. Israelsson, L. M. H. Ulander, J. L. H. Askne, J. E. S. Fransson, P.-O. Frörlind, A. Gustavsson, and H. Hellsten, "Retrieval of forest stem volume

- using VHF SAR,” *IEEE Trans. Geosci. Remote Sens.*, vol. 35, no. 1, pp. 36–40, Jan. 1997.
- [24] R. F. Nelson, P. Hyde, P. Johnson, B. Emessiene, M. L. Imhoff, R. Campbell, and W. Edwards, “Investigating RaDAR-LiDAR synergy in a North Carolina pine forest,” *Remote Sensing of Environment*, vol. 110, no. 1, pp. 98–108, Sep. 2007.
- [25] P. Pasquali, C. Prati, F. Rocca, M. Seymour, J. Fortuny, E. Ohlmer, and A. J. Sieber, “A 3-D SAR experiment with EMSL data,” in *Proc. IEEE Int. Geosci. and Remote Sens. Symp.*, vol. 1, 1995, pp. 784–786.
- [26] C. Jakowatz and P. Thompson, “A new look at spotlight mode synthetic aperture radar as tomography: imaging 3-D targets,” *IEEE Trans. Image Process.*, vol. 4, no. 5, pp. 699–703, 1995.
- [27] J. Homer, I. Longstaff, and G. Callaghan, “High resolution 3-D SAR via multi-baseline interferometry,” in *Proc. IEEE Int. Geosci. and Remote Sens. Symp.*, vol. 1, May 1996, pp. 796–798.
- [28] J. Li, Z.-S. Liu, and P. Stoica, “3-D target feature extraction via interferometric SAR,” *Proc. Inst. Elect. Eng.—Radar, Sonar Navig.*, vol. 144, no. 2, pp. 71–80, 1997.
- [29] L. Rössing and J. H. Ender, “Multi-antenna SAR tomography using super-resolution techniques,” *EUSAR 2000 Special Issue, Frequenz, Zeitschrift für Telekommunikation (Journal of Telecommunications)*, vol. 55, pp. 123–128, Mar. 2001.
- [30] P. Berardino, G. Fornaro, R. Lanari, E. Sansosti, F. Serafino, and F. Soldovieri, “Multi-pass synthetic aperture radar for 3-D focusing,” in *Proc. IEEE Int. Geosci. and Remote Sens. Symp.*, vol. 1, 2002, pp. 176–178.
- [31] F. Bordoni, F. Lombardini, F. Gini, and A. Jakobsson, “Multibaseline cross-track SAR interferometry using interpolated arrays,” *IEEE Trans. Aerosp. Electron. Syst.*, vol. 41, no. 4, pp. 1473–1482, 2005.
- [32] G. Fornaro, F. Serafino, and F. Soldovieri, “Three-dimensional focusing with multipass SAR data,” *IEEE Trans. Geosci. Remote Sens.*, vol. 41, no. 3, pp. 507–517, 2003.
- [33] F. Gini, F. Lombardini, and M. Montanari, “Layover solution in multibaseline SAR interferometry,” *IEEE Trans. Aerosp. Electron. Syst.*, vol. 38, no. 4, pp. 1344–1356, 2002.

- [34] F. Lombardini, M. Montanari, and F. Gini, "Reflectivity estimation for multibaseline interferometric radar imaging of layover extended sources," *IEEE Trans. Signal Process.*, vol. 51, no. 6, pp. 1508–1519, Jun. 2003.
- [35] Z. Su, Y. Peng, and X. Wang, "Feature-independent aperture evaluator for the curvilinear SAR," *IEEE Geosci. Remote Sens. Lett.*, vol. 4, no. 2, pp. 191–195, Apr. 2007.
- [36] F. Lombardini and M. Pardini, "3-D SAR tomography: The multibaseline sector interpolation approach," *IEEE Geosci. Remote Sens. Lett.*, vol. 5, no. 4, pp. 630–634, Oct. 2008.
- [37] M. Pardini, F. Lombardini, and F. Gini, "The hybrid Cramér – Rao bound on broadside DOA estimation of extended sources in presence of array errors," *IEEE Trans. Signal Process.*, vol. 56, no. 4, pp. 1726–1730, Apr. 2008.
- [38] G. Fornaro and A. Pauciullo, "LMMSE 3-D SAR focusing," *IEEE Trans. Geosci. Remote Sens.*, vol. 47, no. 1, pp. 214–223, Jan. 2009.
- [39] F. Lombardini and A. Reigber, "Adaptive spectral estimation for multi-baseline SAR tomography with airborne L-band data," in *Proc. IEEE Int. Geosci. and Remote Sens. Symp.*, vol. 3, 2003, pp. 2014–2016.
- [40] S. Guillaso and A. Reigber, "Polarimetric SAR Tomography (POLTOM-SAR)," in *Proc. PolInSAR*, Frascati, Italy, 2005.
- [41] O. Frey and E. Meier, "Combining time-domain back-projection and Capon beamforming for tomographic SAR processing," in *Proc. IEEE Int. Geosci. and Remote Sens. Symp.*, 2008, pp. 445–448.
- [42] "PolInSAR 2009 sorted recommendations," ESA, Frascati, Italy, Jan. 2009. [Online]. Available: http://earth.esa.int/workshops/polinsar2009/POLInSAR2009_sorted_rec.pdf
- [43] O. Frey, C. Magnard, M. Rüegg, and E. Meier, "Focusing of airborne synthetic aperture radar data from highly nonlinear flight tracks," *IEEE Trans. Geosci. Remote Sens.*, vol. 47, no. 6, pp. 1844–1858, Jun. 2009.
- [44] S. R. Cloude and E. Pottier, "A review of target decomposition theorems in radar polarimetry," *IEEE Trans. Geosci. Remote Sens.*, vol. 34, no. 2, pp. 498–518, Mar. 1996.
- [45] S. R. Cloude and E. Pottier, "An entropy based classification scheme

- for land applications of polarimetric SAR,” *IEEE Trans. Geosci. Remote Sens.*, vol. 35, no. 1, pp. 68–78, Jan. 1997.
- [46] S. R. Cloude, J. Fortuny, J. M. Lopez-Sanchez, and A. J. Sieber, “Wide-band polarimetric radar inversion studies for vegetation layers,” *IEEE Trans. Geosci. Remote Sens.*, vol. 37, no. 5, pp. 2430–2441, Sep. 1999.
- [47] J.-S. Lee, M. R. Grunes, T. L. Ainsworth, L.-J. Du, D. L. Schuler, and S. R. Cloude, “Unsupervised classification using polarimetric decomposition and the complex Wishart classifier,” *IEEE Trans. Geosci. Remote Sens.*, vol. 37, no. 5, pp. 2249–2258, Sep. 1999.
- [48] S. Tebaldini, F. Rocca, and A. Monti-Guarnieri, “Model based SAR tomography of forested areas,” in *Proc. IEEE Int. Geosci. and Remote Sens. Symp.*, vol. 2, Jul. 2008, pp. 593–596.
- [49] S. Tebaldini and F. Rocca, “Polarimetric options for SAR tomography of forested areas,” in *Proc. PolInSAR*. Frascati, Italy: ESA SP-668, Jan. 2009.

6 Synopsis

6.1 Main Findings

In the following, the main findings of this research project are reported structured according to the research questions as formulated in Section 1.4.2 and as treated in the four publications (Chapters 2–5) that form this thesis.

6.1.1 Nonlinear Flight Tracks

Publication 1 (Chapter 2):

O. Frey, C. Magnard, M. Rüegg, and E. Meier, 2009. “Focusing of Airborne Synthetic Aperture Radar Data From Highly Nonlinear Flight Tracks.” *IEEE Transactions on Geoscience and Remote Sensing*, 47(6):1844–1858.

- **What is the imaging performance of TDBP as opposed to the ECS&M approach and are these methods suitable with respect to potential applications such as corridor mapping along nonlinear features of interest?**

In an airborne SAR experiment designed to study the effects of various nonlinearly shaped sensor trajectories on SAR imagery, two different SAR imaging approaches, that were identified to have the potential to cope with highly nonlinear sensor motion, were investigated: 1) a patchwise focusing and mosaicking approach based on the ECS algorithm, and 2) a flexible TDBP approach, which utilizes the true 3D acquisition geometry. It was shown that patchwise frequency-domain processing and mosaicking is limited because of two opposing requirements on the azimuth length of a patch: 1) A higher flight-track nonlinearity would require patches with a shorter azimuth length, and 2) the minimal length of a patch is determined by the azimuth beam width of the antenna. A large azimuth beam width is often preferable in order to ensure a continuous coverage of the region of interest even for large attitude variations along the sensor trajectory. In contrast, the proposed TDBP algorithm has proven to

be a robust processing method when a highly nonlinear sensor trajectory, in combination with a large synthetic aperture, would otherwise lead to defocused imagery. A good imaging performance is obtained due to a rigorous treatment of the nontrivial three-dimensional acquisition geometry during the focusing procedure. In addition, the TDBP approach allows any subregion of interest to be selected and focused without the need to process the entire data set.

Thus, the TDBP-based approach provides the means for a high-quality corridor mapping of curvilinear features such as rivers or traffic routes. It features flexible and parallelized processing of subareas of interest within a SAR data set acquired from virtually arbitrarily-shaped flight tracks in combination with a direct and phase-preserving mapping functionality in any desired coordinate frame and map projection.

6.1.2 SAR Tomography

Publication 2 (Chapter 3):

O. Frey, F. Morsdorf, and E. Meier, 2008. “Tomographic Imaging of a Forested Area By Airborne Multi-Baseline P-Band SAR.” *Sensors, Special Issue on Synthetic Aperture Radar*, 8(9):5884–5896.

- **What is the imaging performance obtained with a three-dimensional pure TDBP approach when tomographically imaging a forested area at P-band and where are the main backscattering sources located?**

In this work, for the first time, a forested area was imaged by tomographic processing of multi-baseline P-band SAR. The processing approach implemented consists of a pure TDBP imaging of the SAR signal to a three-dimensional reconstruction grid. The TDBP-based method, which maintains the geometric relationship between the original sensor positions and the imaged target, is able to handle irregular sampling without introducing any approximations with respect to the geometry. The tomographic imaging performance, assessed by analyzing the impulse response of simulated point targets and an in-scene corner reflector, was found to be compliant with the theoretical values in terms of resolution. However, high intensity values within the tomographic images are often accompanied by considerable anomalous side lobes in the normal direction. Therefore, the target-to-clutter ratio needs to be increased by applying more

advanced processing techniques, as treated in Publication 3. In particular, multilooking is to be implemented to stabilize the image inversion process in the normal direction.

A qualitative comparison of the tomographic slices resulting from the airborne multi-baseline P-band data set with a DEM/DSM obtained from laser scanning indicates that high intensity values are predominantly located at the ground level within forested areas. This result supports the claim that DEMs obtained by means of P-Band interferometry provide a good estimate of the ground topography underneath canopy.

Publication 3 (Chapter 4):

O. Frey, E. Meier, 2010. "3D SAR Imaging of a Forest Using Airborne Multi-baseline Data at L- and P-Band." Submitted to *IEEE Transactions on Geoscience and Remote Sensing*, June 2010.

- **What is the imaging performance obtained with the three different tomographic imaging approaches: multilook standard beamforming, robust Capon beamforming, and multiple signal classification at L-band and P-band?**
- **What is the imaging performance using the full set of baselines as compared to a reduced set?**

In this paper, the imaging performance of a TDBP-based tomographic signal processor was analyzed using the experimental multibaseline data sets at L-band and P-band. Three tomographic imaging approaches were subject to a comparative analysis: multilook standard beamforming (MLBF), robust Capon beamforming (RCB), and MUSIC beamforming. In addition, the focusing performance was assessed with respect to processing the full set of baselines and a reduced set of baselines, respectively.

Based on an analysis of the impulse response of a trihedral corner reflector it was found that RCB and MUSIC beamforming, compared to MLBF, yield an enhanced suppression of the side lobes at both frequencies. If the synthetic aperture in normal direction is cut down to half of the full size by using only a reduced set of baselines the resolution and the suppression of side lobes within the MLBF-focused data set degrade considerably. On the other hand, RCB and MUSIC are able to maintain a high resolution as well as an effective suppression

of the side lobes. In addition, using the super-resolution techniques RCB and MUSIC, the effect of potential steering vector errors, a major source responsible for defocused imagery, is much reduced leading to an improved focusing quality.

By means of an exemplary tomographic 3D voxel image resulting from MUSIC focusing of a forested area it was demonstrated that an unprecedented level of detail is obtained using the proposed TDBP-based focusing approach. The high processing quality allows for employing a lower number of looks to focus the data in the normal direction. As a direct beneficial consequence, the resolution in the range/azimuth domain is still at an acceptable level, such that gaps in the canopy due to features like small forest roads, of a width of a few meters only, are well visible in the tomographic image.

The three-dimensional tomographic SAR imagery provides a basis for a detailed investigation of the back-scattering properties of the forested area at L-band and P-band.

Publication 4 (Chapter 5):

O. Frey, E. Meier, 2010. “Analyzing Tomographic SAR Data of a Forest With Respect to Frequency, Polarization, and Focusing Technique”. Submitted to *IEEE Transactions on Geoscience and Remote Sensing*, June 2010.

- **What features of the forest (canopy top, forest structure, terrain level) can be imaged at the different frequencies and polarization channels and using different focusing techniques?**
- **What types of scattering mechanisms are found by applying polarimetric decompositions to the three-dimensional tomography data sets at both frequencies?**
- **Is the information obtained consistent with the cross-reference in the form of a digital surface model and a digital elevation model obtained from airborne laser scanning?**

Within this work, the SAR tomography data products at L-band and P-band, generated as described in Publication 3, were analyzed with respect to their ability to map structural features of the forested area under study, such as the detection of the ground level underneath foliage, forest height, as well as the prevalent scattering mechanisms. The analysis of the three-dimensional data cubes was aimed at identifying 1) which frequency, which polarization,

and which focusing technique (MLBF, RCB, or MUSIC beamforming) is best suitable to reveal certain features of the forest, and 2) how accurately these features are detected.

It was found that, at L-band, the main back-scattering contributions are observed at both the ground level and around the tree top. A comparison of the back-scattering locations with histograms of the tree heights as estimated from the difference between the DSM and the DEM from airborne laser scanning clearly showed that back-scattering from the canopy is actually located at tree-top level. Thus, the structural information obtained from the SAR tomography data sets at L-band is in agreement with the cross-reference data. By contrast, at P-band, the canopy of the forest under study is virtually transparent to the microwaves. The ground level is well detected in all polarization channels at L- and P-band, the detection being slightly superior at P-band. It was also observed that RCB and MUSIC allow for an improved detection of the location of the main back-scattering contributions as compared to MLBF.

Analyzing the polarimetric decompositions as a function of height indicated that, within the forest, surface scattering occurs scarcely, even at L-band, and only in the case where no understory is present. Interestingly, the back-scattering classification does not change much as a function of height within the forest volume. At P-band, where scattering at the ground level dominates, the entropy/ α plots show hardly any surface scattering but mostly dipole scattering and volume scattering.

6.2 Conclusion

A highly flexible synthetic aperture radar signal processing software has been developed and implemented within this dissertation. The suitability of the TDBP-based imaging algorithm for high-quality processing of SAR data obtained from nonstandard acquisition scenarios was demonstrated by means of two dedicated airborne SAR experiments that were designed and conducted within this project.

With the help of the first experiment, which involved highly nonlinear sensor trajectories flown by an airborne platform, it was shown that the algorithm is suitable to cope with advanced imaging tasks such as corridor mapping along nonlinear features of interest. The experimental data at L-band demonstrated

that by using the proposed TDBP processing approach it is possible to fly a SAR sensor along a nonlinear trajectory without compromising the quality and phase preservation of the final SAR image. In general, the algorithm imposes virtually no restrictions on the shape of the sensor trajectory and it perfectly accounts for topographic variations within the scene. These properties make it an attractive tool for efficient high precision mapping of curvilinear objects by simply allowing the sensor to follow the shape of a road, a river, or a pipeline, for instance. In addition, the experiment showed the potential of the algorithm in terms of high precision processing of SAR data from small unmanned sensor platforms that typically are subject to very strong nonlinear motion due to wind and atmospheric turbulence.

A second experiment consisted of two multibaseline data sets (16 tracks at L-band, 11 tracks at P-band) with a layout optimized for tomographic imaging of a forested area. The resulting three-dimensional data products, obtained by employing three time-domain based tomographic imaging algorithms, multilook beamforming, robust Capon beamforming, and MUSIC beamforming, provide crucial insight into the back-scattering behavior within a forest volume at both L-band and P-band. Within the scope of this research project, for the first time, multibaseline P-band SAR data of a larger forested area were published, and, for the first time, high resolution tomographic SAR images at L-band *and* P-band of the same forested area were available and have undergone a thorough inter-comparison as well as a cross-validation with laser scanning data. An unprecedented level of detail was achieved using the TDBP approach in combination with the advanced spectral estimation methods for tomographic focusing. By means of the tomographic data processing and the subsequent analysis of the three-dimensional data products a substantial contribution towards an improved understanding of the interaction of microwaves at L- and P-band with forest environments was accomplished.

Since non-model-based tomographic reconstruction methods were chosen to image the volume—with a slight restriction concerning the MUSIC algorithm, which is model-based in the sense that the number of scattering sources have to be determined previously—the three-dimensional SAR imaging approaches implemented within this work do not rely on any a priori assumption about the physical structure of a forest nor do they rely on any empirical functions. The good agreement found between the location of the local maxima within the vertical profiles of intensities obtained from the different reconstruction methods, multilook beamforming, the data-adaptive robust Capon beamformer, and

the subspace method MUSIC, indicates that the predominant locations of back-scattering sources within the forest under study were successfully identified. In addition, a good agreement of the SAR vertical profiles of intensities with the histograms of tree heights, as estimated from the difference between the DSM and the DEM from airborne laser scanning, was found for the L-band multi-baseline data set. Thus, the finding that, for the forest under study, coherent back-scattering around the tree-top region of the canopy at L-band is present in all polarization channels is thoroughly supported. Somewhat unexpectedly, the back-scattering mechanisms were found not to change considerably as a function of height within the forest volume at L-band. This leads to the conclusion that back-scattering sources at ground level and within the canopy layer are not necessarily distinguishable only by their polarimetric signature. At P-band, where scattering at the ground level dominates, hardly any surface scattering but mostly dipole and volume scattering was observed.

6.3 Outlook

In view of the potentially upcoming spaceborne mission BIOMASS, the finding that within the forest back-scattering at P-band is virtually exclusively localized at the ground level, supports the scenario of terrain mapping underneath foliage by means of repeat-pass SAR interferometry at P-band. In terms of a single-pass interferometry scenario, as sketched in the Tandem-L proposal, it is noteworthy that at L-band two main locations of back-scattering sources were identified for the forest under study: canopy top and ground level.

In terms of ongoing research in the field of SAR signal processing algorithms, the flexible TDBP-based SAR processor developed within this project provides a good basis for further investigation of advanced SAR imaging modes. Potential fields include bistatic SAR image scenarios. If (quasi-)real-time applications are envisioned in the context of bistatic SAR processing, for instance, a speedup of the image generation process is of interest. A speedup can potentially be obtained either by using factorization approaches or by further optimizing the degree of parallelization, possibly by means of GPU-based parallel processing.

Potential advancements with regard to tomographic imaging involve research towards an optimized exploitation of the polarimetric information within the tomographic focusing step; this in particular with regard to a reliable separation of different back-scattering sources in the case where the number of baselines

is very low. Research opportunities that arise from the three-dimensional SAR tomography data products generated within this work are found 1) in a further validation with respect to field measurements on tree level, now available for the test site, and 2) in a validation of forest scattering models with SAR tomography data products in order to further contribute towards a better understanding of the interaction of microwaves with vegetation volumes at L- and P-band.

Acknowledgment

This dissertation was funded by the Procurement and Technology Center armasuisse of the Swiss Federal Department of Defense. At armasuisse, I would like to thank Peter Wellig, Konrad Schmid, and Daniel Wyssen for their constant support and their interest in the project. I would also like to thank the E-SAR/F-SAR team at the SAR Technology Department of the Microwaves and Radar Institute at the German Aerospace Center DLR, in particular, Ralf Horn, Rolf Scheiber, Martin Keller, and Andreas Reigber for their cooperation and technical support during as well as in the aftermath of the SWISAR 2006 airborne SAR campaign. Thanks are also due to all colleagues at the Remote Sensing Laboratories who have contributed to the successful completion of this thesis, be it, either in the form of intense collaboration or, even more valuable, through providing a friendly and welcoming atmosphere that made working as well as many hours of my spare time a lot more enjoyable. A special thank you goes to Erich Meier who not only agreed to but rather actively supported my idea to dive into the world of SAR image processing and SAR tomography. He provided the contacts and the funding sources without which this project and, particularly, the extensive airborne SAR experiment would not have been possible. He absolutely never lacked enthusiasm about the project at any time and he has always been a very motivating and thoughtful supervisor. I would also like to thank Michael Schaepman and Klaus Itten for accompanying this PhD thesis as the chairs of my promotion committee. Besides giving many useful hints they were always lending an ear to questions, concerns and problems of any kind. I gratefully acknowledge the following people for their scientific collaboration within the project or their support with either fieldwork, proofreading scientific papers, or technical support: Arnold Barmettler, Max Frioud, Daniel Henke, Michael Jehle, Felix Morsdorf, Christophe Magnard, Daniel Nüesch, Maurice Rüegg, Adrian Schubert, David Small, Oliver Stebler, Bruno Weber, and Lukas Zuberbühler. A special thank you also goes to Livia Hollenstein for proofreading major parts of the manuscript. Finally, I would like to thank my family and my friends. Their much-appreciated love and friendship have always provided me with a solid foundation to rely upon.

Scientific Communications

Peer-Reviewed Journal Papers

- [1] **O. Frey** and E. Meier, “3D SAR imaging of a forest using airborne multi-baseline data at P- and L-band,” *IEEE Transactions on Geoscience and Remote Sensing*, in review.
- [2] **O. Frey** and E. Meier, “Analyzing tomographic SAR data of a forest with respect to frequency, polarization, and focusing technique,” *IEEE Transactions on Geoscience and Remote Sensing*, accepted.
- [3] M. Jehle, **O. Frey**, D. Small, and E. Meier, “Measurement of ionospheric TEC in spaceborne SAR data,” *IEEE Transactions on Geoscience and Remote Sensing*, vol. 48, no. 6, pp. 2460–2468, Jun. 2010.
- [4] **O. Frey**, C. Magnard, M. Rüegg, and E. Meier, “Focusing of airborne synthetic aperture radar data from highly nonlinear flight tracks,” *IEEE Transactions on Geoscience and Remote Sensing*, vol. 47, no. 6, pp. 1844–1858, Jun. 2009.
- [5] **O. Frey**, F. Morsdorf, and E. Meier, “Tomographic imaging of a forested area by airborne multibaseline P-band SAR,” *Sensors*, vol. 8, no. 9, pp. 5884–5896, Sep. 2008.
- [6] F. Morsdorf, **O. Frey**, E. Meier, K. I. Itten, and B. Allgöwer, “Assessment of the influence of flying altitude and scan angle on biophysical vegetation products derived from airborne laser scanning,” *International Journal of Remote Sensing*, vol. 29, no. 5, pp. 1387–1406, Mar. 2008.

Peer-Reviewed Conference Papers

- [1] F. Morsdorf, **O. Frey**, B. Koetz, and E. Meier, “Ray tracing for modeling of small footprint airborne laser scanning returns,” in *Intl. Archives of the*

Photogrammetry, Remote Sensing and Spatial Information Sciences, vol. XXXVI, Part 7/C50, Sep. 2007, pp. 294–299.

- [2] **O. Frey**, E. Meier, and D. Nüesch, “Processing SAR data of rugged terrain by time-domain back-projection,” in *SPIE Vol. 5980, 598007: SAR Image Analysis, Modeling, and Techniques VII*, 2005.

(Extended-)Abstract-Reviewed Conference Papers

- [1] **O. Frey** and E. Meier, “Analyzing tomographic SAR data of a forest with respect to frequency, polarization, and focusing technique,” in *Proc. IEEE Int. Geosci. and Remote Sens. Symp.*, Jul. 2010, pp. 150–153, invited Paper.
- [2] **O. Frey** and E. Meier, “3D SAR imaging of a forest using airborne MB-SAR data at L- and P-band: Data processing and analysis,” in *Proc. of EUSAR 2010 - 8th European Conference on Synthetic Aperture Radar*, 2010, pp. 166–169.
- [3] **O. Frey** and E. Meier, “A comparative tomographic evaluation of airborne multibaseline SAR data at P- and L-band,” in *IEEE Int. Geosci. and Remote Sens. Symp.*, 2009, invited Talk. Abstract.
- [4] **O. Frey**, C. Magnard, M. Rüegg, and E. Meier, “Focusing SAR data acquired from non-linear sensor trajectories,” in *Proc. IEEE Int. Geosci. and Remote Sens. Symp.*, 2008, pp. 415–418.
- [5] **O. Frey**, C. Magnard, M. Rüegg, and E. Meier, “Non-linear SAR data processing by time-domain back-projection,” in *Proc. of EUSAR 2008 - 7th European Conference on Synthetic Aperture Radar*, 2008, pp. 165–168.
- [6] **O. Frey** and E. Meier, “Combining time-domain back-projection and Capon beamforming for tomographic SAR processing,” in *Proc. IEEE Int. Geosci. and Remote Sens. Symp.*, 2008, pp. 445–448, invited Paper.
- [7] **O. Frey** and E. Meier, “Tomographic focusing by combining time-domain back-projection and multi-looking based focusing techniques,” in *Proc. of EUSAR 2008 - 7th European Conference on Synthetic Aperture Radar*, 2008, pp. 73–76, invited Paper.
- [8] C. Magnard, **O. Frey**, M. Rüegg, and E. Meier, “Improved airborne SAR data processing by blockwise focusing, mosaicking and geocoding,” in *Proc.*

of *EUSAR 2008 - 7th European Conference on Synthetic Aperture Radar*, 2008, pp. 375–378.

- [9] **O. Frey**, F. Morsdorf, and E. Meier, “Tomographic processing of multi-baseline P-band SAR data for imaging of a forested area,” in *Proc. IEEE Int. Geosci. and Remote Sens. Symp.*, 2007, pp. 156–159.
- [10] **O. Frey**, F. Morsdorf, and E. Meier, “Tomographic SAR imaging of a forested area by time-domain back-projection,” in *Proc. 10th Intl. Symposium on Physical Measurements and Spectral Signatures in Remote Sensing*, M. Schaepman, S. Liang, N. Groot, and M. Kneubühler, Eds., vol. XXXVI, no. 7/C50. Intl. Archives of the Photogrammetry, Remote Sensing and Spatial Information Sciences, 2007.
- [11] **O. Frey**, E. Meier, and D. Nüesch, “An integrated focusing and calibration procedure for airborne SAR data,” in *Proc. of EUSAR 2006 - 6th European Conference on Synthetic Aperture Radar*, 2006.
- [12] F. Morsdorf, **O. Frey**, E. Meier, K. I. Itten, and B. Allgöwer, “Assessment on the influence of flying height and scan angle on biophysical vegetation products derived from airborne laser scanning,” in *3D Remote Sensing in Forestry*, Feb. 2006.
- [13] **O. Frey**, E. Meier, and D. Nüesch, “A study on integrated SAR processing and geocoding by means of time-domain backprojection,” in *Proc. International Radar Symposium*, vol. 1, 2005, pp. 645–649.
- [14] **O. Frey**, E. Meier, D. Nüesch, and A. Roth, “Geometric error budget analysis for TerraSAR-X,” in *Proc. of EUSAR 2004 - 5th European Conference on Synthetic Aperture Radar*, vol. 1, 2004, pp. 513–516.
- [15] M. Jehle, **O. Frey**, D. Small, E. Meier, and D. Nüesch, “Improved knowledge of SAR geometry through atmospheric modelling,” in *Proc. of EUSAR 2004 - 5th European Conference on Synthetic Aperture Radar*, vol. 1, 2004, pp. 909–912.
- [16] **O. Frey**, A. Papritz, P. Lehmann, and A. Gygi, “Geostatistical analysis and filtering of X-Ray CT-scans of the pore structure of a sand,” in *Joint Meeting of Geostats-UK, BRITISH SOCIETY OF SOIL SCIENCE, ISTRO (TEGWG), Reading UK*, 2002, abstract.

Other Communications

- [1] **O. Frey**, M. Frioud, C. Magnard, and E. Meier, “Development of a modular and flexible SAR processor – Annual report 2009,” Remote Sensing Laboratories, University of Zurich, Technical Report 4500317436/8003407964, 2010, report to the Federal Authorities of the Swiss Confederation.
- [2] **O. Frey**, M. Frioud, C. Magnard, and E. Meier, “Development of a modular and flexible SAR processor – Annual report 2008,” Remote Sensing Laboratories, University of Zurich, Technical Report 4500317436/8003404653, 2009, report to the Federal Authorities of the Swiss Confederation.
- [3] **O. Frey**, M. Frioud, C. Magnard, and E. Meier, “Development of a modular and flexible SAR processor – report 2007,” Remote Sensing Laboratories, University of Zurich, Technical Report 4500317436/8003401492, 2008, report to the Federal Authorities of the Swiss Confederation.
- [4] **O. Frey**, M. Rüegg, C. Magnard, and E. Meier, “Development of a modular and flexible SAR processor – Annual report 2006/2007,” Remote Sensing Laboratories, University of Zurich, Technical Report 4500317436/4500318424, 2007, report to the Federal Authorities of the Swiss Confederation.
- [5] M. Rüegg, **O. Frey**, and E. Meier, “Development of a modular and flexible SAR processor – Annual report 2005/2006,” Remote Sensing Laboratories, University of Zurich, Technical Report 4500314939/120271, 2006, report to the Federal Authorities of the Swiss Confederation.
- [6] M. Rüegg, **O. Frey**, and E. Meier, “Development of a modular and flexible SAR processor – Annual report 2004/2005,” Remote Sensing Laboratories, University of Zurich, Technical Report 4500312706/120271, 2005, report to the Federal Authorities of the Swiss Confederation.
- [7] M. Jehle, **O. Frey**, E. Meier, and D. Nüesch, “Estimation and correction of atmospheric path delay in radar signal processing,” Remote Sensing Laboratories, University of Zurich, Technical Note TX-PGS-TN-3016, 2004, under Contract of the German Aerospace Center (DLR).
- [8] **O. Frey**, E. Meier, D. Small, A. Barmettler, and D. Nüesch, “Geometric error budget analysis for TerraSAR-X,” Remote Sensing Laboratories, University of Zurich, Technical Note TX-PGS-TN-3201, 2003, under Contract of the German Aerospace Center (DLR).